



# Paleoenvironmental and paleoclimatic evolution and cyclo- and chrono-stratigraphy of upper Permian–Lower Triassic fluvial-lacustrine deposits in Bogda Mountains, NW China — Implications for diachronous plant evolution across the Permian–Triassic boundary



Wan Yang <sup>a,\*</sup>, Mingli Wan <sup>b,c</sup>, James L. Crowley <sup>d</sup>, Jun Wang <sup>b,c</sup>, Xiaorong Luo <sup>e,c</sup>, Neil Tabor <sup>f</sup>, Kenneth D. Angielczyk <sup>g</sup>, Robert Gastaldo <sup>h</sup>, John Geissman <sup>i,j</sup>, Feng Liu <sup>b</sup>, Peter Roopnarine <sup>k</sup>, Christian A. Sidor <sup>l</sup>

<sup>a</sup> Geology and Geophysics Program, Missouri University of Science and Technology, Rolla, MO 65409, USA

<sup>b</sup> State Key Laboratory of Palaeobiology and Stratigraphy, Center for Excellence in Life and Palaeoenvironment, Department of Palaeobotany and Palynology, Nanjing Institute of Geology and Palaeontology, Chinese Academy of Sciences, Nanjing, China

<sup>c</sup> College of Earth and Planetary Sciences, University of Chinese Academy of Sciences, Beijing, China

<sup>d</sup> Department of Geosciences, Boise State University, Boise, ID 83725, USA

<sup>e</sup> Key Laboratory of Petroleum Resources Research, Institute of Geology and Geophysics, Chinese Academy of Sciences, Beijing, China

<sup>f</sup> Department of Earth Sciences, Southern Methodist University, Dallas, TX 75275, USA

<sup>g</sup> Negaunee Integrative Research Center, Field Museum of Natural History, 1400 South Lake Shore Drive, Chicago, IL 60605, USA

<sup>h</sup> Department of Geology, Colby College, Waterville, ME 04901, USA

<sup>i</sup> Department of Earth and Planetary Sciences, University of New Mexico, Albuquerque, NM 87131-0001, USA

<sup>j</sup> Department of Geosciences, The University of Texas at Dallas, Richardson, TX 75080-3021, USA

<sup>k</sup> Department of Invertebrate Zoology and Geology, CA Academy of Sciences, San Francisco, CA 94118, USA

<sup>l</sup> Department of Biology and Burke Museum, University of Washington, Seattle, WA 98195, USA

## ARTICLE INFO

## ABSTRACT

### Keywords:

Age model

Permo-Triassic

Cyclostratigraphy

Northwestern China

Terrestrial climate

Plant evolution

Stratigraphic sections in the Bogda Mountains, NW China, provide detailed records of late Permian–Early Triassic terrestrial paleoenvironmental and paleoclimatic evolution at the paleo-mid-latitude of NE Pangea. The sections are located in the Tarlong-Taodonggou, Dalongkou, and Zhaobishan areas, ~100 km apart, and ~5000 m in total thickness. An age model was constructed using seven high-resolution U-Pb zircon CA-TIMS dates in the Tarlong-Taodonggou sections and projected to sections in two other areas to convert the litho- and cyclo-stratigraphy into a chronostratigraphy. Sediments were deposited in braided and meandering streams, and lacustrine deltaic and lakeplain-littoral environments. A cyclostratigraphy was established on the basis of repetitive environmental changes for high-order cycles, stacking patterns of high-order cycles, and long-term climatic and tectonic trends for low-order cycles (LC). Sedimentary evidence from the upper Wuchiapingian–mid Induan Wutonggou LC indicates that the climate was generally humid-subhumid and gradually became variable toward a seasonally dry condition in the early Induan. Lush vegetation had persisted across the Permo-Triassic boundary into the early Induan. A subhumid-semiarid condition prevailed during the deposition of mid Induan–lower Olenekian Jiucayuan and lower Olenekian Shaofanggou LCs. These three LCs are largely continuous and separated by conformities and diastems. Intra- and inter-graben stratigraphic variability is reflected by variations in thickness, depositional system, and average sedimentation rate, and results in variable spatial and temporal stratigraphic resolution. Such stratigraphic variability is mainly controlled by paleogeographic location, depocenter shift, and episodic uplift and subsidence in the source areas and catchment basin.

A changeover of plant communities occurred during the early Induan, postdating the end-Permian marine mass extinction. However, riparian vegetation and upland forests were still present from the mid Induan to early Olenekian, and served as primary food source for terrestrial ecosystems, including vertebrates. Correlation of the vascular plant evolutionary history from the latest Changhsingian to early Induan in the Bogda Mountains with

\* Corresponding author.

E-mail address: [yangwa@mst.edu](mailto:yangwa@mst.edu) (W. Yang).

those reported from Australia and south China indicates a diachronous floral changeover on Pangea. The late Permian–Early Triassic litho-, cyclo- and chrono-stratigraphies, constrained by the age model, provides a foundation for future studies on the evolution of continental sedimentary, climatic, biologic, and ecological systems in the Bogda region. It also provides a means to correlate terrestrial events in the mid-paleolatitudes with marine and nonmarine records in the other parts of the world.

## 1. Introduction

Significant advances have been made in our understanding of the magnitude, timing, pace, and causes of the end-Permian mass extinction in the terrestrial realm and ensuing Early Triassic biotic recovery (e.g., Retallack, 1995; Retallack et al., 1996; Ward et al., 2005; Shen et al., 2011, 2019; Benton and Newell, 2014; Zhang et al., 2016; Benton, 2018; Feng et al., 2018; Fielding et al., 2019; Gastaldo, 2019; Gastaldo et al., 2020b). Many continental late Permian–Early Triassic records in Africa, Australia, Antarctica, Texas, Argentina, and southwestern, northern, and northwestern China show highly variable environmental, ecological, and climatic conditions and contain variably preserved plant, invertebrate, and vertebrate fossil assemblages (e.g., Retallack et al., 1996; Sidor et al., 2005, 2013; Chu et al., 2015; Bourquin et al., 2018a, 2018b; Fielding et al., 2019; Botha et al., 2020; Feng et al., 2020; Gastaldo et al., 2020a, 2021). This should be expected in light of the complexity and diversity of the terrestrial world on the supercontinent Pangea over space and time. Thus, more studies are needed to accurately document the tectonic, sedimentary, paleoclimatic, and biotic events during the late Permian and Early Triassic (e.g., Gastaldo et al., 2020a), which can be used to test various hypotheses on the causes of those events (e.g., Chu et al., 2015; Benton, 2018; Mays et al., 2020; Davydov, 2021).

Several intrinsic properties of terrestrial sedimentary and climatic systems present challenges in this effort. First, frequent changes in terrestrial environments and the physical and chemical conditions localized in various catchment basins can cause rapid alternations among depositional, non-depositional, and erosional events affecting sedimentation. As a result, terrestrial sedimentary records are highly incomplete with significant amounts of time represented by paleosols (Gastaldo and Demko, 2011; Thomas et al., 2011), diastems, or erosional surfaces. Individual lithofacies show rapid lateral changes in type and thickness (e.g., Obrist-Farner and Yang, 2015), which prevent reliable high-resolution lithostratigraphic correlation over a distance of 0.1–1 km (e.g., Gastaldo et al., 2009). In addition, environmental changes may have driven turnover of ecological habitats, resulting in biased biomass preservation (e.g., Behrensmeyer et al., 2000; DiMichele and Gastaldo, 2008). Last, but not least, most Permo–Triassic sections have poor numerical age constraints, hindering accurate global correlation among terrestrial sections and also, importantly, with well-documented marine records (Kozur and Weems, 2011; Shen et al., 2011; Burgess et al., 2014; Botha et al., 2020; Schneider et al., 2020; Viglietti et al., 2021). Thus, an enhanced understanding of the sedimentary and paleoclimatic systems that host the ecosystems and solid litho- and chrono-stratigraphic frameworks of the upper Permian–Lower Triassic terrestrial sections are crucial to understanding the paleontological and ecological histories of the mass extinction at the end of Permian and ensuing Triassic recovery in the terrestrial realm.

This paper presents an age model constructed using U-Pb zircon dates for the upper Permian–Lower Triassic fluvial-lacustrine sedimentary records in the Bogda Mountains, NW China, at the paleo-mid-latitude of NE Pangea. The model is used to establish a chronostratigraphic framework in the Bogda region from the litho- and cyclo-stratigraphy of nine sections exposed in the Tarlong-Taodonggou, Dalongkou, and Zhaobishan areas, spanning a geographic distance of ~100 km. Detailed interpretations of lithofacies, depositional systems, and their boundary relationships and lateral changes using field-based sedimentary and stratigraphic evidence depicts the evolution of

environmental and tectonic conditions that affected the sedimentary system. Interpretation of climate-sensitive sedimentary indicators shows that a humid–subhumid condition persisted from the late Wuchiapingian to the mid Induan across the Permian–Triassic boundary (PTB). The onset of a bona fide subhumid–semiarid condition occurred in the mid Induan and continued into the Olenekian, as did the turnover of vascular plants. The results of this study serve as a foundation for future multi-faceted geochemical and paleontological studies of terrestrial biotic events in NE Pangea, and their correlation with marine and non-marine records in other parts of the world.

## 2. Geologic background

### 2.1. Tectonic and depositional settings

This study focuses on three areas in the foothills of the Bogda Mountains, Xinjiang Uygur Autonomous Region, NW China, where upper Permian–Lower Triassic strata are superbly exposed and moderately folded (Fig. 1A–F). The areas are Tarlong-Taodonggou and Zhaobishan in the south and Dalongkou in the north, covering 88, 100, and 7 km<sup>2</sup>, respectively. The Tarlong-Taodonggou area is ~80 km south of Dalongkou and ~100 km west of Zhaobishan. The Bogda Mountains are a giant anticline composed of Devonian to Quaternary sedimentary and igneous rocks, and separate the Turpan–Hami Basin to the south from the eastern part of Junggar Basin to the north (Zhang, 1981; XUARBGMR, 1993; 1999). Uppermost Carboniferous–Triassic fluvial and lacustrine deposits are exposed at many localities along the northern, western, and southern foothills of Bogda Mountains (Fig. 1C; e.g., Yang et al., 1986; Liao et al., 1987; Cheng and Lucas, 1993; Carroll et al., 1995; Shao et al., 1999; Wartes et al., 2002; Greene et al., 2005; Metcalfe et al., 2009; Yang et al., 2010; Obrist-Farner and Yang, 2015, 2016). These were deposited in grabens and half-grabens of the greater Turpan–Junggar continental rift basin on the upper Carboniferous–basal Permian basement, composed of marine sedimentary and volcanic rocks, and formed by collisional tectonics between the Junggar and northern Tianshan plates (Allen et al., 1993, 1995; Yang et al., 2007a, 2010, 2013; Yang, 2008). Continental rifting was probably caused by regional sinistral shearing (Allen et al., 1995; Şengör and Nat'lin, 1996; Şengör et al., 2018; cf. Carroll et al., 1995 and Wartes et al., 2002). Yang et al. (Yang et al., 2007a, 2010; see also Jeffrey, 2011; Obrist-Farner and Yang, 2015, 2017) interpreted the Permo–Triassic strata in the Tarlong-Taodonggou area as being deposited in a half graben, as indicated by drastic lateral facies and thickness changes. Using seismic data in the Turpan–Hami Basin, Yang (2008; see also Yang et al., 2010) interpreted the Permian–Early Triassic paleogeography of the greater Turpan–Hami and Junggar basin to be similar to the Neogene to Quaternary Basin-and-Range Province of the western US, where active alluvial and lacustrine sedimentation had occurred in many small grabens and half grabens. Recent plate tectonic reconstructions place the study area at the easternmost margin of the Kazakhstan Plate at about 45°N in NE Pangea during the Permian–Triassic time (Fig. 1A; Şengör and Nat'lin, 1996; Scotese and Wright, 2018; Şengör et al., 2018; cf. Li et al., 2003).

The upper Permian–Lower Triassic sediments were deposited in fluvial-lacustrine environments (Shao et al., 1999; Yang et al., 1986; Wartes et al., 2002; Yang et al., 2007a, 2010). Lake expansion and contraction, and fluvial peneplanation and deposition, occurred episodically in the basin (Yang et al., 2007a, 2010). Siliciclastic sediments were mainly derived from the northern Tianshan suture zone to

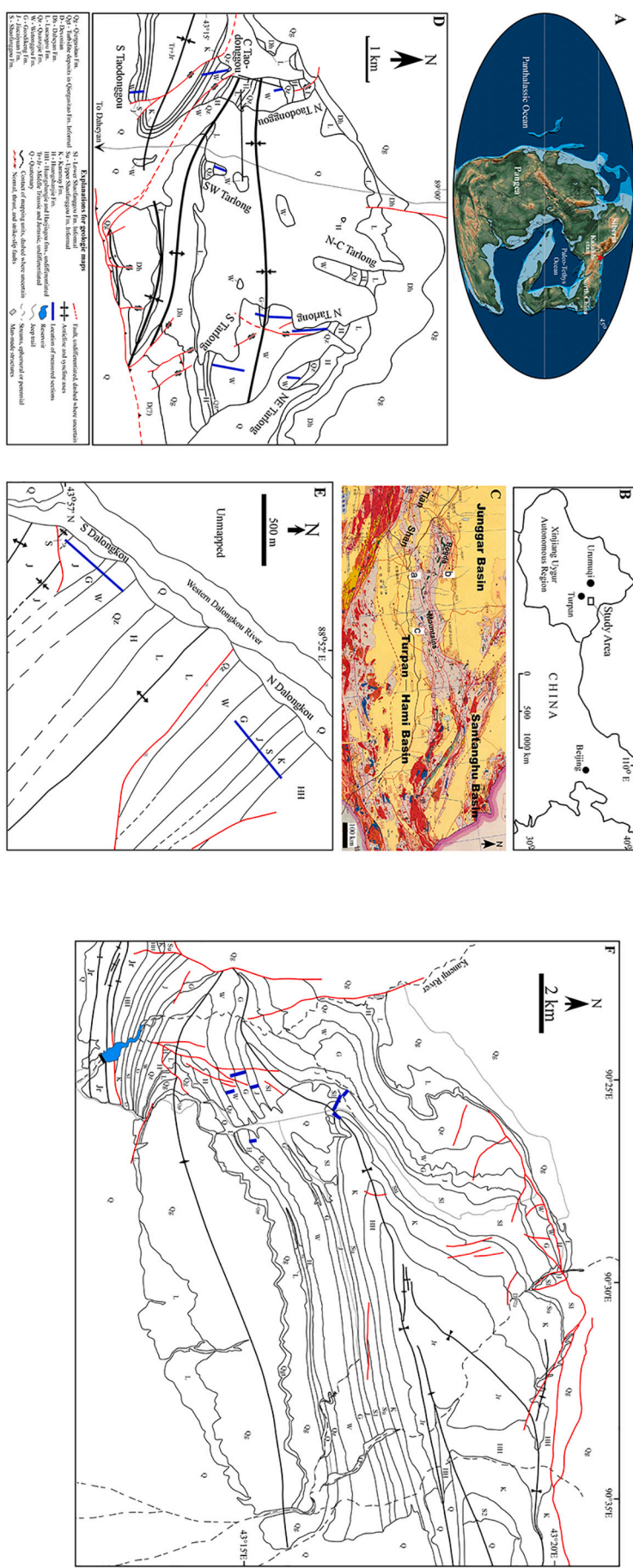


**Fig. 1.** A) Global paleogeographic reconstruction at the Permo-Triassic boundary at ~251 Ma from [Scotese and Wright \(2018\)](#). The study area in the greater Turpan-Junggar basin (red star) is located on the eastern Kazakhstan Plate at a paleolatitude of ~45° N, similar to the reconstruction of [Sengör et al. \(2018\)](#). B) Map of NW China showing the study area in NE Xinjiang Uyghur Autonomous Region in NW China. C) Geologic map of NE Xinjiang showing study areas of Tarlong-Taodonggou (a) and Zhaobishan (c) in the southern and Dalongkou (b) in northern foothills of the Bogda Mountains. Modified from Xinjiang Bureau of Geology and Mineral Resources (1993). D, E, F) Geologic maps of Tarlong-Taodonggou, Dalongkou, and Zhaobishan areas, respectively, showing the approximate location of measured sections (blue lines). Revised from [Yang et al. \(2007a, 2010\)](#), [Obrist-Farner and Yang \(2015, 2016, 2017\)](#), and [Zheng and Yang \(2020\)](#). See figs. S1A–C, S2A–C, S3A–C, and S4A–C in supplemental materials for maps showing detailed transects of measured sections.

the south, with some contributions from local horsts (e.g., Carroll et al., 1995; Shao and Stattegger, 2001; Wartes et al., 2002; Greene et al., 2005; Guan et al., 2011; Fredericks, 2017; Zheng and Yang, 2020).

## 2.2. Stratigraphy and age model

The stratigraphy of upper Permian–Lower Triassic sedimentary sequences in the Bogda Mountains and northern Tianshan areas, as well as the subsurface of the Turpan–Hami and Junggar basins, has been constrained mainly by lithostratigraphy and invertebrate biostratigraphy (primarily ostracods and conchostracans), vascular plants, palynology (spores and pollen), and vertebrates (Fig. 2; e.g., Yuan and Young, 1934; Zhang, 1981; Yang et al., 1986; Liao et al., 1987; Cheng and Lucas, 1993; Liu, 1994; Cheng et al., 1996; Zhou et al., 1997; Ouyang and Norris, 1999; Liu, 2000; Liu et al., 2002; Pang and Jin, 2004; Afonin and Foster, 2005; Zhu et al., 2005; Foster and Afonin, 2006; Metcalfe et al., 2009; Liu and Abdala, 2017; and references therein). Magnetostratigraphic (e.g., Li et al., 2003; Glen et al., 2009) and chemostratigraphic data (e.g., Cao et al., 2008; Metcalfe et al., 2009) are limited mainly to a few PTB sections. Most stratigraphic studies have focused on PTB sections, mainly those at the southern Dalongkou and central Taodonggou sites (Fig. 1D, E). A chronostratigraphy was established by calibrating lithostratigraphy with biostratigraphy at two to three key sections, which was initially carried out during regional geologic mapping and has been updated over the years (e.g., Zhang, 1981; Yang et al., 1986; XUARBGM, 1993; 1999). This chronostratigraphy was not calibrated with high-precision radiometric dates until the study of Yang et al. (2010). Nevertheless, the chronostratigraphy has been widely referenced in a variety of regional studies (e.g., Allen et al., 1995; Carroll et al., 1995,

2010; Shao et al., 1999; Shao and Stattegger, 2001; Wartes et al., 2002; Greene et al., 2005; Yang et al., 2007a).

In the last 15 years, our research team has made a concerted effort to identify volcanic ash deposits in the upper Carboniferous to Lower Triassic sections and carry out high-resolution geochronologic studies on these samples. Yang et al. (2010) published five U-Pb zircon chemical abrasion isotope dilution-thermal ionization mass spectrometry (CA-TIMS), one U-Pb zircon sensitive high resolution ion microprobe (SHRIMP), and two  $^{40}\text{Ar}/^{39}\text{Ar}$  biotite dates, which constrain the latest Carboniferous to Lopingian age of the strata in the Tarlong-Taodonggou area. Five preliminary U-Pb zircon CA-TIMS dates subsequently were published by Yang et al. (2013, 2018) that indicate the basaltic and marine sedimentary rocks in the basement in Tarlong-Taodonggou area are Late Pennsylvanian in age; and rifting and nonmarine deposition in the area started at about 301 Ma and persisted at least to the Olenekian. These age dates have been used to calibrate the upper Carboniferous to Lower Triassic cyclostratigraphy, within which some sedimentologic, stratigraphic, and paleontological studies have been carried out (e.g., Yang et al., 2010; Guan et al., 2011; Jeffrey et al., 2011; Thomas et al., 2011; Wan et al., 2014, 2020, a, a, b, b, c, 2021a, 2021b; Obrist-Farner and Yang, 2015, 2016, 2017; Lu, 2016; Peng, 2016; Fredericks, 2017; Zhan, 2019; Zheng and Yang, 2020; Angielczyk et al., 2021).

The cyclostratigraphy of Yang et al. (2007a, 2010) was established in the Tarlong-Taodonggou area and later improved by Obrist-Farner and Yang (2015). It consists of three orders (high, intermediate, and low) of sedimentary cycles. High-order cycles (HCs) are defined on the basis of repetitive changes of sedimentary environments. Intermediate-order cycles (ICs) are composed of stacked high-order cycles deposited in a pattern of large-scale lake expansion and contraction or fluvial

Stages	Formations	Low-order cycles	Thickness (m) and number of high-order cycles (in parentheses) of low-order cycles in measured sections									
			South Taodonggou	Central Taodonggou	North Taodonggou	North Tarlong	Northeast Tarlong	South Tarlong	Southwest Tarlong	North Dalongkou	South Dalongkou	Zhaobishan
Olenekian	Karamay	Karamay	>50	>50						104.3 (13)		>100
			?	?	?					?		?
	Shao-fanggou	Shao-fanggou 250.53			249.2							249.4
			249.7 Ma	81.5 (42)	127 (71)					249.6	Faulted & deformed	365.7 (95)
Induan	Jiucai-yuan	Jiucaiyuan 251.36	76.9 (26)	83.3 (10)						84.3 (14)	51.5 (?) (11)	312.3 (139)
						Not exposed				75.3 (27)	74.1 (34)	
	Guo-dikeng	Wutonggou	124.5 (60)							36.2 (14)		
			Last coal 252.29			Last coal		Last coal		40.1 (6)		
Changhsingian	Wutonggou	Wutonggou	Not exposed		329.4 (128)					Not measured		
						826.1 (319)		836.0 (312)		287.5 (120)	456.4 (248)	
							Not measured					
							110.2 (59)		295.4 (85)			
Wuchiapingian	Quan-zijie	Upper Quan-zijie		25.8							163.8	222.3 (undifferentiated lower and upper Quan-zijie low-order cycles)
				Not exposed	110.4	66.4	81.0	85.5	86.7			

**Fig. 2.** Upper Permian–Lower Triassic chrono-, litho-, and cyclo-stratigraphy of measured sections in the Tarlong-Taodonggou, Dalongkou, and Zhaobishan areas of the Bogda Mountains, NW China. The vertical axis is time in Ma. Ages of stage boundaries are from International Commission on Stratigraphy (2020); the ages for the bases of Changhsingian, Olenekian, and Induan in parentheses are from Ogg et al. (2020); the difference in assigned ages between the two time scales demonstrates the fluidity of stage ages. Ages of formation boundaries are approximate. Low-order cycles (LCs) are adapted from Yang et al. (2007a, 2010) and Obrist-Farner and Yang (2015). Ages of LC boundaries are estimates from the age model presented in the current study for north and south Tarlong and south Taodonggou sections and projected using average sedimentation rates into other sections. The last occurrence of the major coal bed in the Wutonggou LC in Tarlong-Taodonggou and south Taodonggou areas is marked. Hachured areas indicate major unconformities between the Shaofanggou and Karamay LCs. Thickness and number of high-order cycles of LCs are shown. Thickness of upper Quan-zijie LC is from Obrist-Farner and Yang (2016), except in the Zhaobishan Section. See text and Fig. 3 for age models.

aggradation. Low-order cycles (LCs) contain similar ICs and reflect long-term trends of environmental, climatic, and/or tectonic conditions. The Capitanian–Olenekian interval in the Tarlong-Taodonggou area is largely continuous without major unconformities and consists of five LCs. These LCs are the Capitanian lower and upper Quanzijie, Lopin-gian–lower Induan Wutonggou, mid–upper Induan Jiucaiyan, and the Olenekian Shaofanggou LCs (Yang et al., 2007a, 2010; Obrist-Farner and Yang, 2015), which are adopted in this study (Fig. 2). Some LCs correlate approximately with lithostratigraphic formations (Fig. 2). However, the lower and upper Quanzijie LCs correlate roughly with the Quanzijie Formation; the upper part of the Wutonggou LC contains the Guodikeng Formation because of the gradual environmental and climatic changes between the Wutonggou, Guodikeng, and Jiucaiyan formations (Yang et al., 2010). Finally, the contact between the Shaofanggou and overlying Karamay LCs is a major unconformity (Yang et al., 2010).

In this study, the upper Permian–Lower Triassic cyclostratigraphy is further refined by a new age model. The model is constructed using seven U-Pb zircon CA-TIMS dates obtained from volcanic ash deposits in the Tarlong-Taodonggou area; and the results are interpreted as depositional ages (Fig. 3; geochronologic methods and data are in Appendix 1 and supplementary materials). Six dates are from the Wutonggou LC in the north and south Tarlong sections and the south Taodonggou section; one date from the Shaofanggou LC in the south Taodonggou section. Three Bayesian age models were constructed using the dates for three composite sections following the methods of Trayler et al. (2020): north Tarlong-south Taodonggou, south Tarlong-south Taodonggou, and normalized three sections (Fig. A1). The three sections are correlated using a persistent coal bed in the upper part of the Wutonggou LC as the datum. The model for the normalized sections (Model 3 in Table 1; Fig. 3) is preferred and adopted throughout the paper because it incorporates and utilizes the greatest number of U-Pb CA-ID-TIMS dates (Fig. A2).

The proposed age model significantly changes the age assignments of pre-existing litho-, cyclo-, and chrono-stratigraphic boundaries and, for the first time, places high-resolution points of stage boundaries on the upper Permian–Lower Triassic Tarlong-Taodonggou sections (Table 1; Figs. 2, 3). The age of the base of the Wutonggou LC is ~254.8 Ma, as projected by linear extrapolation from the age model. This age is significantly younger than those of 255.5 and 255.7 Ma projected from the other two models (Table 1; Figs. 3, A2). Those ages place the base of the Wutonggou LC in the mid–upper Wuchiapingian Stage (ICS, 2020; cf. Ogg et al., 2020). The age of the base of Jiucaiyan LC in the south Taodonggou and south Tarlong sections is ~251.56 and ~251.79 Ma, respectively, placing the base in the lower to mid-Induan Stage (ICS, 2020; cf. Ogg et al., 2020). The age of the base of the Shaofanggou LC in the south Taodonggou section is ~250.53 Ma, placing the base of this unit in the lower Olenekian Stage (ICS, 2020; cf. Ogg et al., 2020). The age of the top of the Shaofanggou LC in the south Taodonggou Section is projected to be ~249.7 Ma, placing the top of this unit in the lower Olenekian Stage (ICS, 2020; cf. Ogg et al., 2020). This age constrains the lower age limit of the Shaofanggou–Karamay unconformity. In addition, an age projected for the major coal bed in the upper Wutonggou LC is ~252.29 Ma, which is about 0.39 Ma older than the PTB at 251.902 Ma (ICS, 2020). Furthermore, the Wuchiapingian and Changhsingian boundary (ICS, 2020; cf. Ogg et al., 2020) is projected at a position of 225 m above the base of the Wutonggou LC, but at 310 and 355 m based on the other two age models, respectively (Table 1). In these models, the PTB is positioned at 77 and 828 m above the base of the south Taodonggou and south Tarlong sections, respectively. The Induan to Olenekian boundary is positioned at 139 m above the base in the south Taodonggou Section. For boundaries below and above the limits of our age model, and in sections besides the north and south Tarlong and south Taodonggou sections, average sedimentation rates derived from the age model are used to estimate their ages or stratigraphic positions (see “Low-Order Cycles” below).

The above age calibrations allow us to establish a much-improved

chronostratigraphy. Within this framework, the evolution of terrestrial sedimentary, tectonic, climatic, biologic, and ecologic systems in the paleo-mid-latitude of NE Pangea during the late Permian and Early Triassic can be more accurately addressed and correlated with marine and non-marine records in other parts of the world. However, inherent uncertainties in radiometric age data, age model construction, and age extrapolation, as well as stratigraphic variability among measured sections, need to be considered in the objective discussion of the evolution of these systems (Table 1; Figs. 3, A1, A2; Appendix 1; see “Low-Order Cycles” and “Discussion”).

### 3. Data and methodology

Ten stratigraphic sections with a total thickness of ~5000 m in the Wutonggou, Jiucaiyan, and Shaofanggou LCs were measured at a cm-dm scale. Geologic mapping of the three areas was carried out to identify structural features and select the best-exposed section transects to study in detail (Fig. 1C–F), which are marked on Google satellite images (Figs. S1A–C, S2A–C, S3A–C, S4A–C) for reference. Most sections provide 100% exposure, although trenching was frequently required to remove modern colluvium from the outcrop surface. Field observations, descriptions, measurements, and recording follow conventional methods. A total of ~500 samples of representative lithologies were collected, of which ~300 samples were thin-sectioned for petrographic observations under stereo and polarized microscopes of grain composition and sedimentary texture. A large number of paleocurrent measurements were taken from tabular cross beds and oriented gravels of fluvial sandstones. Detailed stratigraphic sections containing field data, measurements, and descriptions, as well as interpretations of depositional environment, lake type, climate, and tectonics, are presented in Supplemental Materials (Figs. S1D–G, S2D–E, S3D–E, S4D).

A cyclostratigraphic approach is employed to decipher regional and long-term climatic and tectonic trends of the low-order cycles (Fig. 4). It is efficient for correlation of terrestrial successions with rapid lateral facies and thickness changes due to frequent environmental changes and erosion in a rift setting (e.g., Yang et al., 2007a, 2010; Obrist-Farner and Yang, 2015, 2016, 2017; Zheng and Yang, 2020). Cyclostratigraphic analysis and correlation start with depositional environment interpretation of individual lithofacies on the basis of lithology, sedimentary structure, fauna and flora, and stratal geometry and boundary relationship. In addition, seven types of paleosols were identified through field observations of lithology, soil texture and structures, color, and soil morphology, which were confirmed by thin-section observations (see Tables 1 and 2 of Yang et al., 2010; Thomas et al., 2011). The paleosol data were used to substantiate environmental interpretations. However, these data are discussed only where necessary and will be fully reported in future publications. The next step is the interpretation of three orders of sedimentary cycles. Specifically, a high-order cycle (HC) reflects a cycle of environmental changes associated with lake expansion and contraction or fluvial erosion-and-deposition, and is the basic cyclostratigraphic entity recognized on the outcrop (Fig. 4).

Finally, the low-order cycles (LCs) are correlated using a process-response strategy (Fig. 5), which employs not only the type, thickness, and stacking patterns of HCs in a LC, but also the interpreted trends of climatic and tectonic conditions during cyclic sedimentation. The principles for the interpretations of lake type and climatic and tectonic conditions follow those of Yang et al. (Yang et al., 2010; see also Yang et al., 2007a, Obrist-Farner and Yang, 2015, 2016, 2017; Fig. 4). The lake-type classification follows that of Carroll and Bohacs (1999). The interpretation of paleoclimatic conditions is based mainly on sedimentary evidence including paleosols (Table 2 of Yang et al., 2010; Thomas et al., 2011). The climatic conditions are interpreted qualitatively on the basis of estimated precipitation/evaporation ratios. Cross-verification among proxy indicators is done wherever possible.

The tectonic conditions are interpreted for the sediment-source area and the depositional site considering the possibilities of both short-term

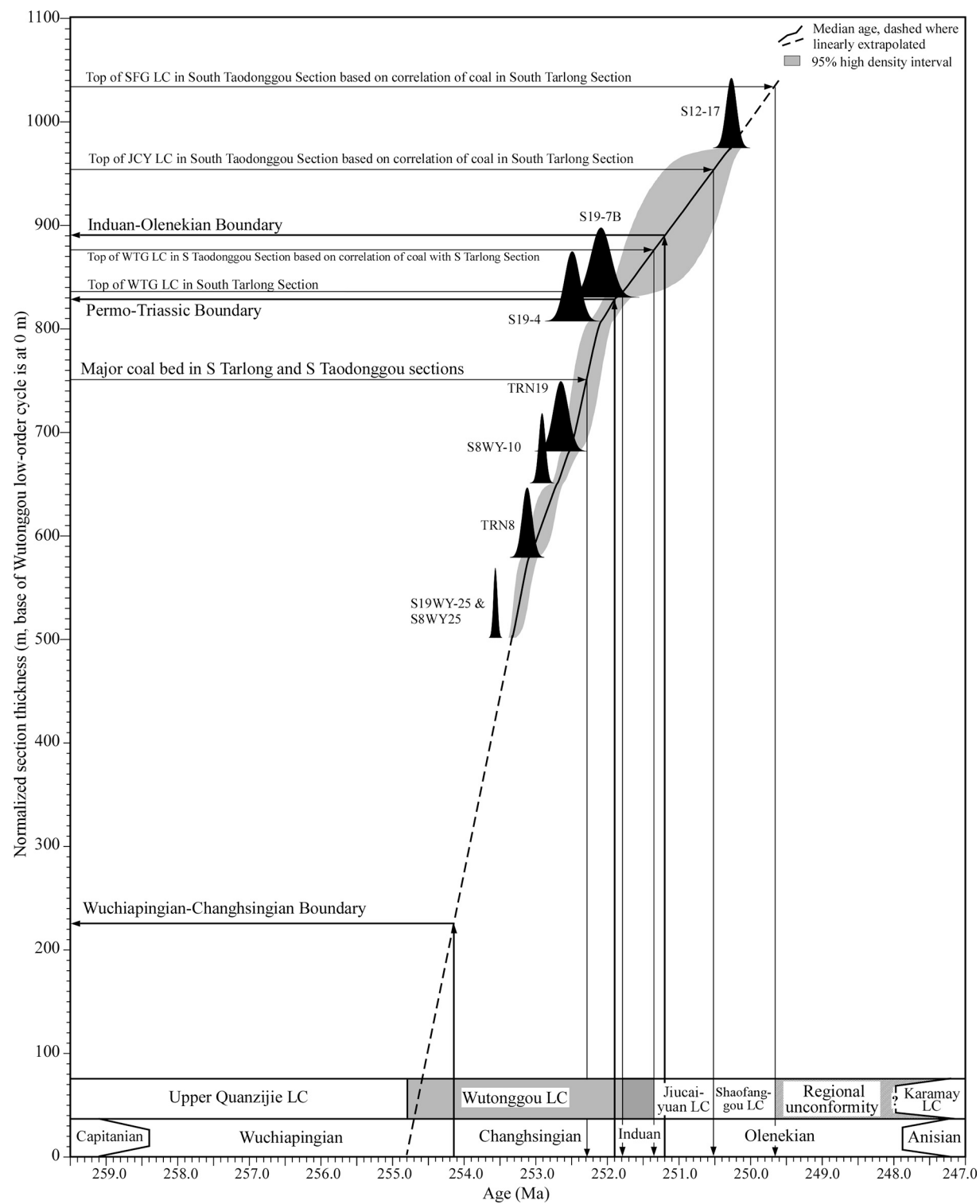


**Fig. 3.** Bayesian age model of upper Permian-Lower Triassic strata constructed using seven zircon U-Pb CA-TIMS dates in the south and north Tarlong and south Taodonggou sections. The section thickness is normalized with respect to that of south Tarlong and south Taodonggou. See normalization schemes in Fig. A1. Ages for stage boundaries are from International Commission on Stratigraphy (2020); the boundaries are projected onto the normalized section to show their respective stratigraphic positions. Boundaries of low-order cycles (LCs) and the last major coal bed are projected onto the age axis to show their respective ages. Dashed lines beyond the range of age model are linear extrapolations from adjacent segments. WTG = Wutonggou, JCY = Jiucaiyuan, and SFG = Shaofanggou LCs. See Table 1 for detailed age estimates; Fig. A2 for two alternative age models constructed using age dates from the south Tarlong-south Taodonggou and north Tarlong-south Taodonggou sections, respectively. See Appendix A for detailed descriptions of geochronologic methods and data.

**Table 1**

Age estimates of low-order cycle boundaries and stratigraphic positions of stage boundaries in north and south Tarlong and south Taodonggou sections, as calibrated by three age models.

Age model	Median age and range of base of low-order cycles and coal bed in upper Wutonggou low-order cycle in respective sections (Ma)					Stratigraphic positions and range of stage boundaries in respective sections (m)		
	Wutonggou	Jiucaiyuan <sup>c</sup>	Shaofanggou	Karamay	Coal bed (upper Wutonggou)	Wuchiapingian - Changhsingian	Changhsingian - Induan (PTB) <sup>c</sup>	Induan - Olenekian
Model 1 (STRL- STDG)	255.5 <sup>a</sup>	251.79 (251.35–251.99, STRL <sup>b</sup> )		249.6 <sup>a</sup> (252.09–252.54)	252.29 (252.09–252.54)	310 <sup>a</sup> (STRL)	828 (809–848, STRL)	139 (89–205, STDG)
		250.69 (251.36–251.77, STDG)	250.53 (250.29–251.25, STDG)				77 (58–98, STDG)	
Model 2 (NTRL- STDG)	255.7	251.36 (250.69–251.77, STDG)	250.57 (250.32–251.27, STDG)	249.7	252.32 (252.11–252.56)	355 (NTRL)	77 (58–98, STDG)	140 (88–202, STDG)
		251.79 (251.33–251.99, STRL)		249.7	252.29 (252.09–252.48)	225 (normalized section)	77 (59–98, STDG)	139 (88–203, STDG)
Model 3 <sup>d</sup> (STRL- NTRL- STDG)	254.8	251.36 (250.67–251.78, STDG)	250.53 (250.29–251.22, STDG)				829 (810–849, STRL)	

<sup>a</sup> Ages in italics are estimated based on average sedimentation rates from the age models. See text for description.

<sup>b</sup> STRL - south Tarlong section; NTRL - north Tarlong section; STDG - south Taodonggou section.

<sup>c</sup> The base of Jiucaiyuan low-order cycle and the Changhsingian-Induan (PTB - Permo-Triassic Boundary) boundary are present in both south Tarlong and south Taodonggou sections, and are absent in north Tarlong section. The base of Wutonggou LC is not present in south Taodonggou section.

<sup>d</sup> This is the preferred model, constructed using normalized north and south Tarlong sections and Taodonggou section. See text for discussion.

uplift and lowering of lake-spill points (Fig. 4). In reality, a variety of autogenic and allogenic processes must have affected sedimentation at each of the three cyclostratigraphic levels. These interpretations are the best approximations due to the complexity of fluvial-lacustrine sedimentation in half-grabens over time. In this paper, only the most reasonable interpretations are presented based on all of the available evidence. Using the aforementioned, the correlation, anchored by the age model, is used to establish a low-order cyclostratigraphic framework, wherein regional stratigraphic variability, climatic and tectonic histories, and implications on plant evolution in the study area are discussed.

#### 4. Lithofacies, depositional environments, and high-order cycles

The upper Permian-Lower Triassic deposits include conglomerate, sandstone, mudrock, and paleosol, a small proportion of coal and bentonite and tuff, and rare bivalve coquina. Each lithology varies widely in composition, sedimentary texture and structure, fossil content, stratal geometry and boundary relationship, and color. These attributes were used to classify four lithofacies and interpret the depositional environments in which they formed. This section concisely presents the major characteristics of lithofacies, their depositional environments, and high-order cycles. Readers are referred to Yang et al. (Yang et al., 2007a, 2010, and Tables 1 and 2) and Thomas et al. (2011) for more detailed descriptions and interpretations.

##### 4.1. Conglomerate lithofacies

Clast-supported conglomerates are common and contain clasts ranging from granule to boulder in size and andesitic, basaltic, granitic, sedimentary and, rarely, metamorphic in lithology (Guan, 2011; Fredericks, 2017; Zheng and Yang, 2020). Sedimentary clasts were derived dominantly from shale, paleosol, and mud chips, and occur mainly in the basal parts of poorly to moderately sorted conglomerate (Fig. 4E).

Conglomerates have several origins. First, many conglomerates are lenticular, ranging from 0.1–1s of meters in thickness. Clasts are sub-angular to well rounded, imbricated, and moderately to well sorted. Crude plane beds and trough and tabular cross-bedding are common. These deposits form fining-upward successions with intercalated gravelly sandstone in the upper part; basal and internal erosional surfaces are

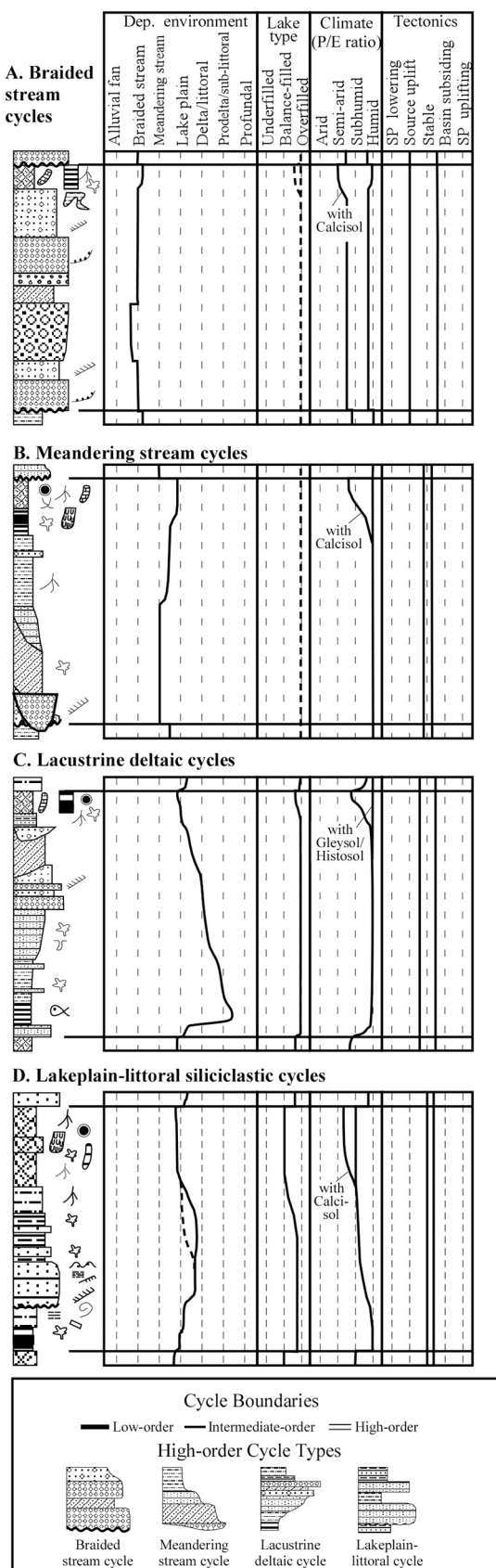
common. They are interpreted as representing either (1) channel-bar and channel-lag deposits of braided streams, where barforms are in low-relief (1–10s cm) with an erosional base; or (2) channel lag and lower point-bar deposits of meandering streams where they fill channel forms with a high-relief (10s–100s cm) erosional base. The second conglomerate type is characterized by a non-erosional concave base overlain by sandstone and shale to collectively form an upward-coarsening and thickening succession. They are interpreted as delta-front deposits (Fig. 4F). The last conglomerate type is composed of thin (1–10s-cm thick) beds that are laterally persistent for 10–100s m. These deposits are well sorted and stratified, contain rounded and imbricated clasts, and have a broad, slightly erosional base. They commonly overlie paleosols and underlie well stratified and well sorted arenites. They are interpreted as well-washed beach and littoral deposits (i.e., shoreline pebbles), commonly associated with shoreline transgression (Fig. 4G).

##### 4.2. Sandstone lithofacies

Lithic wacke, subarenite, and arenite dominate and, generally, are compositionally immature and texturally immature to mature. Lithic framework grains are mainly andesitic and basaltic with a variable amount of rhyolitic and sedimentary lithics (Guan, 2011; Fredericks, 2017; Zheng and Yang, 2020). Feldspars represent <25% of framework grains and quartz <10%. Grains are coarse silt to very coarse sand in size, angular to well rounded, and very poorly to very well sorted. Gravelly sandstones are common. The compositional immaturity, highly variable textural maturity, and complex sedimentary structures of the sandstones are typical of sandy deposits in alluvial, fluvial, and lacustrine environments in intermontane grabens (Yang et al., 2007a, 2010). A sandstone lithofacies may occur in several environments. Thus, stratal geometry, boundary relationships, vertical textural, structural, and thickness trends, fossil content, and facies associations, in addition to the composition, texture, and structure, of individual sandstones, are used to interpret the depositional environment of any particular sandstone body. Major environmental facies of sandstones are briefly described below.

###### 4.2.1. Fluvial sandstone lithofacies

Many of these sandstones occur in the lower part of upward-fining



## EXPLANATIONS

### Lithology

Normal graded conglomerate or sandstone	Shale
Reverse graded conglomerate or sandstone	Silty shale and siltstone
Clast-supported conglomerate	Calcareous shale or mudstone
Matrix-supported conglomerate	Dolostone
Sandstone	Shale, dolomitic.
Well-bedded sandstone	Mudstone
Well-laminated sandstone	Gravelly mudstone
Cross-bedded sandstone	Calcrete (petrocalcic deposits) or palustrine limestone
Gravelly sandstone	Paleosol
Calcareous sandstone	Limestone
Muddy sandstone	Tuffaceous sandstone
Interbedded sandstone and shale	Tuff and bentonite
	Tuffaceous shale

### Sedimentary Texture & Structure

Soil slickensides	Algal coated pisoid and oncoid
Clay cutans, illuviated mud	Planar, tabular, and/or trough x-bedding
Rhizoconcretion or calcitic nodules, equant, elongate, or tabular	Accretionary set
Calcareous clayey or sandy nodules, commonly root mottled	Erosional surface
Fe-oxide pisoids in ferric Gleysols	Internal erosional surface
Rootlets, rhizolith, and molds, illuvial clay-filled, carbonized, or calcified	Parallel and climbing ripple laminations
Plant debris, Well-preserved plant fragments and leaf matter	Hummocky cross stratification (HCS)
Silicified, calcified, or charcoaled wood	Convolute bedding
Vertebrate fossils	Normal and reverse graded bedding
Trace fossils	Cryptalgal lamination
Fish or fish scale fossils	Ripple marks
Ostracod, conchostracean, microgastropod, other shell fragments	Carbonaceous partings and laminae
Mud clasts, angular or rounded	Mud cracks
Carbonate pisoids	Burrows, mottles
Ooids and superficial ooids	Microfaults
	Dissolution cavities/vugs

### Abbreviations

LA - Lithic arenite	dt/l - Delta-front or littoral.
LSA - Lithic subarenite	p/sl - Prodelta or sub-littoral.
LW - Lithic wacke	pf - Profundal.
CRL - Climbing ripple laminations	uf - Underfilled.
XRL - Cross ripple laminations	bf - Balance-filled.
SS - Sandstones	of - Overfilled.
f - fine grained	ar - Arid.
m - medium grained	sa - Semi-arid.
c - coarse grained	sh - Subhumid.
vc - very coarse grained	hd - Humid.
mod. - moderately	spl - Spill-point lowering.
al - Alluvial fan.	sul - Active source uplift.
bs - Braided stream.	stb - Stable and quiescence.
ms - Meandering stream.	sub - Active subsidence.
lp - Lake plain.	spr - Spill-point rising.

### Cycle Names

ntr - north Tarlong; netr - northeast Tarlong; str - south Tarlong; swtr - southwest Tarlong; ntd - north Taodonggou; ctd - central Taodonggou; std - south Taodonggou; nd - north Dalongkou; sd - south Dalongkou; z - Zhaobishan  
 W, J, S, K - Wutonggou (WTG), Jiuciyuan (JCY), Shaofanggou (SFG), and Karamay (KRM) low-order cycles.  
 Example: Jnd 24 - The 24th high-order cycle in Jiuciyuan low-order cycle in north Dalongkou section.

**Fig. 4.** Lithology, sedimentary structures, and interpretation of four types of high-order cycles (HCs) in the upper Permian-Lower Triassic strata. A) Braided stream cycle; B) meandering stream cycle; C) lacustrine deltaic cycle; and D) lakeplain-littoral siliciclastic cycle. Several cycle variations are common in each major cycle type and not all the component lithofacies are present in any one specific cycle. No vertical scale intended, while HCs are mostly 0.1–10 m thick. Interpretation begins with depositional environment, lake type (speculative for non-lacustrine cycles), climate, and ends with tectonics. Dashed lines indicate speculative or alternative

interpretations. Modified from Yang et al. (2007a, 2010). Explanations are for all stratigraphic sections in the current paper and supplemental materials. E) Field photo of a channel-lag conglomerate overlying cross-bedded sandstone with a low-relief erosional surface in a braided stream deposit. Red Calcisol cobble and boulder (black arrows) in the conglomerate contain coalesced cm-size calcitic nodules in a calcareous muddy matrix, and were probably derived from a nearby penecomtemporaneous Calcisol. The petrified wood reported by Wan et al. (2019c) is preserved in this interval. Hammer is 30 cm long. Lower Shaofanggou LC in Zhaobishan section. F) Field photo showing a lacustrine deltaic HC composed of basal transgressive upward-fining conglomerate and sandstone, middle maximum-transgressive sublittoral-prodeltaic shale and sandstone, and upper coarsening-upward delta-front sandstone and conglomerate, which is incised by a meandering stream filled by upward-fining conglomerate and sandstone. The transgressive deposit overlies the Quanzijie braided stream deposit (see a close-up in G). The partially-covered prodeltaic-sublittoral interval is ~13 m thick. View to north. Basal Wutonggou LC in Zhaobishan section. G) Field photo showing a close-up of the transgressive deposit in (F). The lower pebble conglomerate is well sorted with rounded, imbricated clasts, and is matrix-free. It is in a sharp contact with an overlying well-sorted coarse arenite with high-angle tabular cross beds (beach shingles). The conglomerate and sandstone form an upward-fining beach-littoral deposit at the base of the Wutonggou LC in the Zhaobishan section, signifying a major lake shoreline transgression and expansion. Ruler is 15 cm long. H) Field photo showing two stacked meandering stream HCs. The lower stream cuts into two stacked Calcisols containing two petrocalcareous beds (white arrows) in the Bk horizons. The Calcisols were developed in the deltaplain mudrocks overlying the prodeltaic and delta-front shale and sandstone. The Calcisol zone in the middle-upper Wutonggou LC is correlated across the study areas (see Fig. 10 and text). Field view is to north and ~50 m across. Middle Wutonggou LC in the Zhaobishan section. I) Field photo showing three successions of fluvial-lacustrine deposits in the middle Shaofanggou LC in Zhaobishan. The basal succession consists of braided stream deposits, which are transgressed by a beach-littoral deposit composed of a well-sorted medium-very coarse grained arenite. The middle succession is a stack of 11 HCs composed of upward-coarsening sublittoral-beach shale, siltstone, and very fine to medium sandstone. The littoral-beach sandstones are laterally persistent and contain well-developed medium to high-angle tabular cross beds (white arrows). The upper succession contains three stacked Calcisols with well-developed Bk horizons hosted in lakeplain mudflat deposits. The three successions are ~20 m thick. J) Field photo showing an intermediate-order cycle bounded at the base by a transgressive surface on fluvial deposits and on top by a fluvial erosional surface. The lower part is a stack of six upward-coarsening littoral-beach fine-coarse sandstone HCs (~5 m thick), which is overlain by a stack of 11 upward-coarsening sublittoral-littoral shale-sandstone/siltstone HCs (~18 m thick). Both successions form an overall fining-upward retrogradational succession as transgressive deposits and are capped by the maximum-transgressive surface or maximum-flooding surface. The overlying deltaic deposits (~10 m thick) were deposited during lake contraction. Hammer (circled) is 30 cm long. The thickness of distant strata is distorted. View is to northwest and ~300 m across. Lower Wutonggou LC in Zhaobishan section. K) Field photo showing an upward-coarsening succession of prodeltaic shale and delta-front sandstone. A close examination identified a high-order cycle boundary separating an argillaceous Protosol from an overlying ostracod-bearing prodeltaic shale. The last major coal bed occurs above the delta-front sandstone on the other side of the ridge. Hammer is 40 cm long. View to the south. Middle Wutonggou LC in the north Tarlong section. L) Field photos showing long vertical-subvertical, downward branching rhizoconcretions in highly-mature Calcisols in the uppermost part of Shaofanggou LC in the north Dalongkou (left) and central Taodonggou (right) sections. Thin dashed white lines outline possible root systems. Thick dashed white line in the left photo is the boundary between the Shaofanggou and Karamay LCs. Both hammers are 30 cm long. M) Field photo showing a large antiform, or gilgai, of a petrocalcareous bed composed of amalgamated calcitic nodules in a vertic Calcisol. The person is in the axis of the antiform; the bed dips away from the axis and buckles outward to the reader. Petrocalcareous nodules and discontinuous beds are abundant below and above the gilgai. Ruler is 1.5 m long. Middle Jiucayuan LC in the Zhaobishan section. N) Field photo showing a sharp surface separating underlying delta-front sandstone from overlying prodeltaic shale. The sandstone becomes gradually red and more concentrated with pebble size oncoids (white arrows), signifying microbial activities during a period of sediment starvation. The surface is interpreted as a flooding surface associated with a rapid lake deepening. Pencil is 15 cm long. Middle Wutonggou LC in the north Tarlong section.

◀

bipartite successions, overlying conglomerates or directly above a basal erosional surface (Fig. 4H). They commonly underlie a mudrock-dominated interval. Sand grains commonly are angular to subrounded and poorly to moderately well sorted. These sandstones are classified as subarenites to wackes. Sedimentary structures include large-scale tabular and trough cross-bedding and planar beds, organized into accretionary sheets. They are interpreted as point bar deposits of meandering streams. Sandstones in the upper mud-rich intervals are thin (1–10s cm), laterally persistent wackes. These may be laminated or massive and interbedded with mudrock. Plant remains and root molds are sparse to abundant. These sandstones are interpreted as overbank deposits. However, in other cases, gravelly coarse to very coarse subarenite and arenite are interbedded with conglomerate to form crudely fining-upward successions with minimal or no muddy deposits in the upper part. These units are plane bedded or large-scale cross bedded and fill in channel forms with a low-relief base. These sandstone bodies are interpreted as braided stream deposits.

#### 4.2.2. Lakeshore and littoral sandstone lithofacies

Lithic arenites and subarenites dominate in this lithofacies and contain more quartz and feldspar grains than the other sandstone lithofacies. Reworked mud clasts are common where the sandstone overlies paleosols with a shallow and undulating erosional contact. Grains range from coarse silt to very coarse sand, are subrounded to well-rounded, and moderately to very well sorted. Plane bed, high-angle tabular cross bed, climbing ripple cross lamination, ripple marks and, in some cases, hummocky cross stratifications are common. This lithofacies is commonly thin (10–100s cm thick) and laterally persistent for 100s of meters (Fig. 4I). Such units are interpreted as well-washed lakeshore to littoral deposits. In many cases, individual facies show a slight, but clear, upward-coarsening trend and are stacked into an overall upward-fining trend. These trends reflect a transgressive lake shoreline associated with lake expansion

(Fig. 4J; Yang et al., 2015). In some cases, laminations in the upper part of the lakeshore deposits are disrupted by rooting structures; here, the sandstones are interpreted as pedogenically-altered sheet flow deposits on a lake plain.

#### 4.2.3. Deltaic sandstone lithofacies

This lithofacies may be either a lithic wacke, subarenite, or arenite in upward-coarsening and thickening successions. The facies overlies shale with a gradational, commonly contorted contact and, in some cases, is overlain by conglomerate with a gradational contact (Fig. 4F). Fine to medium-grained wacke and subarenite are thinly interbedded with silty shale and siltstone in the lower part of the succession. Medium to very coarse-grained, moderately to well sorted subarenite and arenite commonly form clinoforms in the middle and upper parts. In addition, bedding changes upward from climbing ripple cross-laminations to large, low-angle tabular or trough cross-bedding, which commonly are convoluted. In some cases, ripple marks are locally common and hummocky cross stratification is present, indicating wave reworking. Disseminated plant remains are common on bedding planes. Individual successions commonly are lenticular with a concave base and/or a convex top, are 1–10 m thick, and may persist laterally for 100s of meters. In some cases, several successions stack vertically to form an overall coarsening-upward trend. These successions are interpreted as delta-front deposits (Fig. 4K).

#### 4.3. Mudrock lithofacies

The mudrock lithofacies, which contains more than 50% of mud-size particles, has a wide range of characteristics and occurrences. In the field, four general types were differentiated: laminated shale and siltstone, laminated carbonaceous shale and coal, massive mudstone, and massive bentonite.

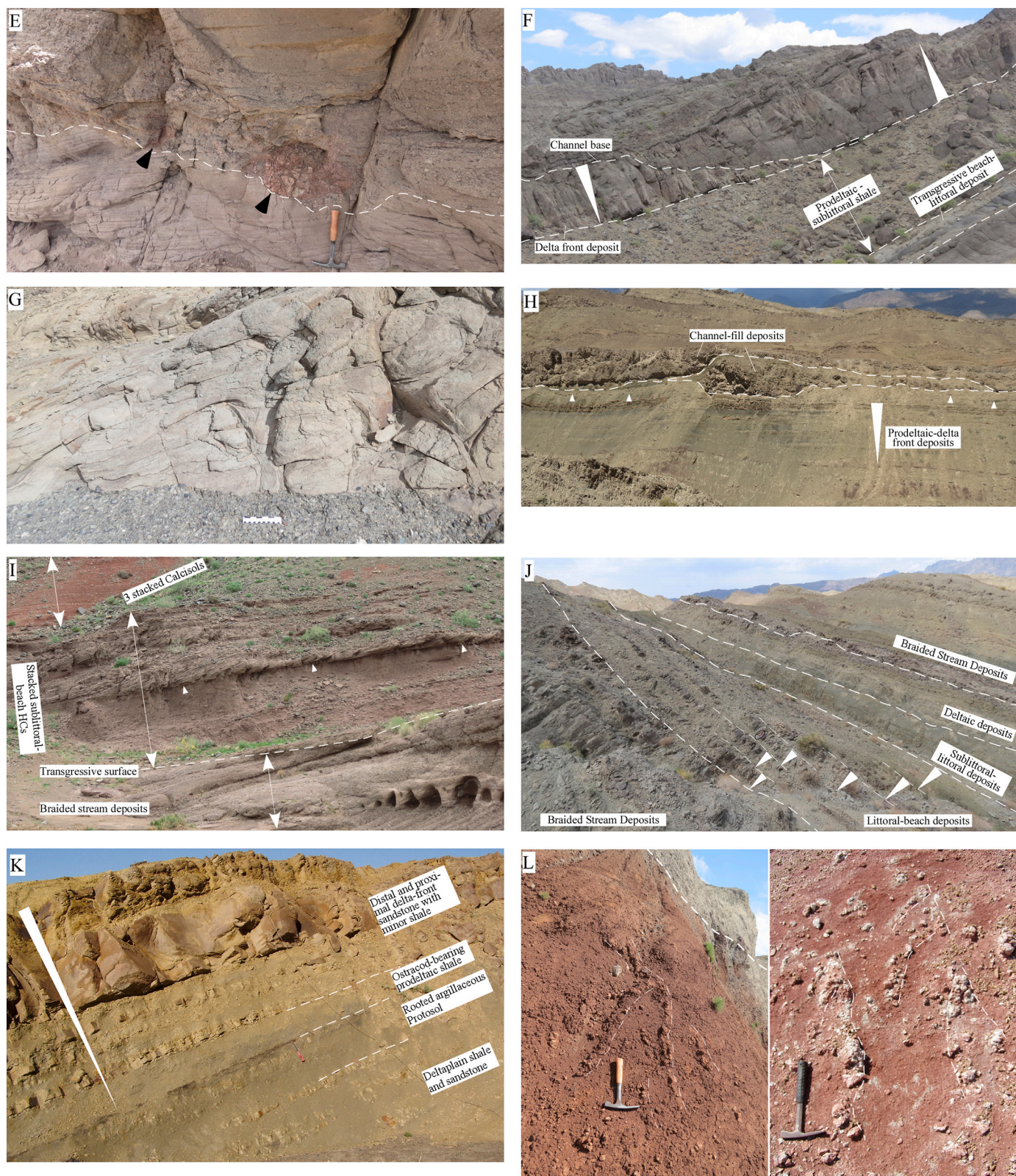


Fig. 4. (continued).

**Shale and siltstone.** This lithofacies is variably calcareous, sandy, and commonly medium to thick laminated, and subdivided into three basic types. First, shale and siltstone in the lower part of upward-coarsening and thickening shale-sandstone and/or conglomerate successions are commonly gray to dark gray, 10–100s of cm thick, and contain abundant

disseminated plant remains and sparse ostracods and conchostracans. Upward, these deposits change from pure or silty shale to siltstone, with an increasing amount of intercalated thin fine-medium-grained sandstone. They are interpreted as prodeltaic deposits. The second type of shale-and-siltstone facies is dark to blackish gray, 1–10s-cm thick, and

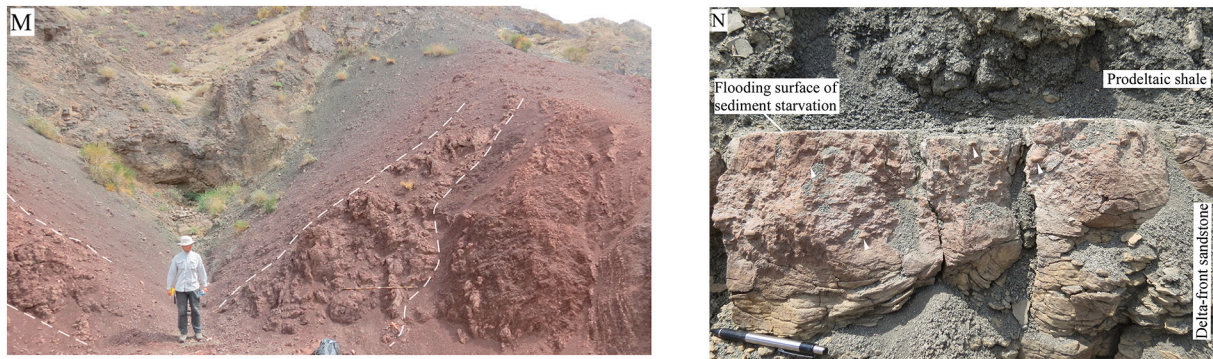
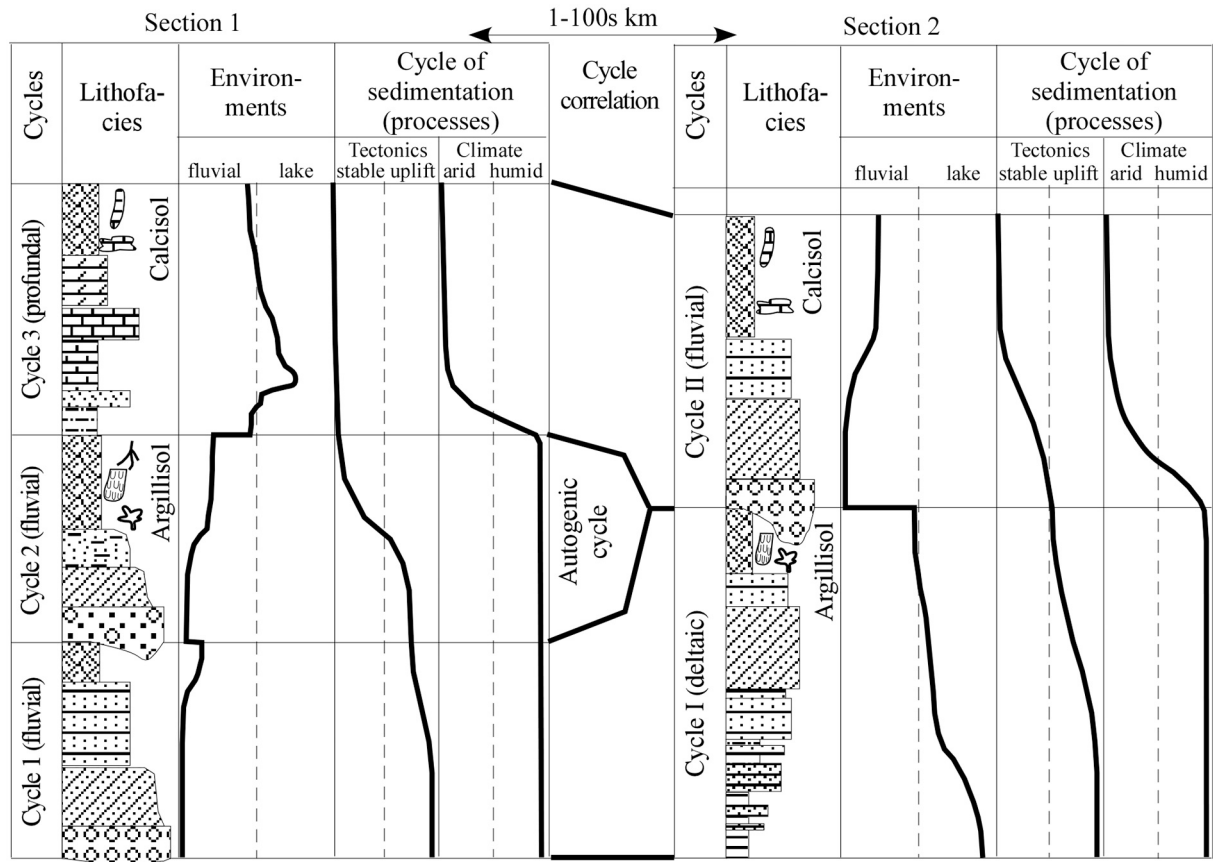


Fig. 4. (continued).

contains abundant ostracods, conchostracans, micro-gastropods, and plant remains. Where this lithofacies overlies paleosols with a broad, slightly erosional contact, it commonly contains angular sand-size mud

fining and thinning conglomerate-sandstone-shale successions. These deposits are brown to reddish brown, and preserve sparse to rich disseminated plant remains without evidence of invertebrate microfos-



**Fig. 5.** Diagram illustrating the rationale and working hypothesis on intra- and inter-graben cyclostratigraphic correlation used in this study. The process-response approach emphasizes correlation of sedimentary cycles and their inherent changes with respect to controlling processes, in addition to cycle type, type and thickness of lithofacies, and depositional environments. A fluvial cycle (or a low-order cycle composed of dominantly fluvial high-order cycles) may correlate with a coeval lacustrine cycle wherein both record a change of the same process. This approach can effectively differentiate local autogenic from regional allogenic cycles and minimize miscorrelation. Correlation of multi-order hierarchical cycles, constrained by geochronologic and biostratigraphic data, will further minimize miscorrelation of coeval but laterally variable cycles. The regionally correlative cycles are the building blocks of a multi-order chronostratigraphic framework.

clasts as rip-up clasts derived from the paleosol. This facies commonly underlies sandstones of littoral characteristics and are interpreted as littoral to swamp deposits formed during initial shoreline transgression (Fig. 4D). Where this lithofacies overlies a littoral sandstone body, they are mostly thinly laminated and interpreted as sublittoral to profundal lacustrine deposits. The third type occurs in the upper part of upward-

sils. The beds are 10–100s cm thick, commonly sandy, platy, or mottled, and may contain pedogenic structures. Intercalated thin sandstones are common. These shale and siltstones are interpreted as fluvial overbank deposits.

Carbonaceous shale and coal. This organic-rich lithofacies is common in some intervals, but volumetrically insignificant. It is black to

blackish gray, variably silty and sandy, well laminated to massive, and commonly thin (1–200 cm thick). The facies has a sharp to gradational base and top. Ostracods, conchostracans, and micro-gastropods are locally concentrated. Coals are lignitic to sub-bituminous in rank. Carbonaceous shale and coals are laterally persistent for 0.1–1s of km.

This lithofacies has three general modes of occurrence. First, some carbonaceous shales are interbedded with overbank deposits and, in a few cases, filling abandoned fluvial channels. These deposits are interpreted to have formed in the floodplain. Second, the facies may underlie lakeshore and littoral sandstone bodies and overlie pedogenically-altered deposits or paleosols, and are associated with initial transgressive shale and siltstone deposits. They are interpreted as marginal swamp deposits laterally coeval with an approaching shoreline and raised water table during early transgression. Finally, carbonaceous shale partings and thin beds occur in sublittoral muddy deposits, and interpreted as having been washed from a nearby riparian plant source with the organic material settling from suspension onto the low-energy sublittoral lake floor.

**Bentonite and tuffaceous deposits.** Bentonite is common, but volumetrically insignificant. It varies from pale gray, blackish gray, to grayish and pinkish white, and is ductile and intensely slickensided. Sparse biotite, quartz, and feldspar grains are present. Bentonites have a sharp to diffuse base and top, and are 1–20 cm thick and laterally persistent, although bed thickness commonly varies laterally. On surface exposure, they form small ridges of a few centimeters in height, due to clay expansion caused by water absorption. This lithofacies is interpreted as altered volcanic ashfall deposits in low-energy lake or overbank environments.

Similar to bentonites, tuff and tuffaceous sandstone are also common. They are unaltered and have distinctive bright orange, yellow, and red coloration. Sand grains include fine to medium-grained quartz, potassium feldspars, bright pink to red lithics, and sparse biotite, and are moderately well sorted and angular to subrounded. Small, equant to irregular calcitic nodules commonly occur in the shales adjacent to bentonite and tuff. They are diagenetic and probably related to the chemical alteration of ash deposits during burial.

**Massive mudstone.** Two types of massive mudstones are identified. First, some mudstones are dark gray and contain abundant disseminated plant remains and micro-gastropods, ostracods, and conchostracans. The absence of lamination may have been the result of extensive burrowing. This lithofacies is interpreted as having been deposited in a low-energy oxygenated shallow embayment. Second, other massive mudstone is variegated and exhibits common pedogenic features. These are interpreted as paleosols, which are described below.

#### 4.4. Paleosols

Seven types of paleosols, including Protosol, Calcisol, Vertisol, Argillisol, Gleysol, Histosol, and possible Gypsisol, were identified mainly on soil structures, including ped shape, size, and surface characteristics, chemical and physical accumulations in the soil profile, and stratigraphic changes of structures and products (Mack et al., 1993). The occurrence and type of paleosol are useful in depositional environmental and qualitative paleoclimatic interpretations because they indicate a period of landscape stability and nondeposition and provide critical clues on climatic conditions (e.g., Retallack, 1990; Mack and James, 1994; Gastaldo et al., 2020a). Readers are referred to the detailed descriptions and interpretations of these paleosols in Yang et al. (2010, their Table 2) and Thomas et al. (2011; see also Obrist-Farner and Yang, 2015, 2016).

Protosols are massive and variegated with red, brown, purple, yellow, and orange colors, showing diffuse to discrete color mottling. They contain poorly-developed blocky or platy peds and soil horizons, and common relict lamination. Climatic conditions cannot be confidently interpreted because of the absence of distinctive climate indicators in these immature soils. Yet, Protosols do indicate subaerial exposure and a

short stasis in deposition.

Calcisols contain well-developed blocky peds and common to abundant equant, elongate, to tabular, autobrecciated micritic nodules. The nodules are discrete; some contain common sparry calcite-filled rounded molds. Elongate nodules are 1–100s cm in length and 0.1–10s cm in diameter. Nodules may be oriented subvertically, and may be downward branching and tapering. These structures are interpreted as rhizoconcretions or root molds (Fig. 4L). Tabular nodules are 3–50 cm thick and up to 5 m long, roughly bedding parallel, and commonly occur below equant and elongate nodules. These are interpreted as petrocalcic deposits precipitated near the groundwater table. Some thick tabular petrocalcic beds composed of autobrecciated blocks form large pseudo-anticlines (gilgai; Fig. 4M). Calcisols have a muddy matrix, which contains weakly to moderately calcareous, platy, prismatic, or equant peds. Peds are angular to rounded, and ~2–30 mm in size. Color mottles are rare to abundant, rounded, and have diffuse to sharp boundaries. Soil profiles range from 10s of centimeters to 2 m in thickness with well-developed Bk, Bt, and BC horizons; stacked profiles are common. Calcisols developed in well-drained sediments accumulated in floodplain, lakeplain, and exposed ephemeral lake environments under an arid to semiarid climate (Mack and James, 1994; Thomas et al., 2011).

Vertisols contain well-developed prismatic to wedge-shaped peds and abundant slickensides. Slickensides are 1–10 cm long and coated with oriented clays. Well-developed antiformal-synformal structures are rare (Fig. 4M). Vertisols indicate a climate with a strong precipitation seasonality (Mack and James, 1994). However, some Vertisols contain a varying amount of calcitic nodules. These are interpreted as calcic Vertisols formed on low-relief lakeplain or floodplain landscapes under a semiarid or seasonally dry climate. Other Vertisols contain varying amounts of iron-oxide nodules and concretions, and are interpreted as ferric Vertisols formed in a subhumid climate. Finally, some Vertisols are gray to dark gray and underlie transgressive lake deposits. They are interpreted as gleyed Vertisols formed under the condition of a raised water table (Thomas et al., 2011).

Argillisol are characterized by common illuvial clays (argillans; Retallack, 1990; Mack et al., 1993) in and coating surfaces of blocky peds. The argillans are sub-mm to mm thick, shiny, and continuous on ped surfaces, or may fill mostly subvertical-vertical mm-scale tubules. Gray to blackish gray Argillisol have a noncalcareous matrix and, in some cases, abundant disseminated plant remains. Carbonaceous films may line clay-filled tubules or occur as remains of decayed roots. This type of Argillisol is gleyed and indicative of a subhumid to humid conditions. In contrast, reddish brown Argillisol are moderately to highly calcareous and may contain calcareous clay-filled tubules and, rarely, calcitic rhizoliths or thin twigs. Calcareous Argillisol may have developed under a subhumid-semiarid condition.

Gleysols are dark to blackish gray exhibiting a blocky to prismatic structure. They form dominantly in mudrocks underlying transgressive surfaces or lignites. Carbonized rootlets are common, ranging from 1 to 10 cm long. In addition, horizons with sparse to highly concentrated iron-oxide pisoids are common (for example, see Yang et al., 2010; Obrist-Farner and Yang, 2016). The pisoids are brown, discrete, rounded, and 3–20 mm in diameter. The horizons are dark gray, brown, or variegated, ranging in thickness from 30 to 100 cm. A muddy matrix is non-calcareous and organic poor. Individual soil profiles are 1–2 m thick and commonly stacked, and have vague horizonation, except where pisoids-bearing horizons are present. The dark gray color, preservation of plant organic matter, abundant iron-oxide pisoids, and stratigraphic position of Gleysols indicate that they formed in humid, water-logged, low-land environments probably associated with a raised water table caused by transgression and establishment of lake margin swamps (Thomas et al., 2011).

Histosols, here, include coals and intercalated carbonaceous shale and highly mottled mudstone. Coals are 1–200 cm thick, and composed of in-situ accumulation of plant material in transgressive swamps or abandoned fluvial channels. One thick coal bed in the upper Wutonggou

LC in the north and south Tarlong and south Taodonggou sections overlies an interval of gray mudstone containing calcitic nodules of a diagenetic origin. It serves as the correlation datum between the three sections (Figs. 2, 3, A1). Histosols formed in poorly to very poorly-drained low-land lake margin or floodplain environments, and are indicative of a humid climate.

Finally, Gypsisols are interpreted from indirect field and petrographic evidence presented by Thomas et al. (2011; see also Yang et al., 2010). This paleosol exhibits blocky peds and common bladed carbonate nodules enclosed in a muddy matrix. The nodules are muddy and display a rosette form, mimicking calcite replacement of original gypsum nodules. They are capped by micritic dolomite crusts containing desiccation cracks. These suspected Gypsisols may have developed in the exposed muddy sediments of ephemeral lakes under an arid climate.

#### 4.5. Depositional systems and sedimentary cycles

Lithofacies deposited in any environment are genetically linked by sedimentary processes operating therein, and are stacked to form a depositional system when environments shift (Brown Jr. and Fisher, 1977). Hence, repetitive lateral environmental shifts at a locality result in repetitive vertical stacking of depositional systems and component lithofacies in the stratigraphic record. Each stratigraphic repetition of depositional systems and/or component lithofacies defines a sedimentary cycle, reflecting a cycle of environmental shift and associated changes in environmental conditions and sedimentary processes. The upper Permian–Lower Triassic deposits are strongly cyclic because fluvial-lacustrine sedimentation is sensitive to frequent environmental change (Talbot and Allen, 1996).

##### 4.5.1. High-order cycles

Four types of cycles are interpreted in the upper Permian–Lower Triassic deposits including braided stream, meandering stream, lacustrine deltaic, and lakeplain-littoral cycles (Fig. 4; Yang et al., 2007a, 2010). The braided and meandering stream cycles are defined by their basal erosional surface and overlying fluvial deposits, representing repetitive changes between phases of erosion or nondeposition (stasis) and deposition. In contrast, lacustrine deltaic and lakeplain-littoral cycles are each composed of successions formed during lake expansion and contraction. An erosional base may or may not be present. In general, the four cycle types are thin (0.1–1s m thick) and form the basic cyclostratigraphic units in the measured sections. As noted above, high-order cycles (HCs) provide a framework for the interpretation of processes and factors controlling cyclic sedimentation and changes in environment, lake type, and climatic and tectonic conditions. A total of 1856 HCs were delineated in all measured sections (Fig. 2) and their major characteristics are described concisely below. Readers are referred to Yang et al. (2007a, 2010; see also Obrist-Farner and Yang, 2016) for detailed descriptions.

Braided stream high-order cycles. Braided stream HCs contain an upward-fining succession of clast-supported conglomerate and sandstone over a low-relief erosional base (Fig. 4A). Cycle thickness ranges from 1 to 11 m. Variably-developed Calcisols are, in some cases, present in the upper part of some cycles, indicating a more stable paleolandscape in comparison with cycles without Calcisols.

The climate conditions under which a braided stream cycle formed is inferred from climate-sensitive sedimentary features, if present (Fig. 4A). These features reveal climate variability at the high-order scale. However, Yang et al. (2007a, 2010) cautioned that the effects of tectonic and autogenic processes must be removed before a reasonable paleoclimatic interpretation can be arrived. However, the removal may not be possible, because, in some cases, the climatic interpretation of a sedimentary feature is non-unique, climatic signals were largely masked or obliterated by other processes, and/or the effects of other processes on sedimentation are non-unique and cannot be interpreted accurately. Thus, the interpreted climatic conditions for HCs are preliminary and of

the first order (also see Thomas et al., 2011). In this study, climate is qualitatively interpreted with respect to the precipitation (P)/evaporation (E) ratio as arid (ratio  $<< 1$ ), semiarid (ratio  $< 1$ ), subhumid (ratio  $> 1$ ), and humid (ratio  $> 1$ ).

Tectonic influence on intermontane sedimentation is typically significant (e.g., Carroll and Bohacs, 1999; Wartes et al., 2002; Carroll et al., 2010; Yang et al., 2010). It includes the movement of provenance and lake-spill point, and subsidence at the depositional site. Possible tectonic effects on any depositional environment and resultant lithofacies are interpreted and filtered prior to climate interpretation (Fig. 4A). In addition, tectonic influence will affect the type of lake filling a graben. These lakes may be either over-, balance-, or under-filled, following the classification of Carroll and Bohacs (1999). The classification is based on facies associations and stacking patterns, emphasizing the interactions between tectonic and climatic processes on lacustrine sedimentation. Lake type is speculated for fluvial cycles, assuming a lake was present near the site of deposition.

Finally, we note the typical dilemma inherent in the graphical presentation of interpretations (Fig. 4A–D). The curves of environment and lake types that are correlated with the lithologic column are drawn relative to thickness of a unit. In contrast, climate and tectonic curves are drawn relative to time, including hiatuses at the tops of cycles when deposition ceased and pedogenesis and/or erosion dominated. For example, the semi-arid condition at the uppermost part of a Calcisol-capped cycle (Fig. 4A–D) may represent only the condition during the period of nondeposition and pedogenesis after deposition had ceased, not necessarily the conditions when the uppermost sediments were deposited. This dilemma of graphically presenting spatial and temporal curves together in a single diagram exists for all interpretations based on sedimentary features that were not formed syndepositionally.

Braided stream HCs with a Calcisols cap probably formed under a semiarid-subhumid climate (Mack and James, 1994). Initial erosion and deposition were followed by a prolonged period of nondeposition, landscape stability, and pedogenesis. Intra-cycle variation from a more humid condition during deposition to a more arid condition during pedogenesis may be preserved, but is not necessary because tectonically-controlled topographic relief is the dominant control on braided stream deposition. For cycles without capping Calcisols, deposition may have been relatively continuous and climate relatively humid. Alternatively, continued deposition could have been the result of accelerated subsidence at a depositional site and/or source uplift. On the other hand, rare ferric Gleysol-capped braided stream cycles probably formed in a subhumid-humid climate (Mack and James, 1994).

Meandering stream high-order cycles. Meandering stream HCs exhibit a high-relief erosional base overlain by channel-fill conglomerate and sandstone in the lower part and overbank sandstone, mudrock, and paleosol in the upper part (Fig. 4B). The proportional thickness of channel-fill and overbank deposits differentiates coarse-grained from classic meandering stream cycles. Coarse-grained meandering streams have thick channel-fill and thin overbank deposits (similar to the wandering stream systems of Miall, 1996). These cycles are 2–8 m thick. Channel-fill deposits are conglomerate and gravelly sandstone; overbank deposits are interbedded sandstone and mudrock. The classic meandering stream contains an equal or lesser amount of channel-fill deposits when compared with overbank deposits. These cycles are 2–20 m thick. Channel-fill deposits include channel-lag conglomerate and accretionary point-bar sandstone; overbank deposits are mudrocks intercalated with sandstones.

Meandering streams generally develop on landscapes of a low topographic gradient and commonly require a perennial flow. Thus, meandering stream HCs indicate an enlarged catchment basin and a subhumid-humid climate. Evidence supporting this interpretation includes capping Histosols, Gleysols, or carbonaceous Argillisol (Fig. 4B) and common plant remains and petrified wood. However, the presence of capping Calcisols or calcareous Argillisol in some cycles indicates that the cycles formed under a semiarid-subhumid climate or,

alternatively, as a consequence of intra-cycle variation between subhumid-humid during stream deposition and semiarid-subhumid conditions during nondeposition and pedogenesis. Finally, systematic upward stacking of braided, coarse meandering, and classic meandering stream systems is common (Yang et al., 2010). This indicates that streams evolved during peneplanation and expansion of a catchment basin, provenance denudation, and increased stream discharge caused by an enlarged catchment and/or an increasingly humid climate (Miall, 1996).

**Lacustrine deltaic high-order cycles.** Lacustrine deltaic HCs commonly consist of two depositional systems (Fig. 4C). The lower system is a fining-upward lake margin-sublittoral succession. It has a thin basal transgressive shoreline to littoral deposit of conglomerate and sandstone underlain by a broad, slightly erosional base. This deposit is commonly underlain by an interval composed of upward Gleysol, carbonaceous Argillisol, Histosol, and ostracod and conchostracan-bearing shale, which has a sharp base. They are 1–100s cm thick and common in the Wutonggou LC, and interpreted as subaerial lake-margin deposits associated with an approaching lake shoreline and a raised groundwater table (Yang et al., 2010). Overlying the shoreline-littoral deposit commonly is thinly-laminated shale that is 1–100s cm in thickness and contains common ostracods and scattered fish scales. The shale has a sharp to gradational base, which, in rare cases, is mantled with cm-thick deposits of pisoids and oncoids, indicating a period of starved sedimentation (Fig. 4N). This shale is interpreted as the maximum-transgressive condensed deposit.

The upper system of the deltaic HC contains a thick upward-coarsening and upward-thickening succession of prodeltaic shale and siltstone and delta-front sandstone and/or conglomerate, which, in many cases, is overlain by distributary channel-fill and interdistributary deltaplain conglomerate, mudrock, and paleosols. An entire deltaic HC is on the order of 1–10s m thick and reflects the environmental shifts associated with lake expansion and contraction (Fig. 4C). In some cases, several deltaic HCs stack successively, indicating fluctuation of river influx, delta-lobe switching, or tectonically-induced subsidence resetting the base level. In general, deltaic progradation indicates a large influx of sediment-laden river discharge into an over-filled lake (Carroll and Bohacs, 1999). Such conditions likely occurred under a humid climate, although lake transgression may be of a tectonic, climatic, and/or autogenic origin. In many cycles, common carbonaceous shale, Histosol, and Gleysol in deltaplain deposits indicate humid conditions throughout a deltaic cycle. However, some Lower Triassic cycles are capped by Calcisols, indicating intra-cycle climate variation from a humid condition, during lake expansion and delta progradation, to a semiarid condition at the end or following deltaic deposition (Fig. 4C).

**Lakeplain-littoral high-order cycles.** In general, lakeplain-littoral cycles exhibit a fining-upward succession in the lower part and a coarsening-upward succession in the upper part, each of which corresponds to sedimentation during lake expansion and contraction, respectively (Fig. 4D). Deposits in the lower part of a cycle have a broad, slightly erosional base and contain lakeshore and littoral well-washed sandstone and conglomerate, which grade upward to sublittoral shale and siltstone. Deposits in the upper part mirror the subjacent trend and are characterized by littoral to lakeshore sandstone and lakeplain mudrock and sandstone. These cycles are thin (10–100s cm thick), commonly capped by Calcisols, Vertisols, calcic Vertisols, gleyed Vertisols, and possible Gypsisols, and commonly stacked. Some cycles contain a basal subaerial transgressive deposit, similar to those at the base of deltaic cycles. The absence of thick coarse-grained deposits and the small magnitude of environmental shifts in lakeplain-littoral HCs indicate that the lake was likely balance-filled; the uplift of the source area and subsidence of the depositional site were not significant; and the depositional site was away from deltaic headlands. The climate under which sedimentation occurred was subhumid to semiarid, such that influx of river water and clastic sediments was insufficient for the formation of extensive deltaic deposits. Alternatively, the site may have

been too far from the deltaic depocenter to receive a significant amount of detritus even though there was a prevailing subhumid to humid climate. Moreover, the absence of lacustrine carbonate deposits, as in the fluctuating profundal mixed carbonate-siliciclastic cycles in the lower Permian (Yang et al., 2010), indicates that the climate was humid enough and river discharge high enough such that the lake water was fresh and/or too turbid for carbonate sediments to precipitate. In many cycles, the basal swamp and wetland paleosols and the cycle-capping Calcisols, calcic Vertisols, and possible Gypsisols are indicative of intra-cyclic climatic variation from a subhumid-humid condition during lake expansion to semiarid to arid during lake contraction and subaerial exposure.

#### 4.5.2. Low-order cycles

The stratigraphic stacking patterns of HCs are used to define intermediate and low-order cycles (Yang et al., 2007a, 2010; Obrist-Farner and Yang, 2015). This three-order cyclicity indicates that the geologic processes controlling environmental change had operated with varying dominance and temporal and spatial scales (Talbot and Allen, 1996). Intermediate-order cycles are composed of a succession of HCs that shows an overall upward trend of retrogradation and progradation associated with environmental changes during lake expansion and contraction (Fig. 12 and Table 3 of Yang et al., 2010; e.g., Yang et al., 2007b, 2009; Li et al., 2019). Low-order cycles (LCs) are defined on the basis of similarity in the succession of high- and intermediate-order cycle types, and are demarcated by regional unconformities and/or conformable surfaces. The similarity reflects the long-term trend of environments, which is controlled by long-term tectonic or climatic changes. The nature and magnitude of any environmental shift across a low-order cycle boundary vary between, and within, half grabens (e.g., Jeffrey et al., 2011; Obrist-Farner and Yang, 2015). Hence, the changes in environments and tectonic and/or climatic conditions across unconformable boundaries are abrupt; in contrast, these changes appear as gradational across conformable boundaries. The contrasts in lithofacies, types of high and intermediate-order cycles, interpreted controlling processes, and regional bounding surfaces ensure reliable intra- and inter-graben low-order cycle correlation in the study area (Fig. 5). The spatial and temporal variability in paleoenvironmental, paleoclimatic, and paleotectonic conditions of LCs are described in detail in the context of the age model in the following section.

### 5. Paleoenvironmental, paleoclimatic, and paleotectonic conditions and stratigraphic correlation of low-order cycles

The upper Permian-Lower Triassic fluvial-lacustrine strata in the Tarlong-Taodonggou, Dalongkou, and Zhaobishan areas were deposited likely in three separate grabens or half grabens during a span of about 5 Ma (Table 1; Figs. 1–3; Yang, 2008; Yang et al., 2007a, 2010; Fredericks, 2017; Obrist-Farner and Yang, 2017; Zheng and Yang, 2020). The terrestrial environmental, climatic, and tectonic conditions must have been highly variable in space and time. We endeavor to decipher the variabilities in a cyclostratigraphic framework that is constrained by the age model established in the Tarlong-Taodonggou area. This work is carried out at the low-order cycle scale, which provides the greatest reliability at this stage of our investigation. Six of the ten sections in this study cover at least two complete low-order cycles (LCs); the north Tarlong section covers almost the entire Wutonggou LC; the other three sections supplement the delineation of stratigraphic variabilities (Figs. 2, 6A–D, 7A–C, 8A–B, 9, S1D–G; S2D–E; S3D–E; S4D). Thus, a complete record of Wutonggou-Jiuciyuan-Shaofanggou LCs is preserved in each of the three areas to ensure a reliable regional correlation (Figs. 10–12).

#### 5.1. Wutonggou low-order cycle

The Wutonggou LC spans the late Wuchiapingian to early Induan (254.8 to 251.36 or 251.79 Ma) for about 3.4 or 3.0 Ma in the

normalized and south Tarlong sections, respectively (Table 1; Figs. 2, 3). The difference in duration results from the different stratigraphic positions of the top of the Wutonggou LC in the two sections (Fig. 10; see “Discussion”). The cycle contains the Wuchiapingian–Changhsingian and Permian–Triassic boundaries. The age of the former is older than the lower limit of the age model; its position is estimated using an average sedimentation rate which is calculated using the lower segment from samples TRN8 and S19WY-25 in the age model as 325.56 m/Ma. By applying this rate, the position of the Wuchiapingian–Changhsingian boundary of ICS (2020; cf. Ogg et al., 2020) is estimated at a

stratigraphic position of 221.4 m above the base of Wutonggou LC for the north, south, and southwest Tarlong sections. The age of the base of Wutonggou LC is estimated at 254.8 Ma (Table 1; Figs. 3, 10). However, this rate is not appropriate for the other sections because of the great difference in thickness and variable depositional environments across the region (see below). A second average sedimentation rate is calculated using the ages of 254.8 and 251.36 Ma for the base and top of the Wutonggou LC, respectively (Table 1; Fig. 3). For the central and north Taodonggou, south Dalongkou, and Zhaobishan sections, these rates are 95.2, 83.1, and 131.9 m/Ma. These rates result in the placement of the

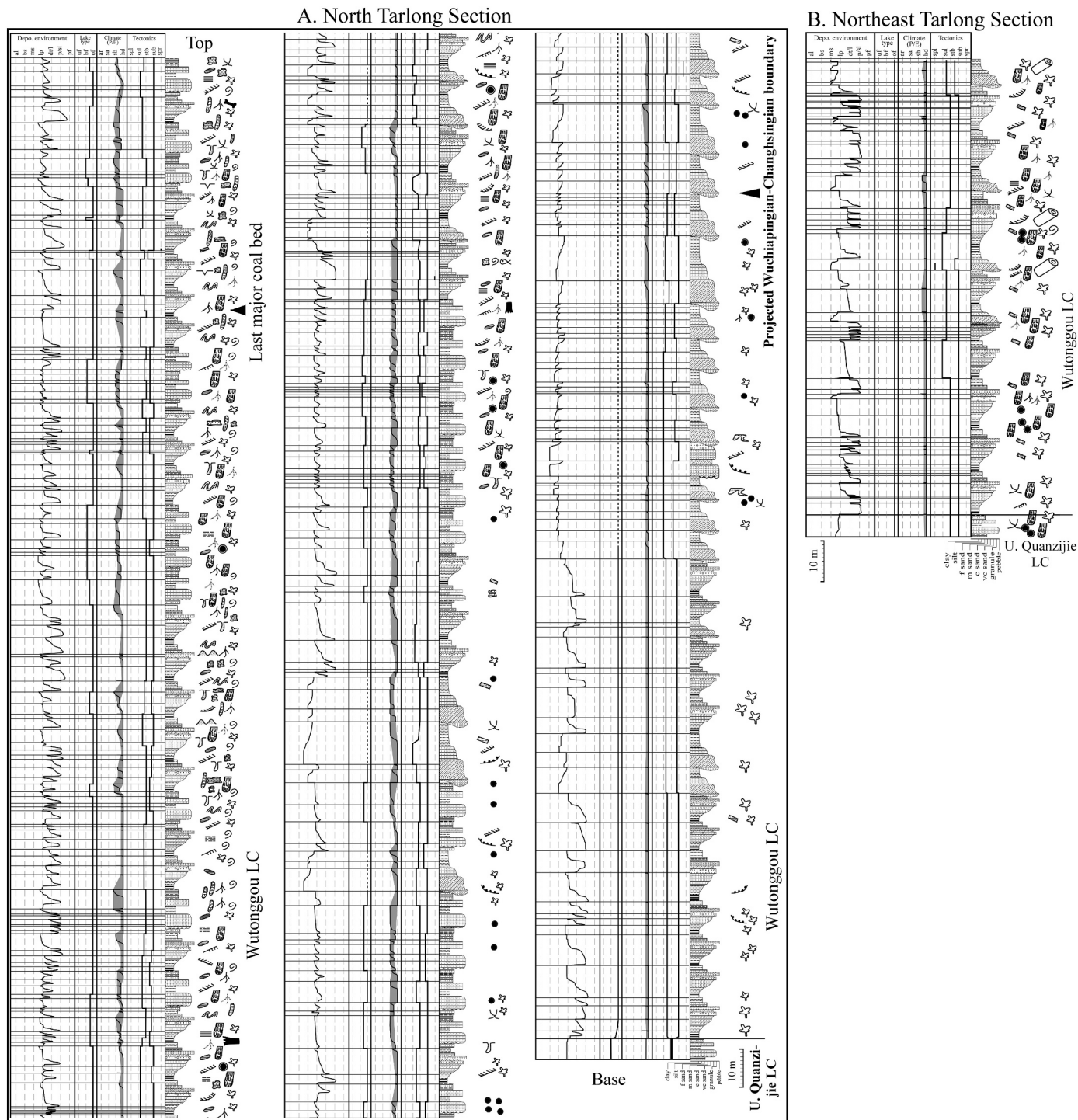


**Fig. 6.** Highly-simplified north, northeast, south, and southwest Tarlong sections (A, B, C, D, respectively), in which depositional environment, lake type, paleoclimatic condition, tectonic movement of the source area and depositional site, and cyclostratigraphy (left panel) and lithologic column, sedimentary structures, and chronostratigraphic boundaries (right panel) of upper Permian–Lower Triassic deposits are shown. Dashed lines are tentative interpretations. The lithologic columns are replaced by simplified high-order cycle types, because the cm-scale field measurements cannot be displayed legibly in the figure. The gray-colored portion of the climate curve is constructed by connecting the most arid and most humid points of adjacent high-order cycles to outline qualitatively long-term climate variations at the low-order cycle scale. See Fig. S1A–G for detailed location, litho-column, and description of the sections, Fig. 3 and Table 1 for age data, and Fig. 4 for additional explanations.

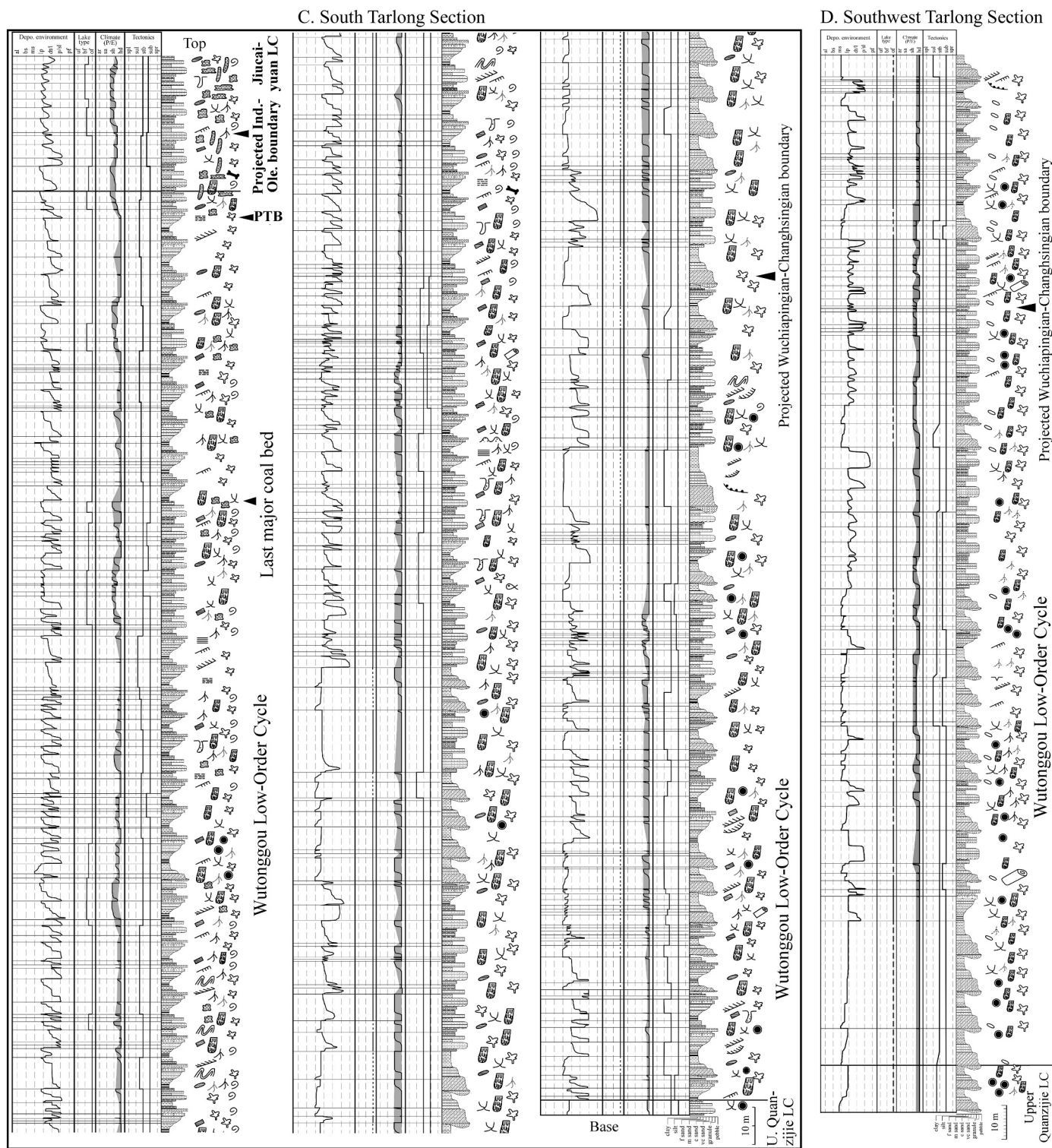


**Fig. 6.** (continued).

Wuchiapingian-Changhsingian boundary at 64.7, 56.5, and 89.7 m above the base of Wutonggou LC, respectively. In the above calculations, the top and base of the Wutonggou LC are assumed to be synchronous in these sections. The position of the PTB in the south and north Tarlong and south Taodonggou sections is calibrated from the age model (Fig. 3). It is estimated for the other sections using an average sedimentation rate (92.12 m/Ma) for the upper interval from samples S19-4 and S12-7 in the age model. The calculated thickness between the PTB and the top of Wutonggou LC is 49.93 m, using an age of 251.902 Ma and a median age of 251.36 Ma as in the south Taodonggou section (Table 1) for the two surfaces, respectively. This thickness is used to project the position of PTB below the top of Wutonggou LC in the central Taodonggou, south Dalongkou, and Zhaobishan sections by assuming that the top of the LC is synchronous in these sections. Here, a single average-sedimentation rate is used because the lithology and depositional environment in the upper part of the Wutonggou LC are similar in all the sections (see below).

The Wutonggou LC ranges from 287.5 to 836.0 m in thickness, and is thickest in the Tarlong area and thinnest in the Taodonggou and Dalongkou areas (Figs. 2, 10). The LC base is a sharp lacustrine transgressive surface overlying floodplain Gleysols of the upper Quanzijie LC (Obrist-Farner and Yang, 2016) or braided stream conglomerates in Zhaobishan (Fig. 4G). Its top is a fluvial channel erosional surface underlying meandering stream deposits of the Jiuciyuan LC in many sections, or a gradational contact in the south Tarlong and south Dalongkou sections, across which the proportion of mature Calcisols increases significantly (Fig. 10).

The Wutonggou LC was deposited dominantly in lacustrine deltaic and lakeplain-littoral environments, and rarely in meandering and braided streams (Figs. 6A–D, 7A–C, 8A–B, 9, 10, 13A; see detailed descriptions in Figs. S1A–C, S2A–C, S3A–C, S4A–C). Lithologies are generally gray, greenish gray, or green, and become increasingly light gray and drab in the uppermost part. Overall, the volume of conglomerate and sandstone decreases upward. Meandering stream HCs are present mainly in the lower part, and are commonly stacked to interrupt lacustrine successions. HCs are commonly thick, in the order of 10s of meters, with well-developed overbank deposits. However, the dominant types of HCs vary between sections (Fig. 13B). In the Tarlong-Taodonggou area, the Tarlong sections contain dominantly thick deltaic and common meandering stream HCs. This contrasts sharply with the central Taodonggou section, where lakeplain-littoral cycles dominate. The contrast signifies the stratigraphic variability in environment, depositional system, and thickness within a single half graben, where the Tarlong sections are located in the axial depocenter and the Taodonggou sections at the ramp margin (Yang et al., 2010). The Dalongkou sections are similar to the Taodonggou sections, and contain abundant thin lakeplain-littoral and deltaic and a few meandering stream HCs (Fig. 13B). The Zhaobishan section contains the greatest volume of conglomerate and sandstone in comparison to the other sections (Figs. 9, 10, 13B). Braided and coarse-grained meandering stream HCs are common and overlain by a thick retrogradational succession of individual coarsening-upward littoral-beach and deltaic HCs, forming thick transgressive systems tracts of intermediate-order cycles (Fig. 4J; Yang et al., 2015). The delta-front sandstones and conglomerates are commonly well-washed and stratified, and interpreted as wave-dominated deltaic deposits. The thick transgressive coarse-grained beach-littoral and wave-dominated deltaic deposits, along with the presence of braided and coarse-grained meandering stream deposits, are used to interpret a relatively steep topographic gradient in the Zhaobishan area (Yang et al., 2015; see also Zheng and Yang, 2020).

The abundance of deltaic and meandering stream deposits, as well as the rarity of coquinas (e.g., Brand et al., 1993), indicate that the Wutonggou sediments were deposited in open lakes and perennial streams (Fig. 10). For the fluvial HCs, the type of nearby coeval lakes is

postulated on the basis of paleosol types developed in the overbank deposits. However, deltaic HCs become thinner; and some calcareous Protosols and poorly to moderately-developed Calcisols start to appear and gradually increase in the uppermost part of the LC (Fig. 10). This indicates that the lakes became less open in the late Wutonggou time of the early–mid Induan.

The tectonic movement in the source areas and depositional sites varied during the deposition of the Wutonggou LC (Fig. 10). Where a thick succession of fluvial and deltaic gravel and coarse-sand deposits overlies mud-rich intervals, there is evidence for significantly increased siliciclastic input to the depositional site. This was probably caused by tectonic uplift in the source area and resulting increase in topographic gradient of the drainage basin. In several cases, a thick succession of stacked channel-fill conglomerates and sandstones overlies sublittoral muddy deposits with an erosional contact of significant relief. This may have been the result of a catastrophic collapse of the lake-spill point. On the other hand, the great thickness of the Wutonggou LC, especially in the Tarlong and Zhaobishan areas, indicates that the depositional sites had experienced intense subsidence during most of Wutonggou time (Fig. 10). A succession of thick HCs of any type indicates ample accommodation space for sediment accumulation and increased subsidence that allowed for sediment preservation. In several cases, thick sublittoral muddy deposits abruptly overlie fluvial and lake margin sediments, indicating rapid deepening. This may have been caused by an uplift of the lake spill point. Alternatively, the rapid deepening may have been caused by a rapid transgression of shoreline and lake expansion resulting from a sudden increase in precipitation. But such an event would have been short-lived. Any sudden displacement of a hanging wall basin floor due to normal faulting in a rift setting is common and would have greatly changed the elevation of the spill point of an open lake, although this scenario is difficult to document in deep time sedimentary records.

Several lines of evidence point to overall humid-subhumid conditions during the Wutonggou time, beginning in the late Wuchiapingian and continuing into the mid-Induan. The conditions gradually became more variable and, in some intervals, shifted to subhumid-semiarid in the uppermost part of the LC (Fig. 10). A humid-subhumid condition implies a P/E (precipitation/evaporation) ratio greater than one and a surplus in moisture. The abundance of deltaic deposits in over-filled lakes requires a constant influx of sediment-laden river water into the lakes. The development of thick meandering stream HCs with a significant proportion of overbank deposits requires perennial river flow in a stable catchment basin, and intense source denudation and weathering under a humid climate (Miall, 1996). The common to abundant disseminated plant debris and carbonaceous shale and sporadic occurrence of coals in fluvial and lacustrine deposits, along with the occurrence of permineralized wood throughout the Wutonggou LC, reflect the presence of a lush vegetation cover in the riparian and upland areas (e.g., Wan et al., 2019d). Finally, Gleysols, Argillisol, and Histosols occur throughout the Wutonggou LC, indicating a humid-subhumid condition (Table 2 of Yang et al., 2010; Thomas et al., 2011). The formation of a specific paleosol is controlled by numerous factors and may not reflect regional climatic conditions (Retallack, 1990; Mack and James, 1994). However, the trend of successive paleosols likely shows the long-term regional climate (e.g., Gastaldo et al., 2020a, 2020b). Hence, the wide occurrence of Gleysols, Argillisol, and Histosols in the Wutonggou LC supports an interpretation for persistent humid-subhumid conditions. Calcareous Argillisol and Protosols and poorly-developed Calcisols, however, begin to appear and gradually increase in the uppermost part of the Wutonggou LC; these are interspersed with non-calcareous paleosols. This change in paleosol type is accompanied by a decrease in well-developed deltas and an increase in lakeplain-littoral HCs. This trend indicates an increased climatic variability and a gradual shift to a relatively drier condition in the upper part of the Wutonggou LC (Fig. 10).

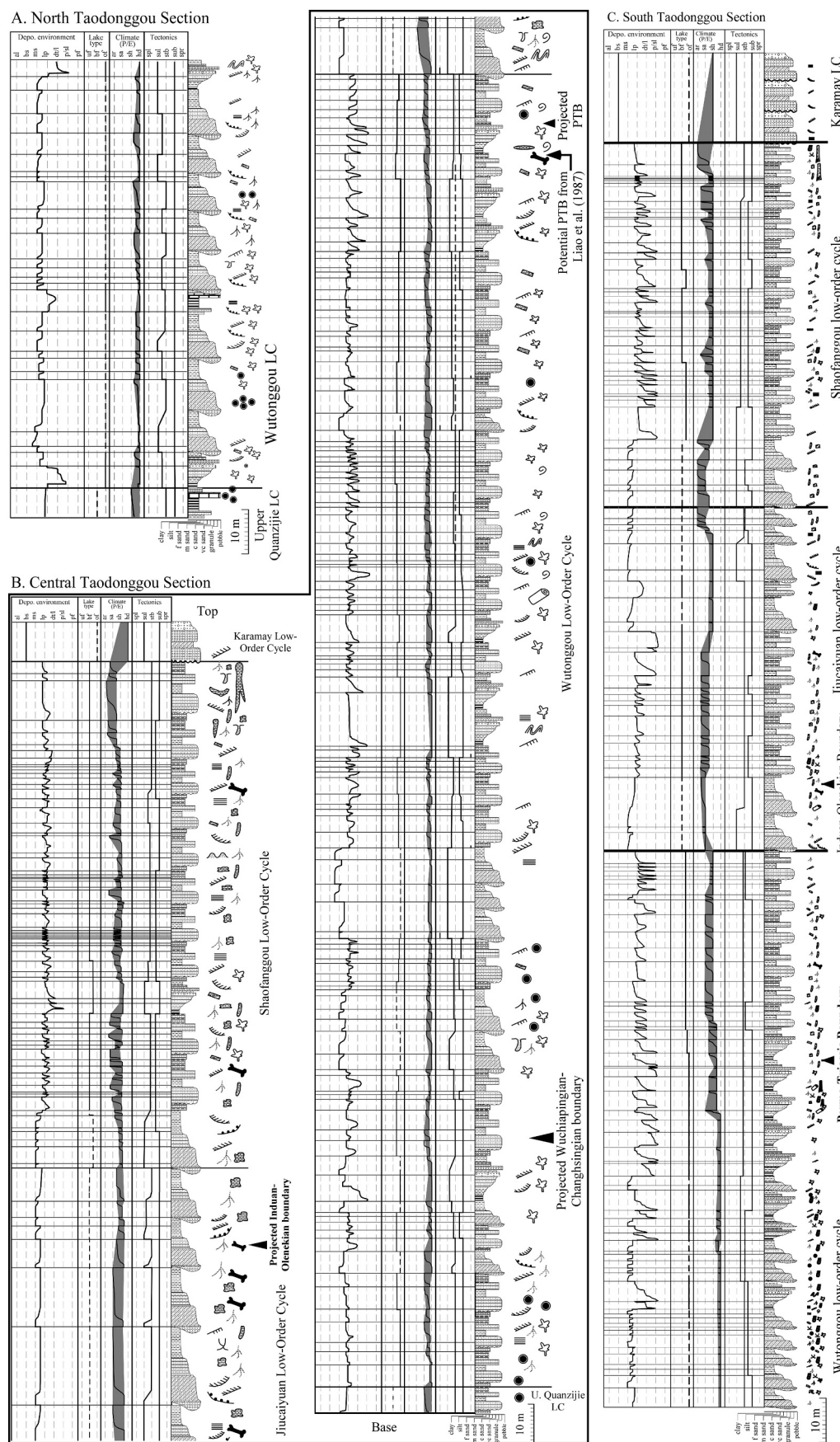
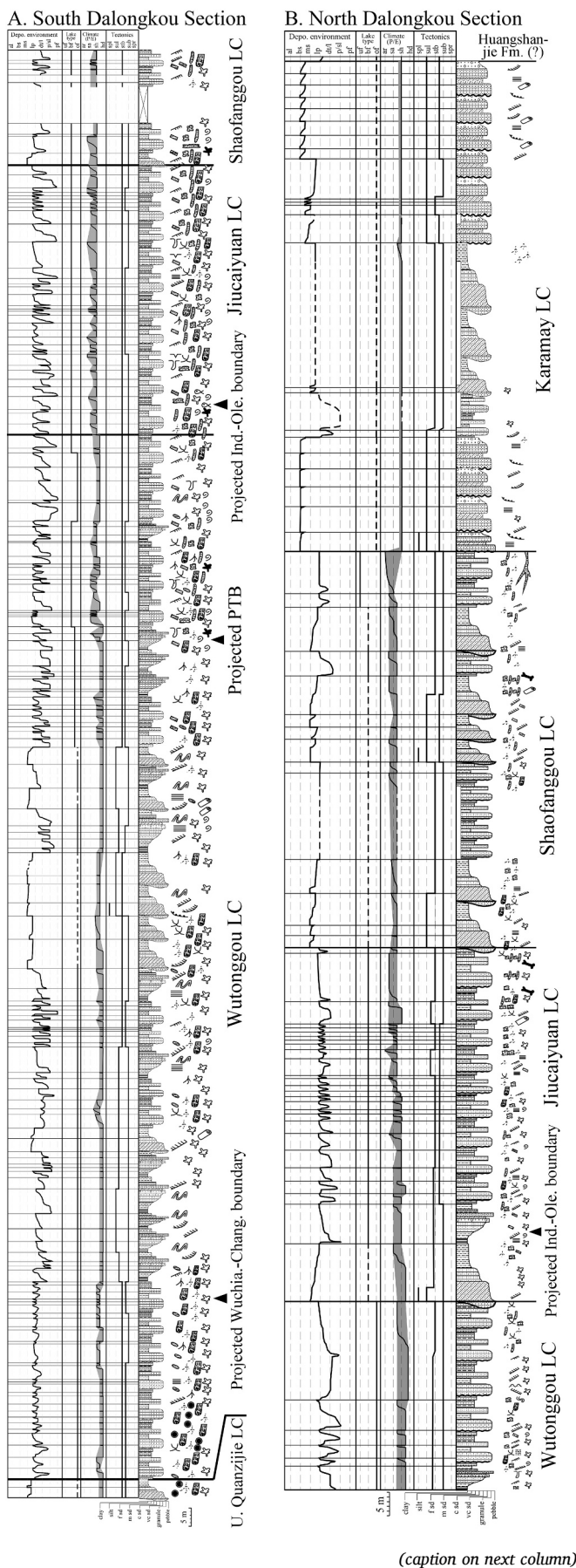


**Fig. 7.** Highly-simplified north, central, and south Taodonggou sections (A, B, C, respectively), in which depositional environment, lake type, paleoclimatic condition, tectonic movement of the source area and depositional site, and cyclostratigraphy (left panel) and lithologic column, sedimentary structures, and chronostratigraphic boundaries (right panel) of upper Permian–Lower Triassic deposits are shown. See Fig. S2A–E for detailed location, lithologic column, and description of the sections, Fig. 3 and Table 1 for age data, and Figs. 4 and 6 for explanations.



*(caption on next column)*

**Fig. 8.** Highly-simplified south and north Dalongkou sections (A, B, respectively), in which depositional environment, lake type, paleoclimatic condition, tectonic movement of the source area and depositional site, and cyclostratigraphy (left panel) and lithologic column, sedimentary structures (right panel), and chronostratigraphic boundaries of upper Permian–Lower Triassic deposits are shown. The Middle-Triassic Karamay low-order cycle is also depicted in (B). See Fig. S3A–E for detailed location, lithologic column, and description of the sections, and Figs. 4 and 6 for explanations.

Precipitation seasonality in the Wutonggou LC can be assessed using several proxies. First, the large volume of siliciclastic sediments indicates the presence of a large sediment yield in the source area, which is likely to be produced under a strongly seasonal climate (Schumm, 1968; Yang, 1996). Second, the growth rings in permineralized gymnosperm trees developed under strong precipitation seasonality. In the Wutonggou LC, some specimens of the wood display clear growth rings, indicating strong seasonality, whereas others do not, suggesting weak or no seasonality (Wan et al., 2014, 2016a, 2016b, 2017a, Wan et al., 2020, 2021a, 2021b, and unpublished data). Finally, Vertisols and vertic structures, such as soil slickensides and clastic dikes, indicate a pronounced precipitation seasonality (Yang et al., 2010; Thomas et al., 2011). They are scattered and impersistent in the Wutonggou LC. Above all, precipitation seasonality had probably varied from weak to strong and shows a clear trend during the Wutonggou time.

Climatic variability is well documented by two contrasting and persistent paleosols, a Calcisol zone and a coal bed (Fig. 10). The Calcisol zone contains two to three stacked mature Calcisols (Fig. 4H). These are prominent amid the sub- and super-adjacent intervals containing humid paleosols. The zone is synchronous between the north and south Tarlong sections because the bentonites occurring directly above the zone provide a similar age,  $252.64 \pm 0.12$  Ma in north Tarlong and  $252.66 \pm 0.05$  Ma in south Tarlong (Figs. S1D, S1F). The zone is tentatively correlated with one in the Zhaobishan section (Fig. 4H), a zone of moderately-developed Calcisols in central Taodonggou, and calcic Argillisols in south Dalongkou (Figs. 10, 2D, 3E). This Calcisol zone represents a significant short-term climate perturbation toward a subhumid-semiarid condition. In contrast, the persistent coal bed (i.e., Histosol) in the upper Wutonggou LC ranges from 1 to 2 m thick and is the uppermost major coal occurrence in the Tarlong-Taodonggou area. It has an estimated age of 252.29 Ma (Table 1; Fig. 3). This distinct coal bed is tentatively correlated with intervals containing concentrated thin lignites and carbonaceous shales in the central Taodonggou, south Dalongkou, and Zhaobishan sections (Fig. 10). It indicates that the humid-subhumid condition persisted into the late Wutonggou time, albeit with a gradual change to a drier condition.

The interpretation of climate based on sedimentary evidence in this study expands on those of [Yang et al. \(2010\)](#) and [Thomas et al. \(2011\)](#); see also [Brand et al., 1993](#)) from the north and south Tarlong and central Taodonggou sections. These are extended into south Taodonggou, Dalongkou, and Zhaobishan, and present a regional pattern constrained by the age model. In general, all areas show a similar trend of a generally humid-subhumid condition with variable precipitation seasonality and a gradual change toward subhumid-semiarid conditions in the late Wutonggou time of early-mid Induan age. The Zhaobishan section, however, does not show an apparent gradual shift to a more seasonally dry condition ([Fig. 10](#)). This may be related to its upland location, where sedimentation was less sensitive to climate variations and/or that a large and fast sediment accumulation may have masked the signals of weak climatic perturbations.

The Wutonggou LC produces rare fossil vertebrates (e.g., Cheng et al., 1996; Lucas, 2001; Huang et al., 2021), of which those in the upper part of the LC (i.e., the traditional Guodikeng Formation) are the most common and most thoroughly studied. The latter assemblage includes the dicynodonts *Diictodon*, *Jimusaria*, *Turfanodon*, and *Lystrosaurus*, the theropcephalian *Dalongkoua*, and a bystrowianid chroniosuchian (Cheng et al., 1996; Lucas, 2001; Angielczyk and Sullivan, 2008;

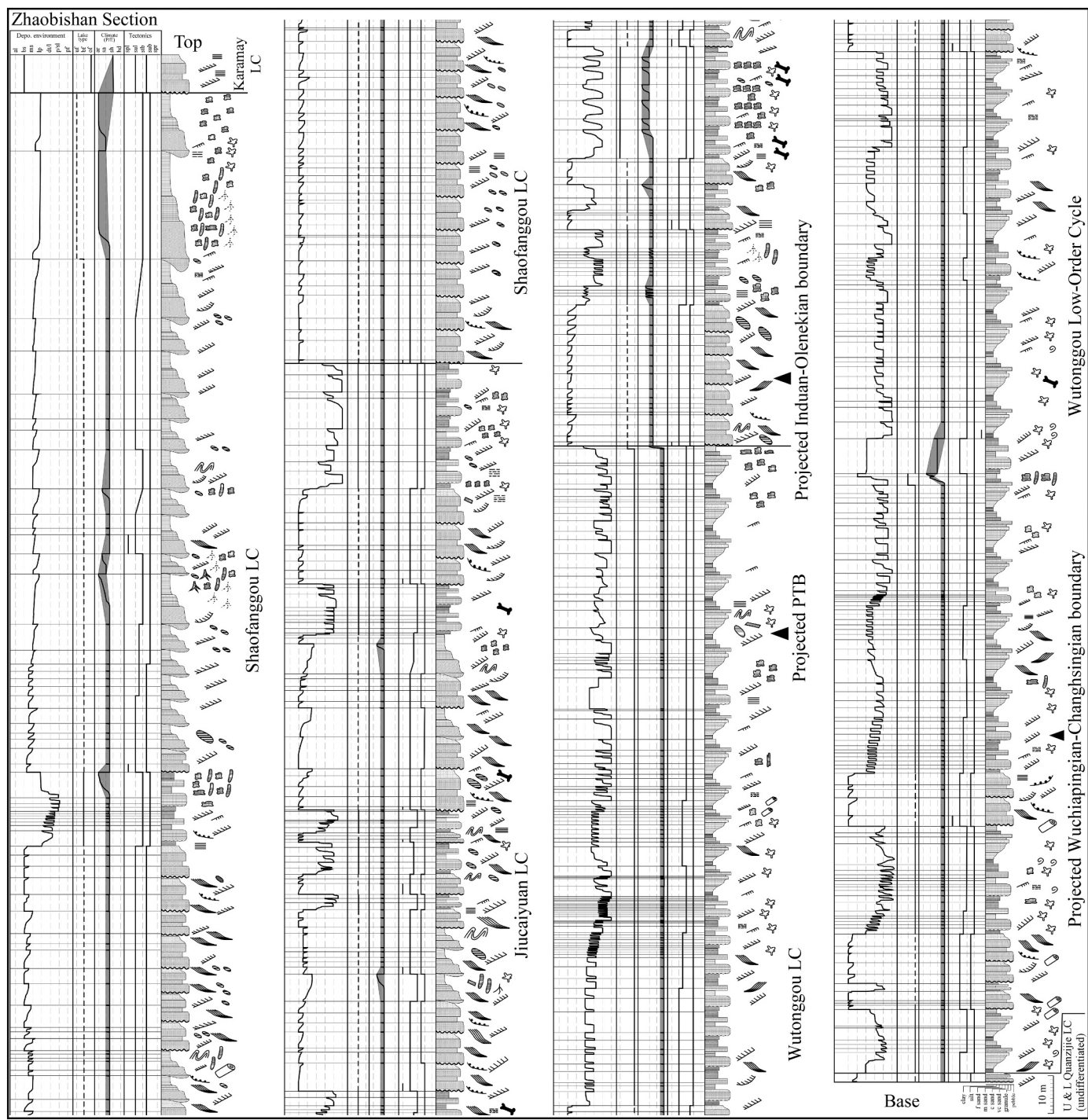


**Fig. 9.** Highly-simplified Zhaobishan section in which depositional environment, lake type, paleoclimatic condition, tectonic movement of the source area and depositional site, and cyclostratigraphy (left panel) and lithologic column, sedimentary structures, and chronostratigraphic boundaries (right panel) of upper Permian–Lower Triassic deposits are shown. See Fig. S4A–D for detailed location, litho-column, and description of the sections, and Figs. 4 and 6 for explanations.

Kammerer et al., 2011; Liu and Abdala, 2017; Liu, 2021). The co-occurrence of the *Dicynodon*-grade dicynodontoid *Jimusaria* with *Lystrosaurus* in the uppermost Wutonggou LC has received considerable attention in the context of the placement of the Permo–Triassic boundary in the Bogda Mountains sections (e.g., Cheng, 1993; Cheng and Lucas, 1993; Lucas, 2001; Metcalfe et al., 2009; Liu and Abdala, 2017) because of a similar stratigraphic overlap between *Dicynodon*-grade

dicynodontoids and *Lystrosaurus* near the Permo–Triassic boundary in the Karoo Basin of South Africa (e.g., Smith and Ward, 2001; Ward et al., 2005; Smith and Botha-Brink, 2014; Botha et al., 2020; Viglietti, 2020; Viglietti et al., 2021; cf. Gastaldo et al., 2021). This overlap is generally considered to occur only in the Permian in South Africa (e.g., Ward et al., 2005; Smith and Botha-Brink, 2014; Viglietti, 2020; Gastaldo et al., 2020a, 2020b), with *Dicynodon*-grade dicynodontoids becoming

extinct by the end of the Permian. However, the stratigraphic framework and age model presented here raises the possibility that *Dicynodon*-grade dicynodontoids survived into the Early Triassic in Xinjiang, a possibility also hinted at by occurrences in Laos (Olivier et al., 2019), as well as an Early Triassic Karoo detrital zircon age presented by Botha et al. (2020). Further investigation of this possibility is warranted.

In summary, the Wutonggou LC in the three areas is composed of fluvial-lacustrine siliciclastic deposits with significantly different stratigraphic thicknesses (Fig. 10). The LC in the Tarlong sections was probably deposited in the axial depocenter, in contrast to the ramp margin in the Taodonggou sections of the Tarlong-Taodonggou half graben (Yang et al., 2010). The LC in Dalongkou probably was also

deposited on the ramp of a half graben (Obrist-Farner and Yang, 2017; Zheng and Yang, 2020). The Zhaobishan area was in a more upland locality and closer to the North Tianshan suture relative to the other two areas (Zheng and Yang, 2020). As a result, the climate conditions in Zhaobishan were more stable during the deposition of the Wutonggou LC.

## 5.2. Jiucaiyuan low-order cycle

The Jiucaiyuan LC spans the middle Induan to early Olenekian (251.36 to 250.53 Ma; ICS, 2020; cf. Ogg et al., 2020) for about 0.83 Ma in the south Taodonggou section (Table 1; Figs. 2, 3). Alternatively, the

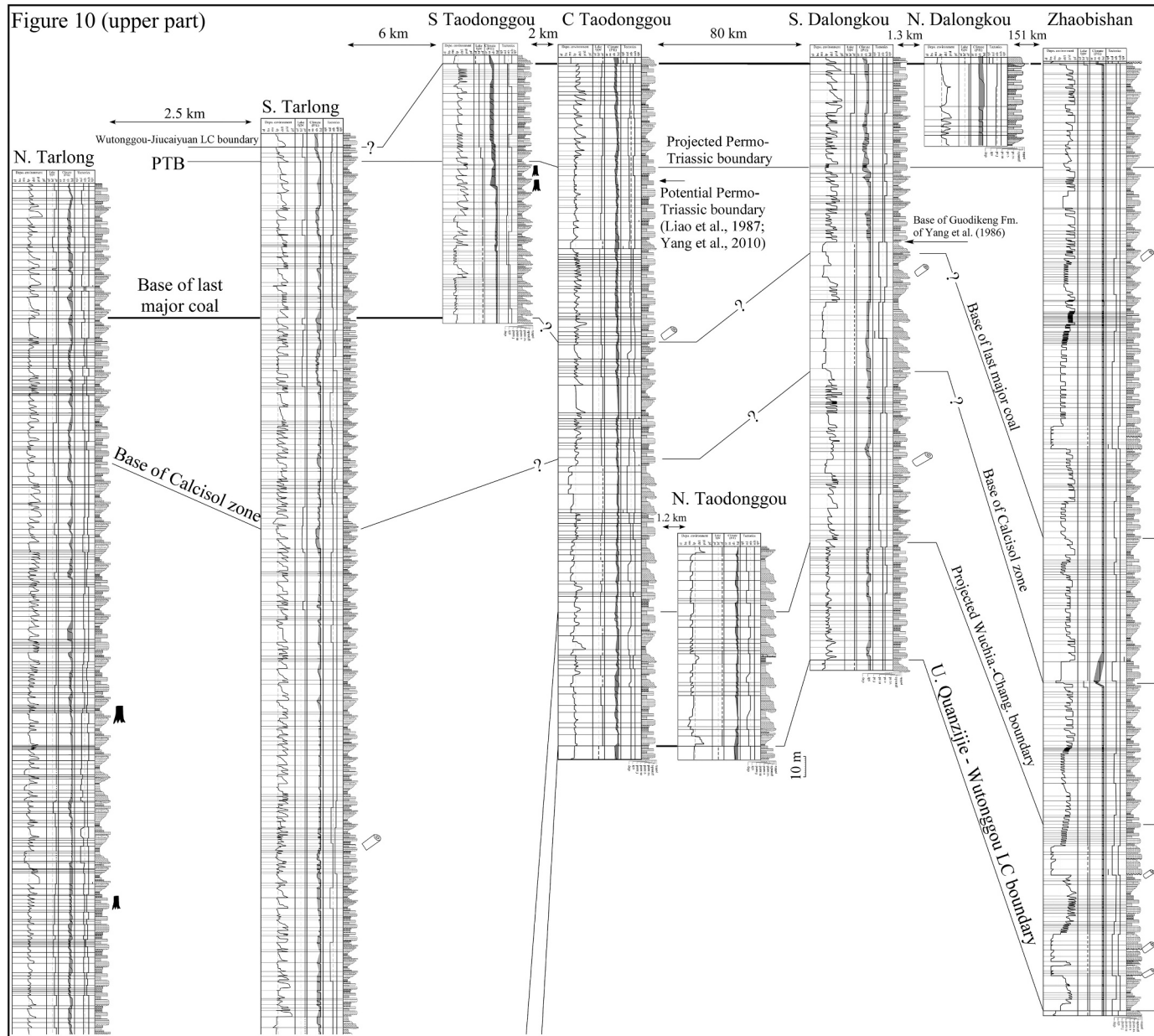


**Fig. 10.** Stratigraphic correlation of the upper Wuchiapingian to middle Induan Wutonggou low-order cycle, showing 1–100-km stratigraphic variability in depositional environment, lake type, and climatic and tectonic conditions. The position of the Permian–Triassic boundary from the age model in south Tarlong and south Taodonggou sections is projected using an average sedimentation rate into the other sections and is correlated. The bases of a major Calcisol zone and the last major coal bed in upper Wutonggou (question marked where the occurrences are speculated; see text for discussion) also act as datums. The position of the Wutonggou–Guodikeng formation boundary of Yang et al. (1986) is marked on the south Dalongkou section. The position of Permian–Triassic Boundary interpreted by Liao et al. (1987) and adapted by Yang et al. (2010) is marked on the central Taodonggou section. Occurrences of some permineralized wood are marked. Multiple correlation datums (thick correlation line) are used. See Figs. 6–9 for individual simplified sections, Figs. 1 and S1–S4 for locations and detailed stratigraphy of individual sections, and Fig. 4 for explanations.

Figure 10 (Lower part)

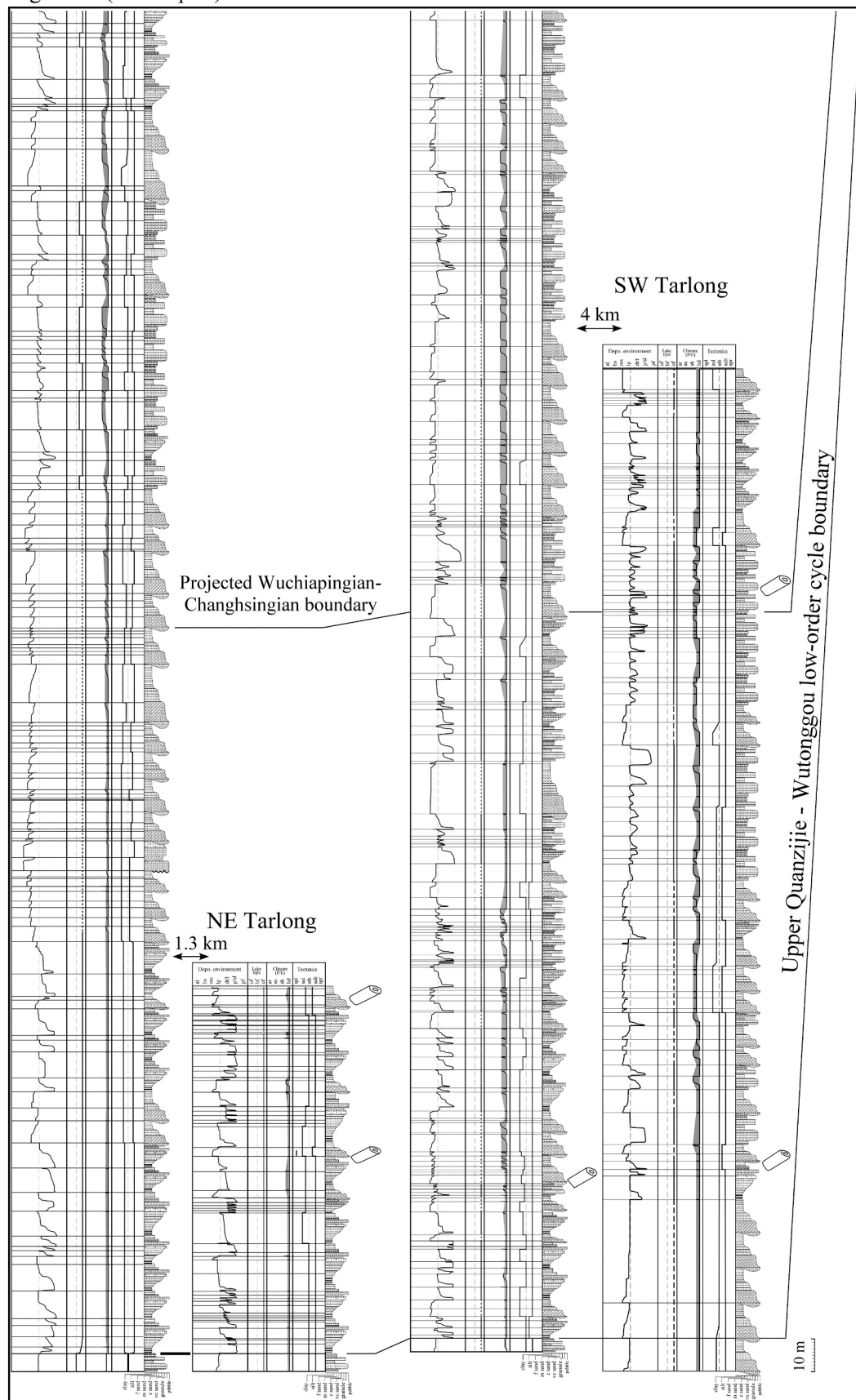
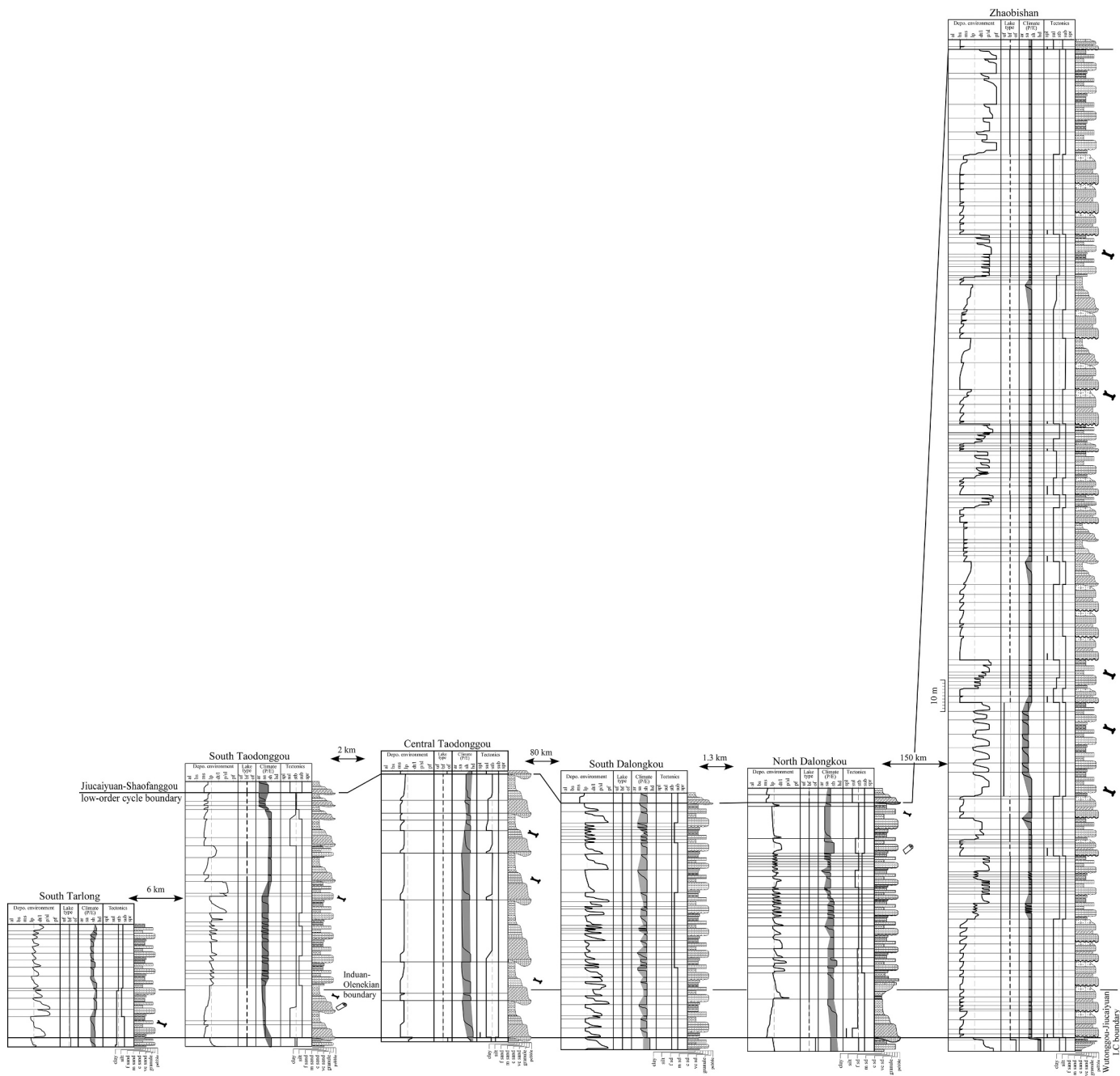


Fig. 10. (continued).



**Fig. 11.** Stratigraphic correlation of the upper Induan-lower Olenekian Jiucaiyan low-order cycle, showing 1–100-km stratigraphic variability in depositional environment, lake type, and climatic and tectonic conditions. The position of the Induan–Olenekian boundary from the age model in the south Taodonggou section is projected using an average sedimentation rate into the other sections and is correlated. Occurrences of some permineralized wood and vertebrate fossils are marked. The base of Jiucaiyan low-order cycle is the correlation datum. See Figs. 6–9 for individual simplified sections, Figs. 1 and S1–S4 for locations and detailed stratigraphy of individual sections, and Fig. 4 for explanations.

duration is estimated to be 0.96 Ma from the base of the Jiucaiyan in the south Tarlong section (251.79 Ma) to the top of the cycle in the south Taodonggou section. The latter estimate is not preferred because only the lower part of the Jiucaiyan is exposed in south Tarlong (see “Discussion”). The cycle contains the Induan–Olenekian boundary in the south Taodonggou section as calibrated using the age model and the age of Olenekian Stage of ICS (2020); the position of the boundary is projected at 14.7 m above the base of the Jiucaiyan LC using an average sedimentation rate of 92.12 m/Ma (see previous section; Fig. 11). The projection assumes that the base of the Jiucaiyan LC is synchronous in

all sections. The Jiucaiyan LC ranges in thickness from 74.1 to 83.3 m in the south and central Taodonggou and the south and north Dalongkou sections, but attains a thickness of 312.3 m in the Zhaobishan section (Figs. 2, 11). Its lower boundary is the base of a fluvial channel cut into underlying lake margin deposits of the Wutonggou LC in the south and central Taodonggou, north Dalongkou, and Zhaobishan sections. It is a sharp contact separating underlying from overlying lake margin deposits in the south Tarlong and south Dalongkou sections. In both cases, the number of mature Calcisols increases significantly across the cycle base (Fig. 11). Hence, the base represents a regional peneplanation and

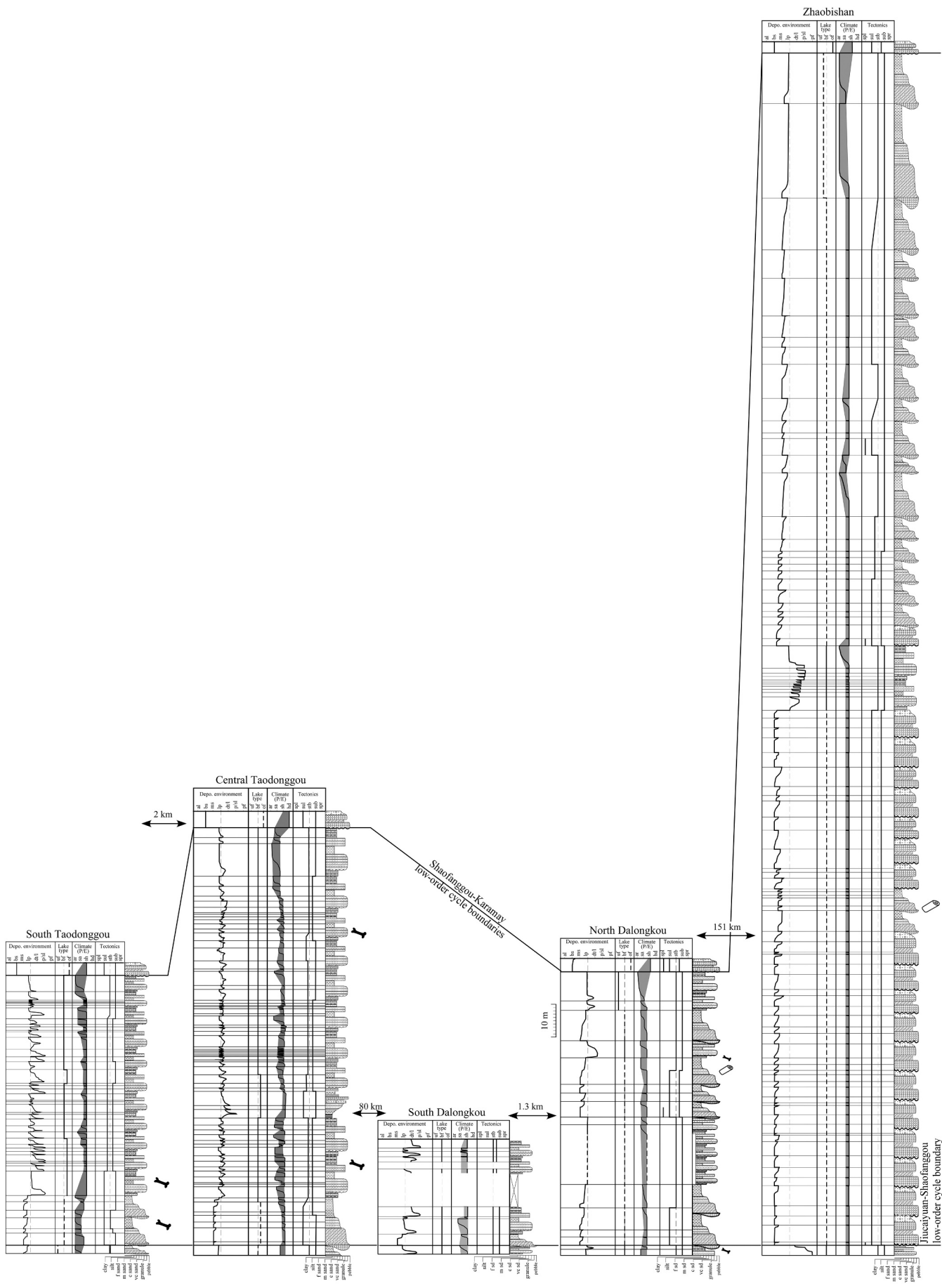


**Fig. 12.** Stratigraphic correlation of the lower Olenekian Shaofanggou low-order cycle, showing 1–100-km variability in depositional environment, lake type, and climatic and tectonic conditions. Occurrences of some permineralized wood and vertebrate fossils are marked. The base of Shaofanggou low-order cycle is the correlation datum. See Figs. 6–9 for individual simplified sections, Figs. 1 and S1–S4 for locations and detailed stratigraphy of individual sections, and Fig. 4 for explanations.

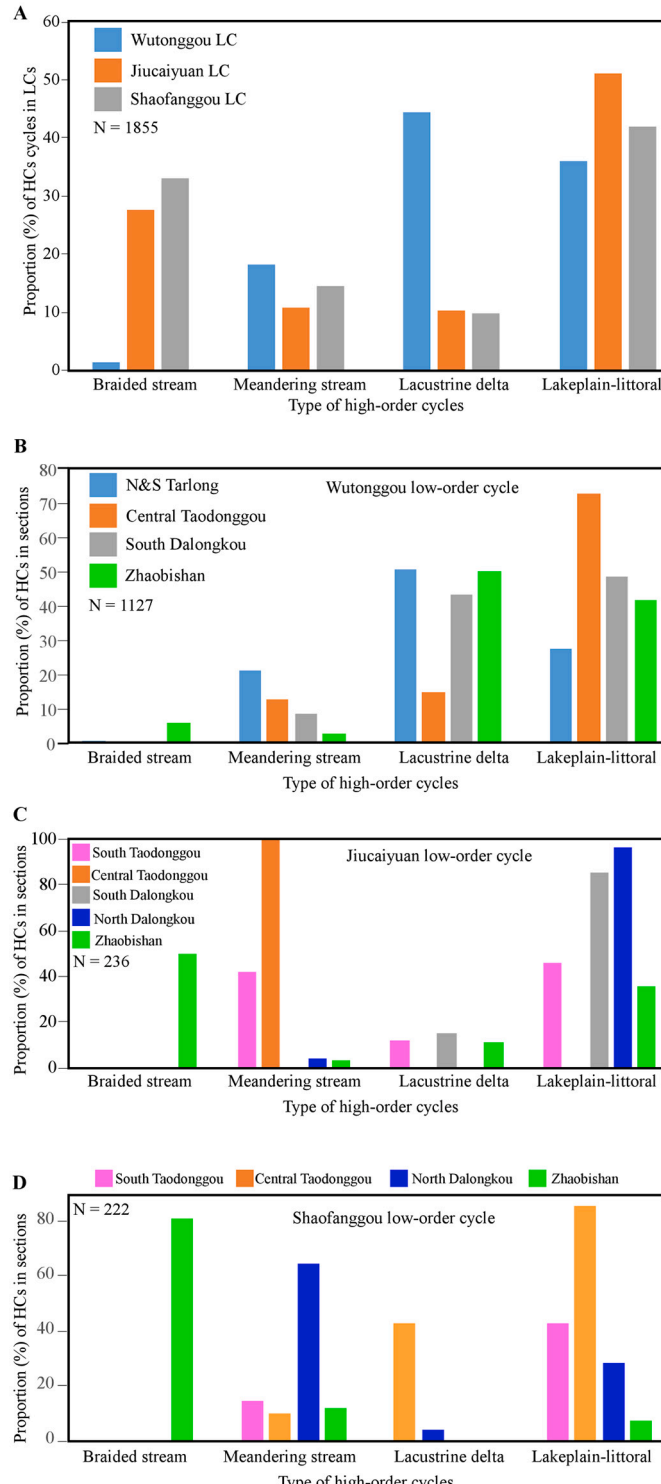


**Fig. 13.** Histograms showing the relative abundance of four types of high-order cycles (HCS) in the Wutonggou, Jiuciyuan, and Shaofanggou low-order cycles (LCs) in all sections (A) and in complete sections for the three LCs (B, C, D), to demonstrate the spatial and temporal variability in lithofacies and depositional environment. See Fig. 4 for high-order cycle types.

the onset of a dominantly subhumid-semiarid climate. It is interpreted as a conformity, or a diastem, with a small and variable amount of missing time. This interpretation is based on the overall gradational changes of environments and climatic and tectonic conditions recorded in the stratigraphy. The top of the Jiuciyuan LC is marked by the base of a high-relief fluvial channel in all sections, juxtaposing lakeplain to sublittoral deposits in the north and south Dalongkou, and Zhaobishan sections (Figs. 8A, B, 9, S3D, S3E, S4D), and thick overbank deposits in the south and central Taodonggou sections (Figs. 7B, C, S2D, S2E) with overlying fluvial conglomerates and sandstones of the Shaofanggou LC.

The Jiuciyuan LC is composed mainly of lakeplain-littoral and braided stream, several meandering stream, and a few lacustrine deltaic HCs (Fig. 13A). The LC is characterized by colors of dark reddish brown, maroon, grayish red and purple for mudrock-rich intervals, and gray, greenish gray to drab colors for sandstone and conglomerate intervals (Figs. S1A–C, S2A–C, S3A–C, S4A–C). These colors contrast with those of the generally gray and greenish gray rocks of the Wutonggou LC. Overall, the proportion of conglomerate and sandstone decreases upward.

The dominant types of HCs vary significantly among the sections (Fig. 13C). For example, the central Taodonggou section is composed entirely of meandering stream HCs, many of which have extremely thick overbank deposits. In contrast, the south Taodonggou section, only 2 km to the south, has one such thick meandering stream HC in the basal part, mainly lakeplain-littoral and a few deltaic HCs in the middle interval, and a succession of thick meandering stream HCs in its upper part (Fig. 7B, C). Calcisols are well developed in thick overbank and marginal mudflat deposits throughout both sections, signifying a stable landscape after initial peneplanation. Hence, the central Taodonggou area was probably located slightly upslope on the ramp margin of the half graben relative to the south Taodonggou area. As a result, only fluvial sedimentation occurred at central Taodonggou, while mixed fluvial and lacustrine sedimentation at south Taodonggou. The upslope location of the central Taodonggou area makes it less sensitive to environmental shifts associated with lake expansion and contraction compared to the south Taodonggou area in a downslope position. As a result, the central Taodonggou section only records 10 HCs, whereas 26 HCs are preserved in the south Taodonggou section, even though the former is ~6 m thicker (Figs. 2, 11). The difference in the number of HCs and their thickness indicates that the south Taodonggou section has a higher stratigraphic resolution than the central Taodonggou section. On the other hand, the south and north Dalongkou sections are not significantly different from each other. The south section records only lakeplain-littoral HCs; the north section has only one thick meandering stream HC at its base, and the remainder of the stratigraphy is comprised of lakeplain-littoral HCs. This indicates that both sections were located on the ramp margin with a similar elevation and proximity to the lake, even though the north Dalongkou section was initially at a topographically higher position.

Finally, the Jiuciyuan LC in the Zhaobishan section is significantly different from those in both the Taodonggou and Dalongkou sections. Here, there is a large proportion (50%) of braided stream and lakeplain-littoral HCs (35%), which form alternating fluvial-lacustrine intermediate-order cycles (Figs. 9, 11, 13C). There are 12 thick successions of stacked braided and coarse-grained meandering stream HCs. For example, a 40-m thick succession occurs at the base of the LC, where granite gravels appear for the first time and persist throughout the LC, signifying significant uplift and lithologic change of the provenance in the North Tianshan suture zone to the south (Figs. 9, S4D; Zheng and

Yang, 2020). These successions are commonly overlain by stacked beach-littoral coarsening-upward HCs, each with a sharp contact. These form an overall fining-upward retrogradational interval during lake shoreline transgression and expansion, similar to those in the underlying Wutonggou LC. Yang et al. (2015) interpreted the presence of a steep lake margin that was the major factor responsible for the formation of thick coarse-grained transgressive deposits, which would have stalled or slowed shoreline transgression to trap and accumulate a large quantity of coarse-grained siliciclastic sediments (see also Li et al., 2019, their Fig. 15). The transgressive intervals are, in turn, overlain by mudrock-dominated deltaic and lakeplain-littoral HCs formed during maximum lake expansion and early contraction. The limited sand-and-gravel deposits and poorly-developed delta-front facies in the phase of maximum expansion and early contraction indicate that there was a limited supply of coarse siliciclastic sediments to the depositional site. This may have been caused by a geographically extensive maximum shoreline transgression that prevented delivery of coarse siliciclastic sediments from the lake margin to the site, and/or a greatly reduced sediment production and stream transport capability during the period of early contraction due to an increasingly seasonally arid climate (see below). In some cases, it is apparent that the ensuing fluvial erosion may have removed some deltaic sediments.

The overall limited volume of meandering stream and deltaic deposits in the Jiucayuan LC indicates that the Jiucayuan lakes were not over-filled (Fig. 11). On the other hand, the absence of lacustrine limestone and evaporites indicates that the lakes were not under-filled. Calcisols are well-developed in overbank deposits of meandering streams as well as on marginal mud and sand flats. This is used to interpret a prevailing subhumid-semiarid conditions and an overall balance of precipitation and evaporation. Thus, the Jiucayuan lakes are interpreted as dominantly balance-filled (Carroll and Bohacs, 1999).

Regional tectonism in the source areas varied during Jiucayuan time beginning in the mid-Induan and continuing into the early Olenekian (Fig. 11). A shift from lacustrine to fluvial deposition across an erosional base in the north and south Taodonggou, north Dalongkou, and Zhaobishan areas points to the uplift and exhumation of the source areas and regional peneplanation in the catchment basin. The uplift, however, apparently did not significantly affect sedimentation in the south Tarlong and south Dalongkou areas. The extremely thick succession of stacked braided streams and the first appearance of granite gravels in the Zhaobishan area indicate that the uplift was rapid (Figs. 9, 11, S4D; Zheng and Yang, 2020). The juxtaposition of littoral-sublittoral deposits with overlying coarse fluvial channel fills is interpreted to reflect collapse of lake-spill points in several areas. Spill-point collapse may have occurred as many as nine times in Zhaobishan (Fig. 11). On the other hand, persistent lakeplain-littoral deposition in south Tarlong, south Taodonggou, and the north and south Dalongkou sections, and the development of large meandering streams in central Taodonggou, are evidence for overall tectonic stability of the source areas and moderate to significant subsidence of the depositional sites during most of Jiucayuan time. Subsidence may have been greater during the deposition of thick HCs than that during times of thin HCs, because continuous, uninterrupted sediment accumulation requires a significant and constant increase of accommodation space. The Zhaobishan deposits are about four times thicker than those in the other areas, suggesting much greater overall subsidence in Zhaobishan. In addition, the Zhaobishan section contains as many as twelve braided stream-lacustrine successions. Each succession contains multiple HCs and may have been the result of an episode of intensified uplift followed by a period of quiescence in the source area. Thus, the intermediate-order cyclicity in the Zhaobishan section may be of a tectonic origin. The area was probably closer to the North Tianshan suture zone with a relatively upslope location in the drainage basin, and tectonically more active than the Tarlong-Taodonggou and Dalongkou areas in a more central basinal

setting (Zheng and Yang, 2020; see also Obrist-Farner and Yang, 2017).

Sedimentary evidence indicates that climate conditions during the mid-Induan to early Olenekian were dominantly subhumid to semiarid. These conditions translate to a P/E ratio about one without a net surplus or deficiency in moisture budget (Fig. 11). Rare deltaic, limited meandering stream, and abundant mud-rich lakeplain-littoral HCs provide evidence of limited runoff and influx of sediment-laden water into the lakes (Fig. 13A). However, thick meandering stream HCs are abundant in the central Taodonggou section, common in the south Taodonggou section, and present in other sections. These deposits indicate perennial stream flow and a surplus of moisture and, thus, are probably reflective of a subhumid climate. In contrast, the well-developed Calcisols in overbank deposits indicate a drier, likely semiarid or seasonally dry condition during the late stage of overbank deposition and/or afterward when non-deposition and pedogenesis took place. Thus, intracyclic variations from subhumid to semiarid conditions may be present at the high-order cycle scale. Moreover, in some thin beds, especially the subaerial lake margin transgressive deposits, disseminated plant debris is common or even abundant although well-preserved leaf litters are rare; rhizoconcretions and root molds are common in paleosols; and macro-charcoal is present in the upper Jiucayuan in north Dalongkou (Wan et al., 2021a). These observations indicate the presence of riparian vegetation; however, permineralized wood is rare and likely a taphonomic artifact with the absence of silica-rich groundwater necessary for preservation. The rarity of permineralized wood also may be partially related to the presence of calcite-precipitating environments as indicated by abundant Calcisols and common calcitic rootlets. Vertebrate fossils, mainly *Lystrosaurus*, are common and locally abundant (Liu and Abdala, 2017 and references therein; unpublished data). These animals likely fed on the riparian vegetation.

The most compelling evidence for subhumid-semiarid conditions is the widespread occurrence of moderately to highly mature Calcisols throughout the Jiucayuan LC (Table 2 of Yang et al., 2010; Thomas et al., 2011). In addition, calcareous Protosols and calcareous Argilliscs are common. The Bk horizons of these paleosols contain concentrated and scattered calcitic nodules, rhizoconcretions, and calcite-filled root molds. In some cases, especially in the uppermost part of the Jiucayuan, the nodules coalesce to form petrocalcic beds that are crudely bedding parallel and have diffuse basal and upper contacts. A 30-cm thick petrocalcic layer in a Calcisol in the middle part of the Jiucayuan LC in the Zhaobishan section forms a giant gilgai/pseudo-anticline, with a ~20 m span and ~1 m relief (Fig. 4M). This petrocalcic horizon is interpreted as having developed in a mudflat of an ephemeral lake under a semiarid climate. Vertisols and vertic features are poorly developed and indicate generally weak precipitation and temperature seasonality. However, in some intervals in the central Taodonggou and Zhaobishan sections, the large proportion of fluvial sediments likely reflects a strong precipitation seasonality, under which intensive weathering in the source areas may have occurred. Finally, the subhumid-semiarid conditions during the Jiucayuan time was persistent in all three areas. The magnitude of intracyclic variations at the high-order cycle scale is generally large but variable (Fig. 11).

Vertebrate fossils, especially those of the dicynodont therapsid *Lystrosaurus*, are common and locally abundant in the Jiucayuan LC (Cheng et al., 1996; Metcalfe et al., 2009; Liu and Abdala, 2017; unpublished data). Indeed, the high density of tetrapod fossils in certain horizons in the Jiucayuan is in stark contrast to the mostly barren strata of the other LCs in this study; the LC has produced the highest diversity of tetrapods (e.g., Li et al., 2008; Maisch and Matzke, 2014; Huang et al., 2021). The predominance of *Lystrosaurus* in the Jiucayuan faunal assemblage, as well as the presence of procolophonids, archosauromorphs, temnospondyls, and thecocephalians (Cheng et al., 1996; Lucas, 2001; Huang et al., 2021), makes the assemblage comparable to the fauna known from the *Lystrosaurus declivis* Assemblage Zone of the

South African Karoo Basin (Botha and Smith, 2020; cf. Gastaldo et al., 2021). This similarity also appears to extend to their community structures and ecological dynamics (Roopnarine et al., 2007; Roopnarine et al., 2017; Huang et al., 2021). The frequent occurrence of tetrapod fossils in overbank and lakeplain deposits may indicate that herbivores like *Lystrosaurus* were feeding on riparian vegetation, or may have accumulated in death assemblages near water sources during seasonally dry conditions.

In summary, the Jiuaiyuan LC in the Taodonggou and Dalongkou areas exhibits a similar thickness and similar types of HCs. Sediments were deposited mainly in lakeplain-littoral environments, except where meandering stream environments occurred in central Taodonggou, under stable subhumid-semiarid climatic and tectonic conditions (Fig. 11). The LC in the Zhaobishan section is about four times thicker than those in Taodonggou and Dalongkou, and was deposited in alternating braided stream and lakeplain-sublittoral environments under a subhumid-semiarid condition. The intermediate-order alternation of depositional environments may be related to episodic tectonic uplift and ensuing quiescence, as a result of an upslope location of the Zhaobishan area closer to the North Tianshan suture zone.

### 5.3. Shaofanggou low-order cycle

The age range of the Shaofanggou LC spans from 250.53 to 249.7 Ma, about 0.88 Ma in the early Olenekian (ICS, 2020; cf. Ogg et al., 2020) in the south Taodonggou section (Table 1; Figs. 2, 3). The age (249.7 Ma) of the top of the Shaofanggou LC in south Taodonggou section is estimated using an average sedimentation rate of 92.1 m/Ma. Using this rate, and assuming the base of Shaofanggou LC is synchronous across the region with an age of ~250.53 Ma in all sections, the age of the top of the unit in the central Taodonggou and north Dalongkou sections is estimated to be 249.15 and 249.61 Ma, respectively. This sedimentation rate, however, may not be applicable to the braided stream-dominated deposits in the Zhaobishan section. Thus, the highest rate of 325.6 m/Ma, which is obtained from the lower segment of the age model for fluvial-dominated deposits in the Wutonggou LC in Tarlong, is used to calculate an age of 249.4 Ma for the top of Shaofanggou LC in Zhaobishan. The Shaofanggou LC is 81.5, 127, 84.3, and 365.7 m thick in the south and central Taodonggou, north Dalongkou, and Zhaobishan sections, respectively (Figs. 2, 12). The base of the Shaofanggou LC is marked by a high-relief erosional base of a fluvial channel in all sections, which cuts into underlying lakeplain to sublittoral deposits in the north and south Dalongkou, and Zhaobishan sections (Figs. 8A, B, 9, S3D, S3E, S4D), and thick overbank deposits in the south and central Taodonggou sections (Figs. 7B, C, S2D, S2E). The erosive channel signifies a regional uplift and peneplanation followed by renewed coarse siliciclastic influx and fluvial deposition across the Jiuaiyuan and Shaofanggou LC boundary. The base is interpreted, in general, as an erosional disconformity or diastem with a variable and moderate amount of missing time. This interpretation is based on the overall similarity in lithology and climatic and tectonic conditions between the Jiuaiyuan and Shaofanggou LCs. However, the top of the Shaofanggou LC is a regional unconformity across most of the greater Turpan-Junggar basin (Zhang, 1981; XUARBGMR, 1993; 1999). A thick succession of conglomerates and very coarse sandstones of braided stream systems of the Karamay LC juxtaposes with underlying thick multi-story highly-mature Calcisols of the Shaofanggou LC in the study areas (Figs. 7B, C, 8B, 9, 12, S2D, S2E, S3D, S4D). Significant erosion had occurred as demonstrated by the variable thickness of the Shaofanggou LC and varying estimated ages of its upper boundary in all sections (Figs. 2, 12; e.g., Wartes et al., 2002).

The Shaofanggou LC consists of abundant lakeplain-littoral and braided stream, some meandering stream, and a few deltaic HC deposits (Fig. 13A, D), similar to the Jiuaiyuan LC. Both LCs also have similar colors of dark reddish brown, maroon, grayish red and purple for mudrock-rich intervals, and gray, greenish gray and drab for sandstone and conglomerate intervals (Figs. S1A–C, S2A–C, S3A–C, S4A–C).

Overall, the proportion of conglomerate and sandstone decreases and mudrock increases upward in the LC. The basal part of the LC is composed of fluvial deposits in all sections. These are of braided streams in Zhaobishan and meandering streams in all other sections, where the channel-lag deposits are mainly pebble to cobble conglomerates, except for medium-coarse sandstones in south Dalongkou. These rock types signify a period of uplift and fluvial incision and peneplanation marking the Jiuaiyuan-Shaofanggou boundary, followed by fluvial deposition. In the Taodonggou and Dalongkou areas, the meandering stream HCs form an aggradational interval that is composed of stacked channel fills cutting into each other without overbank deposits and capped by a thick meandering stream HC at the top. The pattern is interpreted to reflect an upward-increasing trend of fluvial accommodation space, as a response to denudation of the catchment basin and increased subsidence. The fluvial deposition was replaced upward by lakeplain-littoral deposition, without a reappearance, in south and central Taodonggou, but fluvial deposition reoccurred in the middle Shaofanggou LC in north Dalongkou. We note that the Shaofanggou LC is incomplete in south Dalongkou due to structural disturbance and poor exposure (Fig. 1E).

In the Zhaobishan area, however, the initial fluvial deposition is more extensive and persistent than that in Taodonggou and Dalongkou, generating 162 m of deposits of 56 braided stream HCs (Figs. 9, 12, S4D). The deposits are gravelly, sandy, or mixed. Clasts in the conglomerates are cobble to pebble in size and, in some cases, boulders, and are dominantly of igneous or sedimentary (Fredericks, 2017). Geological mapping in the Zhaobishan area indicates that this interval of braided stream HCs is widespread and persistent, albeit with variable thickness (Fig. 1E). It is interpreted as an alluvial fan complex. The complex is overlain by a 20 m-thick succession of lakeplain-littoral HCs, which is overlain by 180 m of meandering stream HCs that persist to the top of the Shaofanggou LC (Figs. 9, 12). The meandering stream systems are coarse-grained in the lower part of the interval and gradually change to very thick systems in the upper part. In Zhaobishan, as well as in Taodonggou and Dalongkou, the uppermost part of the Shaofanggou LC is composed mainly of thick mud-rich overbank or lakeplain deposits (Fig. 12), within which mature Calcisols developed (Fig. 4L).

The overall trend of depositional environments is consistent in all three study areas. This trend reflects an initial phase of intense fluvial sedimentation, followed by fluvial and/or lacustrine sedimentation in an increasingly stable and low-topographic gradient setting, and ending with mud-rich deposits and intense pedogenesis on a stable landscape (Fig. 12). Hence, the Shaofanggou LC represents a cycle of catchment-basin evolution from uplift, peneplanation, expansion, and stabilization. The great thickness of fluvial-dominated sediment accumulation in the Zhaobishan area indicates that it was a depocenter and close to the North Tianshan provenance (Fredericks, 2017; Zheng and Yang, 2020).

The small volume of meandering stream and deltaic deposits in the Shaofanggou LC likely indicates that these Triassic lakes were not overfilled. Under-filled lakes were also unlikely because of the absence of evaporites and eolian deposits (Carroll and Bohacs, 1999). Where thick meandering stream and deltaic deposits occur, a lake may tend to be more open, whereas the lake tends to be more closed where stacked highly-mature Calcisols occur. Overall, the Shaofanggou lakes are interpreted to be balance-filled. Tectonism in the source areas marks a trend of initial uplift and subsequent quiescence and denudation, correlating with the evolution of the catchment basin interpreted above. Episodic uplift of source areas and subsidence at the depositional sites, at both the high- and intermediate-order cycle scales, recurred throughout Shaofanggou time, as interpreted using the criteria discussed in previous sections (Fig. 12).

Lithofacies and their interpreted environments, along with the type and occurrence of paleosols, indicate that subhumid-semiarid conditions dominated during deposition of the Shaofanggou LC, similar to that of the Jiuaiyuan LC (Figs. 11, 12). Rare deltaic and meandering stream, and abundant mud-rich shallow lakeplain-littoral HCs, are evidence for limited perennial stream flow and influx of sediment-laden waters into

the lakes (Fig. 13A, D). Intervals of stacked mature Calcisols in the overbank and regressive marginal mud-and-sand flat deposits also are indicative of semiarid conditions. Petrocalcic beds are common in Calcisol Bk horizons, 5–30 cm thick, and composed of coalesced calcitic nodules of various shapes and sizes. These highly-mature Calcisols may have been formed under a semiarid to arid setting. Such a set of conditions was also interpreted by Thomas et al. (2011) based on Gypsisols in the Shaofanggou LC in central Taodonggou (see also Table 2 of Yang et al., 2010). In some cases, common boulders of maroon to red reworked Calcisol clasts occur in braided stream conglomerates and sandstones in the lower Zhaobishan section. These intraformational clasts indicate the development of mature Calcisols in nearby overbank areas, and are used to infer a subhumid-semiarid condition during the braided stream deposition (Fig. 4E).

Evidence for subhumid conditions includes the occurrence of some thick meandering stream and deltaic deposits, which indicate the presence of perennial streams laden with sediment that discharged into the lakes. Permineralized wood preserved in the lower part of the Zhaobishan section is restricted to braided stream deposits of an alluvial fan complex and probably was transported from outside of the depositional site. These woods display distinct growth rings, which indicate growth under a strong precipitation and/or temperature seasonality in an upland forest on a hill slope where climate was humid to subhumid and oscillation of snow lines occurred (Wan et al., 2019a; the wood of *Amyelon bogdense* was reported from Induan deposits, which have been revised to a lower Olenekian age based on results of the current study). This condition contrasts with that at the depositional site where mature Calcisols formed. The pattern mimics the Highland (Type H) climate found, today, in mountainous regions. Furthermore, well-preserved leaf matter in a thin siltstone bed in the same horizon is evidence for the presence of riparian vegetation, which is substantiated by the common occurrence of rhizoconcretions and root molds throughout the Shaofanggou LC. This vegetation likely was the base of the food chain for the fossil-vertebrate assemblage preserved in the Shaofanggou LC (represented by fragmentary materials likely referable to *Lystrosaurus* and a temnospondyl amphibian; Cheng et al., 1996; Fig. 12). Finally, the occurrence of thick, multi-story Calcisols in the uppermost part of the LC is remarkably persistent. This interval ranges from 20 to 40 m in thickness and contains one to three horizons of abundant rhizoconcretions hosted in marginal mudflat or overbank deposits (Figs. 4L, 12). Some rhizoconcretions, up to 30 cm thick and 3 m in length, are in a vertical to subvertical orientation, and both taper and branch downward in the paleosol. These rooting structures are truncated by transgressive surfaces or erosional channel bases (Figs. 7B, C, 8B, 9, S2D, E, S3D, S4D). No permineralized wood has been found here, to date. This interval signifies a regional highly-stable landscape, where riparian vegetation was well developed and growing under subhumid-arid (seasonally dry) conditions. The paleoecological significance awaits future exploration.

In summary, the Shaofanggou LC shows the same trend of drainage-basin evolution in all three areas, Tarlong-Taodonggou and Dalongkou in the basin and Zhaobishan in the foothills. The areas experienced uplift and peneplanation before fluvial deposition took place, and became increasingly stabilized and achieved a great landscape stability at the end. Sediment accumulation occurred slowly mainly in the lakeplain-littoral and meandering stream environments at the basinal sites. In contrast, thick accumulation occurred rapidly in braided stream-dominated alluvial fan and meandering stream environments in the upslope Zhaobishan depocenter, where the stratigraphic thickness is three to four times that of basinal sections. Climate conditions ranged from subhumid to semiarid and, in some periods, to arid; these persisted throughout the Shaofanggou time. Despite the relatively dry conditions, riparian and upland vegetation, albeit poorly preserved, probably flourished and served as food for terrestrial herbivores, including vertebrates, such as *Lystrosaurus*.

## 6. Late Permian-Early Triassic paleoenvironmental, paleoclimatic, and paleotectonic trends in the Bogda Mountains

The upper Wuchiapingian-mid Induan Wutonggou, mid Induan-lower Olenekian Jiucaiyuan, and lower-mid Olenekian Shaofanggou LCs in the Tarlong-Taodonggou, Dalongkou, and Zhaobishan areas record the history of environmental, climatic, and tectonic evolution in the Bogda Mountains. The three study areas cover about 10,000 km<sup>2</sup>. Reconnaissance and literature review in areas of Kulai (~300 km east of Zhaobishan), the western Bogda Mountains (~100 km northwest of Tarlong-Taodonggou), and Aiweiergou (~100 km southwest of Tarlong-Taodonggou) indicate a similar stratigraphy in these areas (Zhang, 1981; Yang et al., 1986; XJUARBGM, 1993; 1999; Allen et al., 1995; Carroll et al., 1995; Wartes et al., 2002; Greene et al., 2005; Metcalfe et al., 2009). In total, rocks in these localities cover ~100,000 km<sup>2</sup> in the southeastern part of the greater Turpan-Junggar basin. The general evolutionary history interpreted for the three study areas may potentially be extrapolated to this part of the basin.

The upper Permian-Lower Triassic strata were deposited in braided and meandering stream, and lacustrine deltaic and sublittoral to lakeplain environments in grabens and half grabens and, thus, exhibit a three-order spatial and temporal variability in lithofacies, depositional systems, and stratigraphic thickness at the 1–100 m scale (Figs. 10–12). Upper Wuchiapingian to mid-Induan sediments of the Wutonggou LC were deposited mainly in meandering stream, lacustrine delta, and lakeplain to sublittoral environments (Fig. 13A, B). The base of the LC is a conformable regional transgressive surface where lacustrine sediments overlie loessial and fluvial deposits of the upper Quanzijie LC in the Tarlong-Taodonggou and Dalongkou areas (Obrist-Farner and Yang, 2016). The Quanzijie sediments in Zhaobishan are currently interpreted as proglacial lacustrine and braided stream deposits (unpublished data). The Tarlong and Zhaobishan areas acted as depocenters along the axis of half grabens, whereas the Taodonggou and Dalongkou areas are located on the ramp margin. The dramatic thickness difference between the Tarlong and Taodonggou sections demonstrates the great intra-graben stratigraphic variability (Fig. 10). Sedimentation occurred in perennial streams and open over-filled lakes under a generally humid-subhumid climate. The climate became more variable and gradually trended toward a subhumid-semiarid condition sometime after the PTB in the early Induan (see also Cui and Cao, 2021 for interpretations using geochemical evidence). Nevertheless, higher plants flourished into the latest Wutonggou time, sometime around the early-mid Induan (Wan et al., 2019a, 2019d).

A regional uplift and fluvial peneplanation event affected many localities during the mid Induan, marking the end of Wutonggou deposition and the complete transition to a subhumid-semiarid seasonally-dry climate. This event formed a diastem and terminated deltaic deposition in some areas, whereas it had minimal impact in other areas where shallow lacustrine sedimentation continued uninterrupted. Fluvial and lakeplain-littoral sedimentation persisted from the mid Induan into the early Olenekian, forming the Jiucaiyuan LC (Figs. 11, 13A, C). Fluvial deposits dominate in the lower part of the LC and lacustrine deposits in shallow balance-filled lakes in the middle and upper parts of the LC. Calcisols and other calcareous paleosols were well developed in overbank and lakeplain sediments under a relatively dry subhumid-semiarid climate. Riparian vegetation continued to be present, supporting a large vertebrate population (Wan et al., 2021a; Metcalfe et al., 2009; Liu and Abdala, 2017; Huang et al., 2021). Intra-graben stratigraphic variability occurs between the meandering stream-dominated central Taodonggou and lacustrine sediment-dominated south Taodonggou areas. Inter-graben variability occurs between the Zhaobishan area in the upslope and the Taodonggou and Dalongkou areas in the interior of the greater Turpan-Junggar basin. In Zhaobishan, 12 alternating braided stream and sublittoral-lakeplain successions accumulated in the Jiucaiyuan LC, which is four times thicker than those in the Taodonggou and Dalongkou areas. This indicates that the Zhaobishan area at the

upslope peripheral location of the greater Turpan-Junggar basin was more tectonically active. The Jiucaiyan LC records a cycle of tectonic uplift and quiescence and expansion and stabilization of the drainage basin.

Another regional uplift and peneplanation event at the end of Jiucaiyan time, in the early Olenekian, terminated Jiucaiyan deposition. This event was likely more extensive and prolonged than that marking the beginning of the Jiucaiyan LC and terminated sediment deposition. It resulted in the formation of a regional disconformity or diastem across the entire area. Subsidence followed by fluvial and lacustrine sedimentation occurred after peneplanation wherein the lower–mid Olenekian Shaofanggou LC was deposited. Coarse-grained braided and meandering stream deposition in the basal and lower parts was replaced by fine-grained meandering stream and shallow lacustrine deposition in balanced-fill lakes (Figs. 12, 13A, D). Highly mature, multistory Calcisol-s and rare Gypsisols formed under subhumid-semiarid and, occasionally, arid conditions. Riparian vegetation was present; an upland forest may have existed near Zhaobishan (Wan et al., 2019c); and this vegetation supported a vertebrate population, although the latter is poorly represented in the fossil record. The evolution of this catchment basin culminated at the end of Shaofanggou time wherein a highly stable landscape was established. This is evidenced by the presence of vegetation with extensive root systems preserved across the entire study area. Moderate intra-graben stratigraphic variability of varying depositional systems is present in the Taodonggou area, and likely controlled by the geographic position of the site and its proximity to the lake on the ramp margin. Inter-graben stratigraphic variability between the Zhaobishan and the Taodonggou and Dalongkou areas is as discordant as that in the Jiucaiyan LC. The Zhaobishan area remained as a major depocenter where an alluvial fan complex in the lower part and meandering stream systems in the upper part developed. Shaofanggou deposition ended in response to a major uplift and peneplanation event that formed a regional unconformity, which probably represents more than two million years of missing time (Fig. 2). This was followed by the deposition of the Middle Triassic Karamay LC, starting another cycle of catchment evolution. In contrast to both the Jiucaiyan and Shaofanggou LCs, deposition of the Karamay LC took place under a humid–subhumid climate, as indicated by abundant permineralized wood assemblages in copious braided stream deposits (Fig. S3D).

## 7. Discussion

### 7.1. The relationship between litho-, cyclo-, and chronostratigraphies – implications for stratigraphic variability and resolution

Lithology is not a very reliable attribute to be used for stratigraphic correlation of terrestrial records, because sedimentary environments change rapidly on and across the land surface. As a result, several types of sediments/facies commonly are deposited in proximity to one another and have varying thicknesses in the same or adjacent environments. In addition, contemporaneous and pene-contemporaneous sediment erosion is also frequent. Thus, lateral facies and thickness changes commonly are rapid in terrestrial deposits. It is uncommon that a specific lithology in a type section is persistent for a long distance. For example, the Guodikeng Formation in the upper part of Wutonggou LC in the study area (Fig. 2), which possibly contains the PTB (e.g., Yang et al., 1986; Liao et al., 1987; Li et al., 2003; Cao et al., 2008; Metcalfe et al., 2009; Chu et al., 2015; Cui and Cao, 2021; and references therein) and many well-preserved vertebrate fossils (e.g., Cheng, 1986; Lucas, 2001; Liu and Abdala, 2017; Huang et al., 2021), is defined basically by its mixed coloration of gray and yellow and the predominance of fine-grained lithology (XUARBGMR, 1999). The type location of the Guodikeng Formation was unofficially discarded and replaced by the south Dalongkou section (Yang et al., 1986), which is substantially modified by several faults and folds (Fig. S3A–C). Yang et al. (1986) used the top of a prominent sandstone, interpreted as an amalgamated interval of

fluvial channel fills in the current study, as the base of the formation and a color change at its top to define the formation in the south Dalongkou section (Figs. 10, S3D). Yang et al. (1986; see also Chu et al., 2015) also measured the formation in north Dalongkou, ~1.5 km to the north, and found that the rock types and their thickness change significantly. To avoid lithostratigraphic miscorrelation, other lithology-independent attributes may be used. The caveat to this approach is that lithology is the carrier of most, if not all, of the physical and chemical attributes.

An alternative approach is to use interpretive attributes, such as trends of depositional environments, climatic and tectonic conditions, and individual geologic events, as correlation markers (Shanley and McCabe, 1994). Such an approach is used in the cyclostratigraphic correlation in this study (Fig. 5). The compositional, sedimentary textural and structural, and stratal geometric characteristics of individual lithofacies, as well as their vertical and lateral relationships, are used here to interpret depositional environments and their systematic changes. These changes, then, are used to define sedimentary cycles and interpret climatic and tectonic processes that have significantly controlled those environmental changes. Hence, the temporal and spatial trends of the cycles and controlling processes are used for stratigraphic correlation (Fig. 5). However, there are two major problems associated with this approach. First, the interpretation of any depositional environment and its controlling processes is not unique, and is dependent on data availability and the knowledge base of the interpreter and his/her understanding of related fields. Second, the effectiveness of this approach depends on the areal extent over which the controlling processes have operated. Autogenic processes of a local extent and short duration are “erratic” and may not be as effective as allogenic processes of a regional extent and great duration (Beerbower, 1964; Yang et al., 1998). It is beyond doubt that both approaches require a solid lithostratigraphy as the foundation for the extraction and interpretation of attributes. We endeavor to provide such a foundation, that is, a cyclostratigraphic framework for the upper Permian–Lower Triassic terrestrial deposits in the Bogda Mountains, as the basis for future studies (Supplemental Materials).

We also have tried to correlate two distinct climatic proxies (events) across the region to subdivide the Wutonggou LC. The first is the Calcisol zone and the second is the last major coal bed in Tarlong area (Fig. 10). The radiometric ages of the bentonites above the Calcisol zone provide evidence that this interval was synchronous between the north and south Tarlong sections; and similarly, physical tracing establishes the synchronicity of the coal bed. However, the correlation of the coal bed with the one at the base of the south Taodonggou section ~4 km away is only supported by indirect evidence, which includes the consistency in bed thickness, lithology, and relative stratigraphic position, and the consistency of the age models that utilize the coal bed as the correlation marker. One may simply argue against using the bed consistency due to the absence of such a thick coal bed in the central Taodonggou section, which is ~2 km away. However, the absence can be explained by the paleogeographic location of the central Taodonggou section on the ramp margin of the Tarlong-Taodonggou half-graben, where only an interval of thin lignite and carbonaceous shale was deposited. If this explanation is reasonable, the correlation is useful. The extension of the correlation of the coal bed and the Calcisol zone to Dalongkou and Zhaobishan is tentative. The rationale for this “long-distance” correlation is that the correlation is not based on lithology, but two interpreted regional events. The first event is a significant short-term climatic perturbation to a drier condition as represented by the Calcisol or calcareous Argillisol and Protosol zone; and the second event a perturbation to a wetter condition as represented by the coal or lignite and carbonaceous shale. The two events are correlatable even though these conditions did not result in the deposition of the same lithologies in all sections.

The other example of an uncertainty in our stratigraphic correlation is the placement of the top of Wutonggou LC in the south Tarlong section (Figs. 2, 6C, S1F). The top of the unit demarcates the transition from a

variably humid-subhumid condition in the uppermost Wutonggou LC to a full-scale subhumid-semiarid seasonally-dry condition in the Jiuciyuan LC. In several sections, not including those in south Tarlong and south Dalongkou, this transition is also accompanied by an event of uplift and peneplanation as indicated by fluvial channel erosion and deposition (Figs. 10, 11). However, the calibration of this event based on the age model places the top of the Wutonggou LC at 251.79 Ma in south Tarlong and 251.36 Ma in south Taodonggou with a discrepancy of 0.43 Ma. The top of the Wutonggou LC in south Taodonggou is preferred because of the stratigraphic continuity, quality and amount of exposure, and minimal structural disturbance of the area when compared to south Tarlong. The placement of the upper boundary of the Wutonggou LC in south Tarlong is likely too low. Nevertheless, the fact that its placement in the south Tarlong area was regarded as viable by Yang et al. (2010) exemplifies the importance of a solid lithostratigraphy and data availability in cyclostratigraphic studies and intra- and inter-graben correlation in rift basin settings.

The aforementioned examples of stratigraphic correlation demonstrate the critical role of high-resolution numerical age information in constraining and converting cyclostratigraphy into chronostratigraphy. Building on the work of Yang et al. (2010), the age models established in the current study make a significant stride toward a viable terrestrial upper Permian-Lower Triassic chronostratigraphy in the Bogda region, and shall be improved upon with further age dates. An important derivative of our age models is the estimation of sedimentation rate. The average sedimentation rates of different stratigraphic intervals are used to project chronostratigraphic boundaries onto measured sections and estimate ages of boundaries of LCs (Table 1; Figs. 2, 3). Moreover, they provide extra insights into the stratigraphic resolution and controlling processes of a sedimentary record. The median age line of our age model (Fig. 3) delimits two segments of different sedimentation rates. The lower segment for the Wuchiapingian and Changhsingian deposits of the Wutonggou LC has a high sedimentation rate of  $\sim 350$  m/Ma, whereas the upper segment for the Induan and Olenekian deposits has a much lower rate of  $\sim 90$  m/Ma. The two segments join to form a gradual

transition in sedimentation rate decrease around the PTB. The pattern crudely correlates with the sedimentary, climatic, and tectonic trends of the Wutonggou, Jiuciyuan, and Shaofanggou LCs in the Tarlong-Taodonggou and Dalongkou areas. That is, sediment accumulation in fluvial and lacustrine environments under a humid-subhumid climate in a rapidly subsiding area is much faster than that under a subhumid-semiarid climate in a peneplaned, relatively stable area on the ramp margin. The former would result in a record with a much higher stratigraphic resolution per unit time than the latter.

However, the above pattern apparently does not apply to the Zhaobishan record. The Jiuciyuan and Shaofanggou LCs in the Zhaobishan record are much thicker and likely have a much greater average sedimentation rate than their equivalents in the Taodonggou and Dalongkou records (Figs. 2, 10, 11, 12). As noted above, the Zhaobishan section records the same Wuchiapingian-Olenekian climate trend as all other sections. Hence, it is the tectonic and paleogeographic settings of the Zhaobishan area that is responsible for the difference. Finally, average sedimentation rates are time-dependent (e.g., Sadler, 1999; Yang et al., 2004, and references therein). However, variable sedimentation rates estimated over the same order of duration would reflect variations in sedimentary environments and controlling processes. For example, assuming that our correlation of the Calcisol zone and coal bed in the Wutonggou LC among the three areas is valid (Fig. 10), the two markers can be regarded as timelines. Together with the base and top of the Wutonggou LC and the projected Wuchiapingian-Changhsingian and PTB, the Wutonggou LC is subdivided into five time-equivalent intervals (Fig. 10). The thickness differences of each interval between the sections indicate significant variation in sedimentation rates and stratigraphic resolution at the intra- and inter-graben scales. It becomes apparent that the depocenter was located in the Tarlong area before the formation of the Calcisol zone, but migrated to the Zhaobishan area afterward. The stratigraphic variability is well demonstrated within a cyclostratigraphic framework constrained by the age model. Consequently, any geochemical and paleontologic signals in the five intervals would have variable spatial and temporal stratigraphic resolutions.

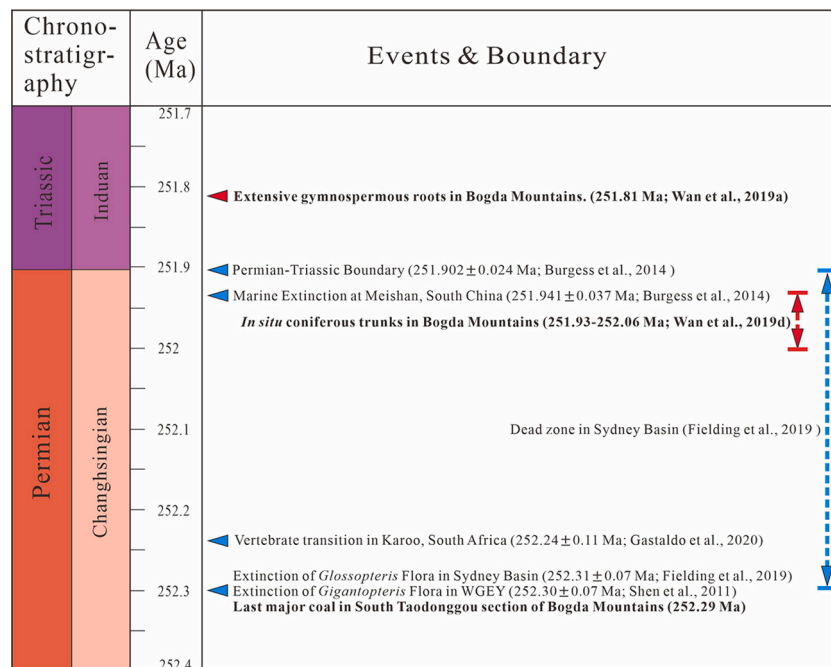


**Fig. 14.** Chart showing the timing of reported events of vascular plant evolution in Australia, south China, and the Bogda Mountains, NW China, during the Changhsingian and Induan. The transition from the *Dapocephalus* to *Lystrosaurus* assemblage zones as currently defined in South Africa (but see Gastaldo et al., 2021) is also marked. WGEY = western Guizhou and eastern Yuan provinces in southwestern China. See text for discussion.

## 7.2. Current understanding of plant evolution within the improved chronostratigraphic framework

The improved chronostratigraphy provides age controls for the fossil plant assemblages, especially permineralized wood, in the upper Permian–Lower Triassic strata in the study area. Hence, an accurate history of vascular plant trends in the Bogda Mountains can be delineated and correlated with other marine and non-marine records in the world (Schneider et al., 2020). At the present, knowledge on the evolutionary history of latest Permian and Early Triassic plants is still limited; and the correlations between marine and non-marine records are coarse (Feng et al., 2018; Wan et al., 2019a, 2019b, 2019c, 2019d). As a result, questions remain on whether vascular plants experienced a mass extinction at the end of Permian (Retallack, 1995; Looy et al., 2001; Gastaldo et al., 2009; Cascales-Miñana and Cleal, 2014; Schneebeli-Hermann et al., 2017; Gastaldo, 2019; Nowak et al., 2019; Feng et al., 2020). And, if true, the question then is whether the floral extinction was synchronous with that of marine invertebrates and terrestrial vertebrates (e.g., Maxwell, 1992; Wagner et al., 2006; Shen et al., 2011, 2019; Stanley, 2016; Zhang et al., 2016; Fielding et al., 2019; Gastaldo et al., 2020b, 2021; Viglietti et al., 2021).

The evolution of plant communities in the latest Permian and early Induan in the Bogda Mountains differs from those evolutionary trends in Gondwana (Fig. 14). The estimated age of the last major coal in the south Taodonggou section is 252.29 Ma (Figs. 2, 3, 10) and compatible to the ages of 252.30 and 252.31 Ma of the last coals in South China and Australia, respectively (Shen et al., 2011; Fielding et al., 2019). Coincidentally, our inferred age of the youngest major coal is also similar to the age (252.24 Ma) of the transition from the *Daptocephalus* to *Lystrosaurus* assemblage zones in South Africa (Gastaldo et al., 2020a, 2020b) as currently defined (Gastaldo et al., 2021; cf. Botha et al., 2020). Extensive evidence shows that the collapse of the austral Permian *Glossopteris* flora coincides with the cessation of the last coal in the Sydney Basin (e.g., Fielding et al., 2019). The extinction of the *Gigantopteris* flora in South China occurred at a variable thickness above the last coal at the top of Xuanwei Formation at different localities (Shen et al., 2011; Zhang et al., 2016). Hence, the question remains as to whether the extinction of the *Gigantopteris* flora in South China (Zhang et al., 2016), which is interpreted as a quick turnover from the rainforest with *Gigantopteris* to an herb land-like ecosystem (Feng et al., 2020), also is coeval. However, the plant communities in the Bogda Mountains continued to flourish after the occurrence of the last coal. For example, both thin lignite and carbonaceous shale are present at 16–19 m above the last major coal, and two intervals yield in-situ fossil trunks at ~69 m in the south Taodonggou section (Figs. 14, S2E; Wan et al., 2019b). The upright and oblique trunks with root systems extending into the underlying paleosols demonstrate that they were buried in life position. They represent a lake margin vegetation community dominated by conifers with *Protophyllocladoxylon*-type wood. Furthermore, anatomical features of the fossil trunks from south Taodonggou indicate that the diversity of conifers during the Changhsingian is underestimated if only based on plant impressions (Wan et al., 2021b). Some dispersed branches and stems that are preserved parallel to bedding are probably from plants growing on the lake margin or upstream riparian niches. The plants represent the latest Permian vegetation from the Bogda Mountains with an estimated age of 251.95 Ma (Fig. 14). From the perspective of fossil wood anatomy, the composition and diversity of the branches, stems, and trunks are consistent with those from the Wuchiapingian deposits in the Tarlong-Taodonggou area. Hence, the Bogda plant communities were not affected by the event that resulted in the extinction of the *Glossopteris* flora in the Sydney Basin and *Gigantopteris* flora in South China. Recent evidence from South Africa indicates that taxa of the *Daptocephalus* and *Lystrosaurus declivis* assemblage zones coexisted in *Glossopteris* landscapes (Gastaldo et al. 2021).

In addition, the evolution of plants in the Early Triassic can be deciphered by plant fossils, albeit rarely preserved in the rocks of the

Bogda Mountains. Wan et al. (2019a) reported Changhsingian to Induan (?) silicified gymnospermous roots (*Amyelon bogdense*) from a layer of tuffaceous sandstone in the uppermost Wutonggou LC in the south Taodonggou section. In the newly-calibrated chronostratigraphy, the fossil root interval is 3 m above the PTB and the age of the roots placed at 251.81 Ma in the early Induan according to the age model (Fig. 14). In addition, calamitalean axes and silicified coniferous *Agathoxylon*-type and *Protophyllocladoxylon*-type woody fragments, but no trunks, are preserved in the same interval (unpublished data). Growth rings are absent in all the woody fragments, indicating stable environmental and climatic conditions. No distinctive changes in fossil wood diversity have been identified across the PTB in the study area. Higher in the stratigraphy, fossil charcoal and silicified woody fragments occur in the Olenekian in the north Dalongkou and Zhaobishan sections, respectively (Wan et al., 2019c; Wan et al., 2020, 2021a). The presence of distinct growth rings indicates a highly seasonal climate. In addition, well-preserved wood with anatomical structures in braided stream deposits in the Zhaobishan section indicate that these trees had grown in the riparian area in the upland (also see “Shaofanggou Low-Order Cycle”). Finally, an herbaceous lycopsid (*Annalepis*) and the probable fern *Pecopteris* are preserved in lacustrine deposits in the north Dalongkou section, expanding the diversity of fossil-plant collections. The taxonomy and paleoecological implications of those fossil materials will be reported in future publications.

Our current data indicate that the floral turnover from the Wuchiapingian peltaspermalean-dominated assemblage (Zhou and Zhou, 1986) to the Olenekian *Annalepis* assemblage in Bogda Mountains is distinctive. However, the occurrence of permineralized wood in each unit over this time interval indicates that arborescent trees were persistent on the landscape in NE Pangea. To date, we have no evidence of deforestation around the PTB in the study area. Instead, a plant community with an arborescent coniferous canopy persisted from the Changhsingian into the early–mid Induan. A floral turnover in the Bogda Mountains occurred in the mid Induan and, thus, postdates those reported in South China, Australia, and South Africa. This suggests a diachronous floral turnover on Pangea during the latest Permian to Early Triassic.

## 8. Conclusions

1. An age model was constructed using high-resolution U-Pb zircon CA-TIMS dates for the upper Permian–Lower Triassic fluvial-lacustrine sedimentary record in the Tarlong-Taodonggou sections in the Bogda Mountains in the greater Turpan-Junggar intracontinental rift basin, NW China. The age model is projected to the sections in Dalongkou and Zhaobishan, expanding our understanding of conditions at the paleo-mid-latitude of NE Pangea. Detailed litho- and cyclo-stratigraphy of the three areas is converted to an upper Wuchiapingian–mid Olenekian chronostratigraphic framework, within which paleoenvironmental, paleoclimatic, paleotectonic, and biotic evolution are interpreted.
2. Fluvial-lacustrine sediments comprise three low-order sedimentary cycles (LCs) demarcated by conformity, diastem, and a regional unconformity. The upper Wuchiapingian–mid Induan Wutonggou LC was deposited under a humid–subhumid condition during the late Wuchiapingian that extended into the mid Induan, when climate became drier and more variable in the early Induan. Both the mid-Induan–lower Olenekian Jiuaiyuan and the lower Olenekian Shaofanggou LCs were deposited under subhumid–semiarid seasonally-dry conditions. Short-term arid conditions may have been present during the early Olenekian. Overall, a gradual transition from humid–subhumid to subhumid–semiarid conditions occurred beginning in the latest Changhsingian into the early Induan.
3. Significant intra- and inter-graben spatial and temporal stratigraphic variability in the upper Permian–Lower Triassic strata is indicated by differences in sediment thickness, depositional systems, and average sedimentation rate among the three areas. These factors influenced

the stratigraphic resolution of the sedimentary records in each area. Stratigraphic resolution is controlled by paleogeographic location, shifts in depocenters, and variable uplift and subsidence in different parts of the catchment basin over time.

4. Lush vegetation was present from the late Wuchiapingian to the early Induan, across the Permo-Triassic boundary. Riparian vegetation and upland forests were present from the mid Induan to the early Olenekian, and served as the primary productivity for the terrestrial ecosystems, including vertebrates, such as *Lystrsaurus*. However, an apparent floral changeover in vascular plants occurred in the early Induan and postdates the marine mass extinction at Meishan, south China. The correlation of the latest Changhsingian–early Induan record of plant communities in the Bogda Mountains with those in Australia, South Africa, and south China suggests that floral changeover is diachronous across the supercontinent Pangea.

Supplementary data to this article can be found online at <https://doi.org/10.1016/j.earscirev.2021.103741>.

#### Declaration of Competing Interest

The authors declare that they have no known competing financial interests or personal relationships that could have appeared to influence the work reported in this paper.

### Appendix A. Data, methodology, and results of geochronological descriptions

#### A.1. LA-ICPMS Methods

Zircon grains were separated from rocks using standard techniques, annealed at 900 °C for 60 h in a muffle furnace, and mounted in epoxy and polished until their centers were exposed. Cathodoluminescence (CL) images were obtained with a JEOL JSM-300 scanning electron microscope and Gatan MiniCL. Zircon was analyzed by laser ablation inductively coupled plasma mass spectrometry (LA-ICPMS) using a ThermoElectron X-Series II quadrupole ICPMS and New Wave Research UP-213 Nd:YAG UV (213 nm) laser ablation system. In-house analytical protocols, standard materials, and data reduction software were used for acquisition and calibration of U-Pb dates and a suite of high field strength elements (HFSE) and rare earth elements (REE). Zircon was ablated with a laser spot of 25 μm wide using fluence and pulse rates of 5 J/cm<sup>2</sup> and 5 Hz, respectively, during a 45 s analysis (15 s gas blank, 30 s ablation) that excavated a pit ~15 μm deep. Ablated material was carried by a 1.2 L/min He gas stream to the nebulizer flow of the plasma. Dwell times were 5 ms for Si and Zr, 200 ms for <sup>49</sup>Ti and <sup>207</sup>Pb, 80 ms for <sup>206</sup>Pb, 40 ms for <sup>202</sup>Hg, <sup>204</sup>Pb, <sup>208</sup>Pb, <sup>232</sup>Th, and <sup>238</sup>U and 10 ms for all other HFSE and REE. Background count rates for each analyte were obtained prior to each spot analysis and subtracted from the raw count rate for each analyte. Ablation pits that appear to have intersected glass or mineral inclusions were identified based on Ti and P. U-Pb dates from these analyses are considered valid if the U-Pb ratios appear to have been unaffected by the inclusions. Analyses that appear contaminated by common Pb were rejected based on mass 204 being above baseline. For concentration calculations, background-subtracted count rates for each analyte were internally normalized to <sup>29</sup>Si and calibrated with respect to NIST SRM-610 and -612 glasses as the primary standards. Temperature was calculated from the Ti-in-zircon thermometer (Watson et al., 2006). Because there are no constraints on the activity of TiO<sub>2</sub>, an average value in crustal rocks of 0.8 was used.

Data were collected in seven experiments in December 2014, January 2019, December 2019, and February 2020. For U-Pb and <sup>207</sup>Pb/<sup>206</sup>Pb dates, instrumental fractionation of the background-subtracted ratios was corrected and dates were calibrated with respect to interspersed measurements of zircon standards and reference materials. The primary standard Plešovice zircon (Sláma et al., 2008) was used to monitor time-dependent instrumental fractionation based on two analyses for every 10 analyses of unknown zircon. A secondary correction to the <sup>206</sup>Pb/<sup>238</sup>U dates was made based on results from the zircon standards Seiland (530 Ma, unpublished data, Boise State University) and Zirconia (327 Ma, unpublished data, Boise State University), which were treated as unknowns and measured once for every 10 analyses of unknown zircon. These results showed a linear age bias of several percent that is related to the <sup>206</sup>Pb count rate. The secondary correction is thought to mitigate matrix-dependent variations due to contrasting compositions and ablation characteristics between the Plešovice zircon and other standards (and unknowns).

Radiogenic isotope ratio and age error propagation for all analyses includes uncertainty contributions from counting statistics and background subtraction. The standard calibration uncertainty for U/Pb is the local standard deviation of the polynomial fit to the fractionation factor of Plešovice versus time and for <sup>207</sup>Pb/<sup>206</sup>Pb is the standard error of the mean of the fractionation factor of Plešovice. These uncertainties are 0.5–1.0% (2σ) for <sup>206</sup>Pb/<sup>238</sup>U and 0.3–0.8% (2σ) for <sup>207</sup>Pb/<sup>206</sup>Pb. Errors without standard calibration uncertainty are shown in Table A1 in Supplemental Materials and given below. Age interpretations are based on <sup>206</sup>Pb/<sup>238</sup>U dates. Errors are 2σ.

#### A.2. CA-TIMS Methods

U-Pb dates were obtained by the chemical abrasion isotope dilution thermal ionization mass spectrometry (CA-TIMS) method from analyses composed of single zircon grains (Table A1 in Supplemental Materials), modified after Mattinson (2005). Zircon was separated from rocks using standard techniques, placed in a muffle furnace at 900 °C for 60 h in quartz beakers, mounted in epoxy, and polished until the centers of the grains were exposed. Cathodoluminescence (CL) images were obtained with a JEOL JSM-300 scanning electron microscope and Gatan MiniCL. Zircon was

### Acknowledgements

Dr. Robin Trayler conducted the majority of the Bayesian age modeling and also provided model codes. We thank Drs. Q. Feng, Y.Q. Liu, J. Liu, and J.Y. Lin for collaborations, and Dr. D. Wang, M. Runnion, W. Guan, Dr. B. Jeffrey, Dr. S. Thomas, Dr. T. Meyers, Dr. Y. Yang, Dr. J. Obrist-Farner, T. Foster, Dr. Z.X. Li, Dr. B. Sun, X.W. Peng, J. Fredericks, J. Duan, Y.R. Lu, Dr. X. Zhan, Dr. D.Y. Zheng, S.X. Wu, W.T. Zhang, Z.Y. Ju, and many other students from Northwestern University, China, Shandong University of Science and Technology, and China University of Petroleum (eastern China) for assistance during field expeditions since 2004. We also thank S.W. Mei and J.J. Li for logistic support. The project was partially supported by U.S. NSF grants (EAR 1714749 to WY, EAR 1714863 to JLC, EAR 171475 to RAG, EAR 1714797 to NT, EAR 1714928 to JWG, EAR 1714829 to KDA, EAR 1713787 to CAS, and EAR 1714898 to PDR), the National Natural Science Foundation of China (41872013) and Youth Innovation Promotion Association CAS (2020312) to MW, and Strategic Priority Research Program (B) of the Chinese Academy of Sciences (XDB18000000, XDB26000000) to JW. Acknowledgment is made to the Donors of the American Chemical Society Petroleum Research Fund for partial support of this research by WY. We thank Dr. Z.Q. Chen and an anonymous reviewer for constructive reviews and Drs. J.T. Chen and F.F. Zhang, guest editors of the special issue, and A. Negri (ESR editor) for their patience and effort.

removed from the epoxy mounts for dating based on CL images and LA-ICPMS data.

Zircon was put into 3 ml Teflon PFA beakers and loaded into 300  $\mu$ l Teflon PFA microcapsules. Fifteen microcapsules were placed in a large-capacity Parr vessel and the zircon partially dissolved in 120  $\mu$ l of 29 M HF for 12 h at 190 °C. Zircon was returned to 3 ml Teflon PFA beakers, HF was removed, and zircon was immersed in 3.5 M HNO<sub>3</sub>, ultrasonically cleaned for an hour, and fluxed on a hotplate at 80 °C for an hour. The HNO<sub>3</sub> was removed and zircon was rinsed twice in ultrapure H<sub>2</sub>O before being reloaded into the 300  $\mu$ l Teflon PFA microcapsules (rinsed and fluxed in 6 M HCl during sonication and washing of the zircon) and spiked with the EARTHTIME mixed <sup>233</sup>U-<sup>235</sup>U-<sup>205</sup>Pb tracer solution (ET535) or EARTHTIME mixed <sup>233</sup>U-<sup>235</sup>U-<sup>202</sup>Pb-<sup>205</sup>Pb tracer solution (ET2535). Zircon was dissolved in Parr vessels in 120  $\mu$ l of 29 M HF with a trace of 3.5 M HNO<sub>3</sub> at 220 °C for 48 h, dried to fluorides, and re-dissolved in 6 M HCl at 180 °C overnight. U and Pb were separated from the zircon matrix using an HCl-based anion-exchange chromatographic procedure (Krogh, 1973), eluted together and dried with 2  $\mu$ l of 0.05 N H<sub>3</sub>PO<sub>4</sub>.

Pb and U were loaded on a single outgassed Re filament in 5  $\mu$ l of a silica-gel/phosphoric acid mixture (Gerstenberger and Haase, 1997), and U and Pb isotopic measurements made on a GV Isoprobe-T multicollector thermal ionization mass spectrometer equipped with an ion-counting Daly detector. Pb isotopes were measured by peak-jumping all isotopes on the Daly detector for 100 to 160 cycles. Analyses spiked with ET535 tracer solution were corrected for 0.16 ± 0.03%/a.m.u. (1 $\sigma$ ) mass fractionation and analyses spiked with ET2535 tracer solution were corrected for mass fractionation using the known <sup>202</sup>Pb/<sup>205</sup>Pb ratio of the tracer solution. Transitory isobaric interferences due to high-molecular weight organics, particularly on <sup>204</sup>Pb and <sup>207</sup>Pb, disappeared within approximately 60 cycles, while ionization efficiency averaged 10<sup>4</sup> cps/pg of each Pb isotope. Linearity (to  $\geq 1.4 \times 10^6$  cps) and the associated deadtime correction of the Daly detector were monitored by repeated analyses of NBS982, and have been constant since installation. Uranium was analyzed as UO<sub>2</sub><sup>+</sup> ions in static Faraday mode on 10<sup>12</sup>  $\Omega$  resistors for 300 cycles, and corrected for isobaric interference of <sup>233</sup>U-<sup>18</sup>O-<sup>16</sup>O on <sup>235</sup>U-<sup>16</sup>O-<sup>16</sup>O with an <sup>18</sup>O/<sup>16</sup>O of 0.00206. Ionization efficiency averaged 20 mV/ng of each U isotope. U mass fractionation was corrected using the known <sup>233</sup>U/<sup>235</sup>U ratio of the tracer solution.

U-Pb dates and uncertainties were calculated using the algorithms of Schmitz and Schoene (2007), calibration of ET535 tracer solution (Condon et al., 2015) of <sup>235</sup>U/<sup>205</sup>Pb = 100.233, <sup>233</sup>U/<sup>235</sup>U = 0.99506, and <sup>205</sup>Pb/<sup>204</sup>Pb = 11268, calibration of ET2535 tracer solution (Condon et al., 2015) of <sup>235</sup>U/<sup>205</sup>Pb = 100.233, <sup>233</sup>U/<sup>235</sup>U = 0.99506, <sup>205</sup>Pb/<sup>204</sup>Pb = 8474, and <sup>202</sup>Pb/<sup>205</sup>Pb = 0.99924, U decay constants recommended by Jaffey et al. (1971), and <sup>238</sup>U/<sup>235</sup>U of 137.818 (Hiess et al., 2012). <sup>206</sup>Pb/<sup>238</sup>U ratios and dates were corrected for initial <sup>230</sup>Th disequilibrium using D<sub>Th/U</sub> = 0.20 ± 0.05 (1 $\sigma$ ) and the algorithms of Crowley et al. (2007), resulting in an increase in the <sup>206</sup>Pb/<sup>238</sup>U dates of  $\sim 0.09$  Ma. All common Pb in analyses was attributed to laboratory blank and subtracted based on the measured laboratory Pb isotopic composition and associated uncertainty. U blanks are estimated at 0.013 pg.

Weighted mean <sup>206</sup>Pb/<sup>238</sup>U dates are calculated from equivalent dates (probability of fit  $> 0.05$ ) using Isoplot 3.0 (Ludwig, 2003). Errors on weighted mean dates are given as  $\pm x / y / z$ , where x is the internal error based on analytical uncertainties only, including counting statistics, subtraction of tracer solution, and blank and initial common Pb subtraction, y includes the tracer calibration uncertainty propagated in quadrature, and z includes the <sup>238</sup>U decay constant uncertainty propagated in quadrature. Internal errors should be considered when comparing our dates with <sup>206</sup>Pb/<sup>238</sup>U dates from other laboratories that used the same tracer solution or a tracer solution that was cross-calibrated using EARTHTIME gravimetric standards. Errors including the uncertainty in the tracer calibration should be considered when comparing our dates with those derived from other geochronological methods using the U-Pb decay scheme (e.g., laser ablation ICPMS). Errors including uncertainties in the tracer calibration and <sup>238</sup>U decay constant (Jaffey et al., 1971) should be considered when comparing our dates with those derived from other decay schemes (e.g., <sup>40</sup>Ar/<sup>39</sup>Ar, <sup>187</sup>Re-<sup>187</sup>Os). Errors are at 2 $\sigma$ .

### A.3. Results

Twenty-four grains from S8WY-10 analyzed by LA-ICPMS yield dates of 327 ± 7 to 244 ± 4 Ma. Seven grains analyzed by CA-TIMS yield a weighted mean of 252.67 ± 0.05 / 0.09 / 0.28 Ma (Mean Squared Weighted Deviation (MSWD) = 1.3, probability of fit = 0.24). This is the interpreted depositional age (Figs. A3, A4A-F).

Thirty-one grains from S12-17 analyzed by LA-ICPMS yield dates of 852 ± 23 to 244 ± 12 Ma. Six grains analyzed by CA-TIMS yield a weighted mean of 250.27 ± 0.07 / 0.10 / 0.28 Ma (MSWD = 0.5, probability of fit = 0.75). This is the interpreted depositional age.

Twenty-seven grains from S19-4 analyzed by LA-ICPMS yield dates of 406 ± 10 to 238 ± 6 Ma. Two grains analyzed by CA-TIMS yield a weighted mean of 252.39 ± 0.08 / 0.15 / 0.30 Ma (MSWD = 0.0, probability of fit = 0.96) and one grain yields a date of 252.01 ± 0.11 Ma. This is the interpreted maximum depositional age.

Thirteen grains from S19-7B analyzed by LA-ICPMS yield dates of 373 ± 11 to 247 ± 7 Ma. One grain analyzed by CA-TIMS yields a date of 252.09 ± 0.14. This is the interpreted maximum depositional age.

Thirty-seven grains from S19WY-25 analyzed by LA-ICPMS yield dates of 300 ± 15 to 235 ± 8 Ma. Six grains were analyzed by CA-TIMS, with the five youngest yielding a weighted mean of 253.29 ± 0.04 / 0.13 / 0.30 Ma (MSWD = 0.8, probability of fit = 0.54). This is the interpreted depositional age. The one grain that yielded a date of 255.08 ± 0.08 Ma is interpreted as containing inherited components.

Grains from TRN-8 were not mounted. Nine grains were analyzed by CA-TIMS, with the five youngest yielding a weighted mean of 253.12 ± 0.07 / 0.10 / 0.29 Ma (MSWD = 0.6, probability of fit = 0.70). This is the interpreted depositional age. The two grains that yielded dates of 253.46 ± 0.17 and 253.45 ± 0.27 Ma are interpreted as containing inherited components.

Twenty-six grains from TRN19-WY analyzed by LA-ICPMS yield dates of 263 ± 15 to 238 ± 14 Ma. Eight grains analyzed by CA-TIMS yields date of 254.15 ± 0.12 to 252.65 ± 0.10 Ma. The youngest date is the interpreted maximum depositional age.

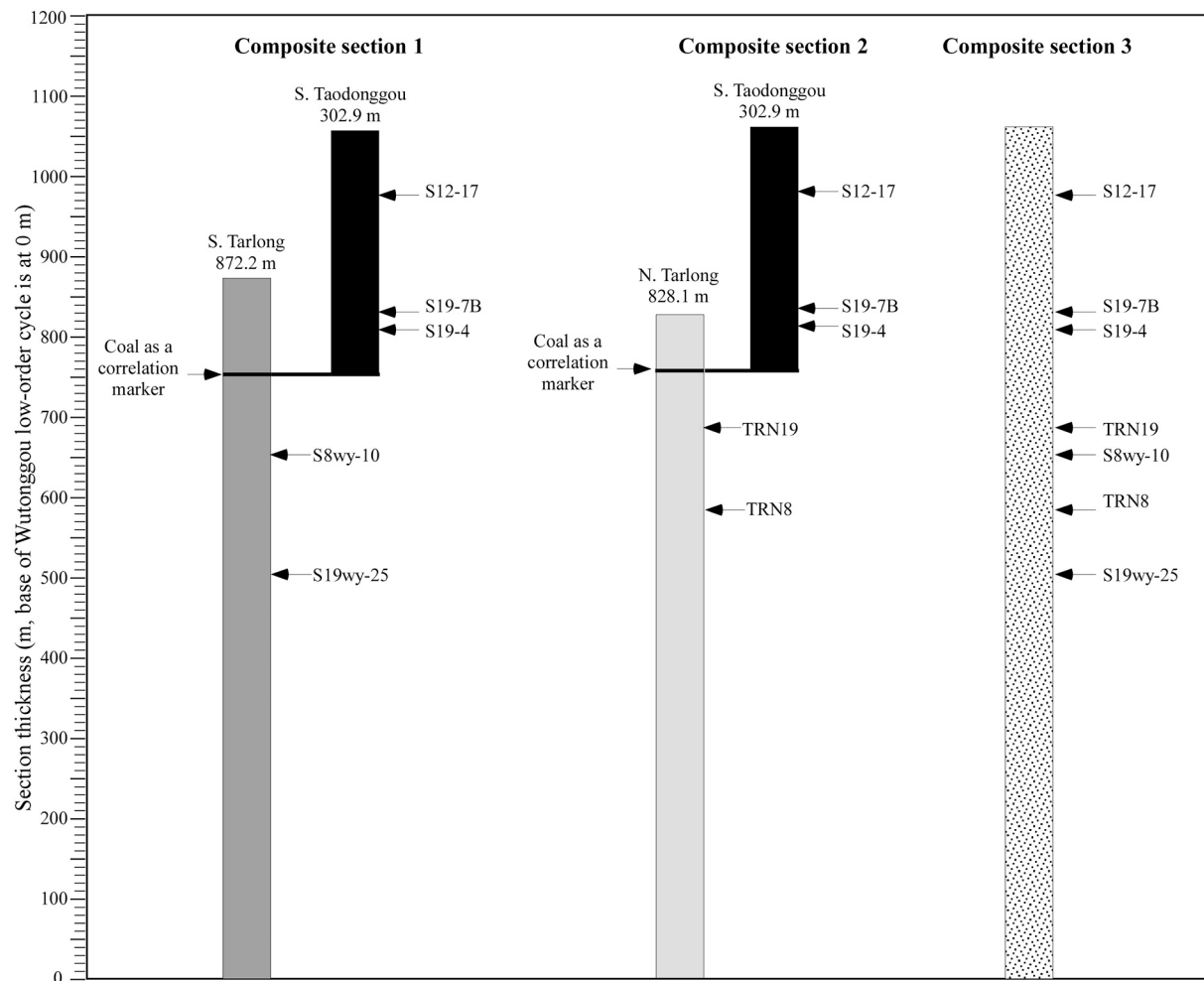


**Fig. A1.** Three composite sections used in the construction of the age model. Composite sections 1, 2, and 3 are constructed using measured sections from south Tarlong-south Taodonggou, north Tarlong-south Taodonggou, and south and north Tarlong and south Taodonggou, respectively. The sections are correlated using the last major coal in the upper part of Wutonggou low-order cycle as the datum. For Composite section 3, the north Tarlong section is normalized against the south Tarlong section between the base of the section and the last coal bed. The normalized section is then correlated with south Taodonggou section using the coal bed as the datum. See Fig. A2 for two alternative age models constructed using age dates from south Tarlong-south Taodonggou and north Tarlong-south Taodonggou sections, respectively.

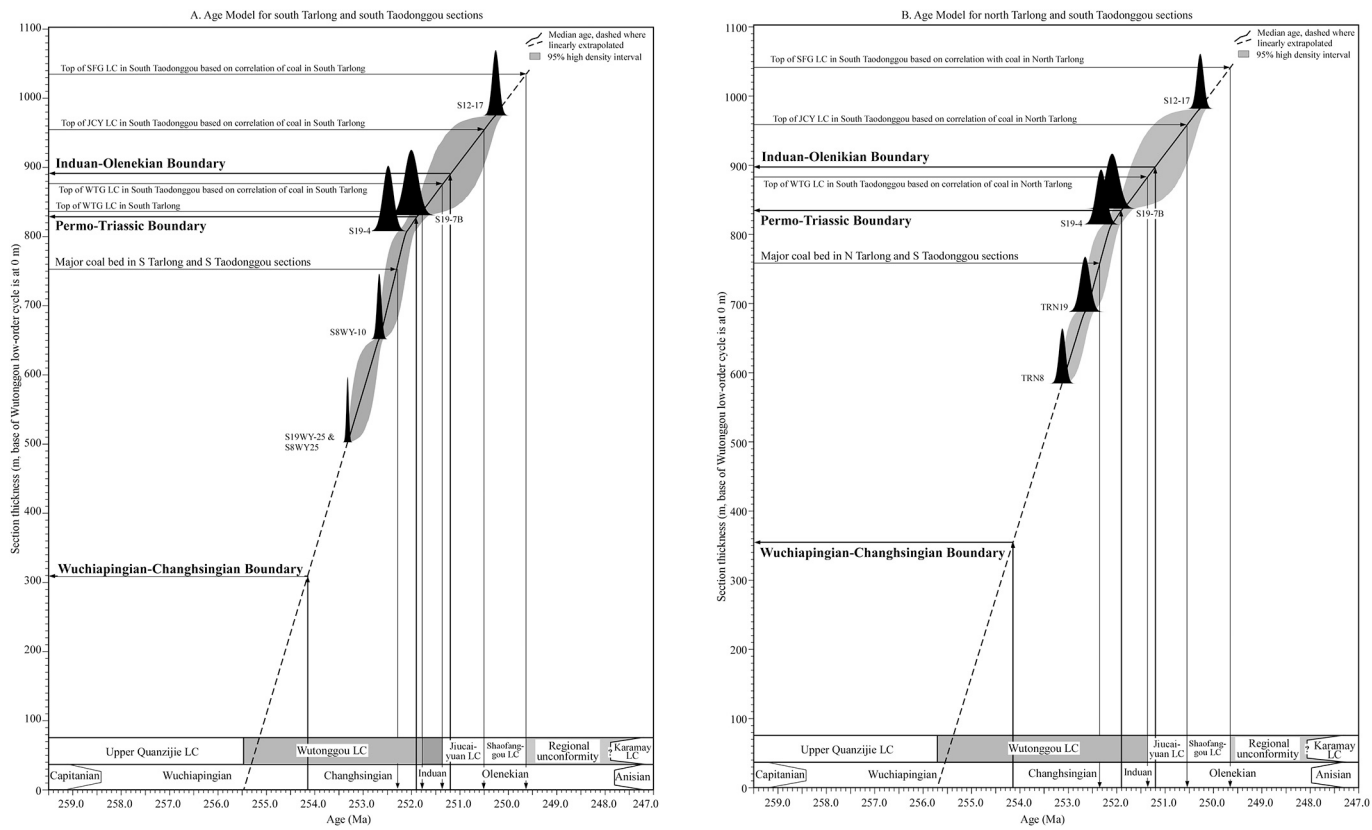


**Fig. A2.** Bayesian age models of upper Permian–Lower Triassic strata constructed using five U-Pb zircon CA-TIMS dates in the south Tarlong and south Taodonggou sections (A) and in the north Tarlong and south Taodonggou sections (B). The sections are correlated using the coal bed in the upper part of Wutonggou low-order cycle. See correlation scheme in Fig. A1. Ages for stage boundaries are from ICS (2020); and the boundaries are projected onto the normalized section to show their respective stratigraphic positions. Boundaries of low-order cycles and the last major coal bed are projected onto the age axis to show their respective ages. The dashed lines beyond the range of the age model are linear extrapolations from adjacent segments of the age models. WTG = Wutonggou, JCY = Jiucaiyuan, SFG = Shaofanggou LCs. See Table 1 for detailed age estimates.

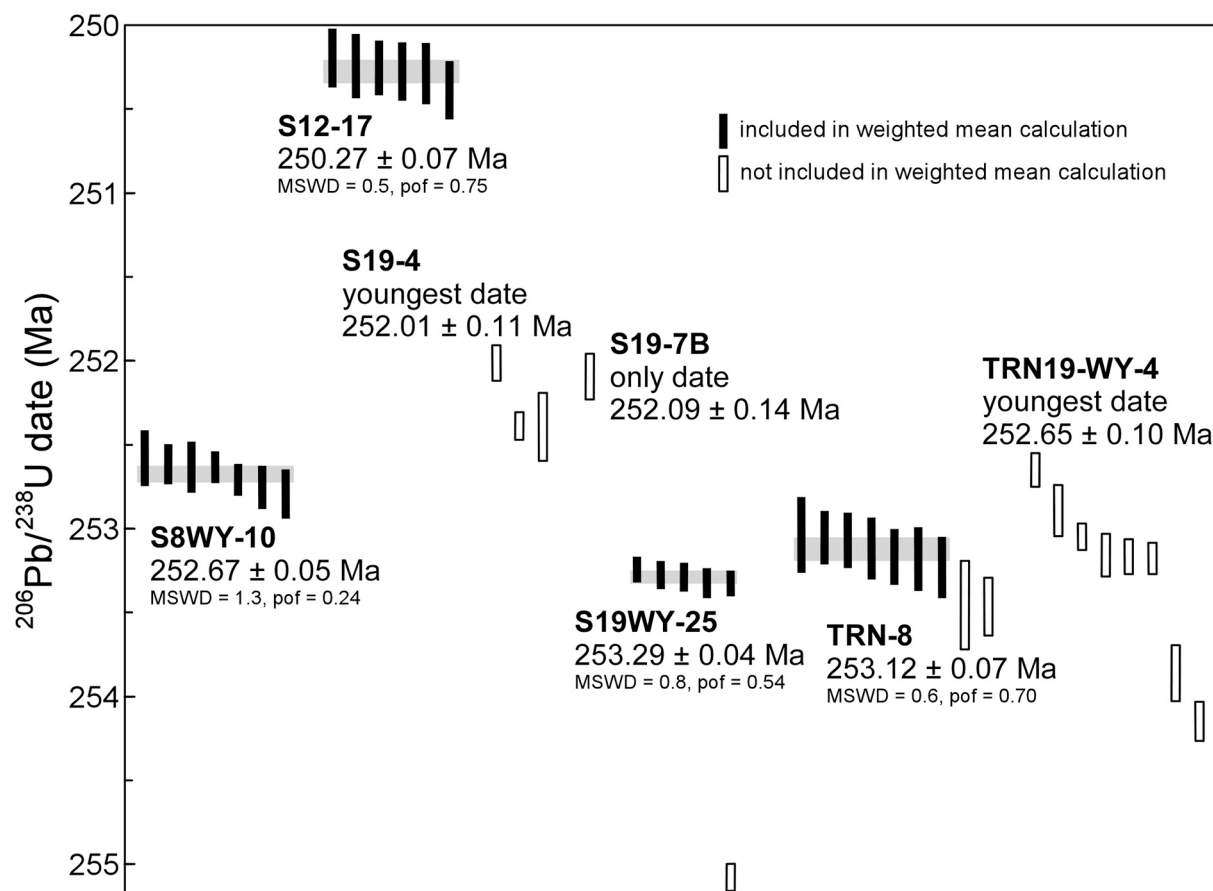


**Fig. A3.** Plot of  $^{206}\text{Pb}/^{238}\text{U}$  dates obtained by CA-TIMS. Plotted with Isoplot 3.0 (Ludwig, 2003). Errors are at  $2\sigma$ . Weighted mean dates are shown and represented by the gray boxes. MSWD = Mean Squared Weighted Deviation, pof = probability of fit.



**Fig. A4.** Cathodoluminescence images of zircon grains collected with a scanning electron microscope for samples S8WY10 (A), S12-17 (B), S19-4 (C), S19-7B (D), S19WY-25 (E), and TRN19-WY (F). Grains dated by CA-TIMS are identified by labels z1, z2, etc.

## References

Afonin, S.A., Foster, C.B., 2005. Palynological assemblages and Permian-Triassic boundary in continental deposits of Dalongkou section (Xinjiang, N.-W., China). In: Afonin, S.A., Tokarev, P.N. (Eds.), XI all-Russian Palynological Conference "Palynology: Theory and Applications, Proceedings of the Conference 27th September–1st October, Moscow". Russian Academy of Science, Palaeontological Institute, pp. 14–18 (in Russian).

Allen, M.B., Windley, B.F., Chi, Z., Jinghui, G., 1993. Evolution of the Turfan Basin, Chinese Central Asia. *Tectonics* 12, 889–896.

Allen, M.B., Şengör, A.M.C., Natal'in, B.A., 1995. Junggar, Turfan and Alakol basins as late Permian to ?Early Triassic extensional structures in a sinistral shear zone in the Altai orogenic collage, Central Asia. *J. of the Geol. Soc. of London* 152, 327–338.

Angielczyk, K.D., Sullivan, C., 2008. *Diictodon feliceps* (Owen, 1876), a dicynodont (Therapsida, Anomodontia) species with a Pangaean distribution. *J. Vertebr. Paleontol.* 28, 788–802.

Angielczyk, K., Liu, J., Yang, W., 2021. A redescription of *Kunpania scopulusa*, a bidentalian dicynodont (Therapsida, Anomodontia) from the Guadalupian of northwestern China. *J. Vertebr. Paleontol.* <https://doi.org/10.1080/02724634.2021.1922428>.

Beerbower, J.R., 1964. Cyclothem and cyclic depositional mechanism in alluvial plain sedimentation. *Bull. Kans. Univ. Geol. Survey* 169, 35–42.

Behrensmeyer, A.K., Kidwell, S.M., Gastaldo, R.A., 2000. Taphonomy and paleobiology. *Paleobiology* 26, 103–147.

Benton, M.J., 2018. Hyperthermal-driven mass extinctions: killing models during the Permian-Triassic mass extinction. *Phil. Trans. R. Soc. A* 376, 20170076. <https://doi.org/10.1098/rsta.2017.0076>.

Benton, M.J., Newell, A.J., 2014. Impacts of global warming on Permo-Triassic terrestrial ecosystems. *Gondwana Res.* 25, 1308–1337.

Botha, J., Smith, R.M.H., 2020. Biostratigraphy of the *Lystrosaurus declivis* Assemblage Zone (Beaufort Group, Karoo Supergroup), South Africa. *South African J. Geology* 123, 207–216. <https://doi.org/10.25131/sajg.123.00152>.

Botha, J., Huttonlocker, A.K., Smith, R.M.H., Prevec, R., Viglietti, P., Modesto, S.P., 2020. New geochemical and palaeontological data from the Permian-Triassic boundary in the South African Karoo Basin test the synchronicity of terrestrial and marine sections. *Palaeogeogr. Palaeoclimatol. Palaeoecol.* 540, 109467.

Bourquin, S., Rossignol, C., Jolivet, M., Poujol, M., Broutin, J., Yu, J., 2018a. Terrestrial Permian-Triassic boundary in southern China: New stratigraphic, structural and palaeoenvironment considerations. *Palaeogeogr. Palaeoclimatol. Palaeoecol.* 490, 640–652. <https://doi.org/10.1016/j.palaeo.2017.11.055>.

Bourquin, S., Rossignol, C., Jolivet, M., Poujol, M., Broutin, J., Yu, J., 2018b. Reply to the comment on "Terrestrial Permian-Triassic boundary in southern China: New stratigraphic, structural and palaeoenvironment considerations" by H. Zhang, Z. Feng, J. Ramezani, S-Z Shen. *Palaeogeogr. Palaeoclimatol. Palaeoecol.* 506, 257–259. <https://doi.org/10.1016/j.palaeo.2018.02.021>.

Brand, U., Yochelson, E.L., Eagar, R.M., 1993. Geochemistry of late Permian non-marine bivalves: Implications for the continental paleohydrology and paleoclimatology of northwestern China. *Carbonates Evaporites* 8, 199–212.

Brown Jr., L.F., Fisher, W.L., 1977. Seismic-stratigraphic interpretation of depositional systems: examples from Brazilian rift and pull-apart basins: in Payton, C.E. (ed.), *Seismic stratigraphy – applications to exploration*. AAPG Mem. 26, 213–248.

Burgess, S.D., Bowring, S., Shen, S.Z., 2014. High-precision timeline for Earth's most severe extinction. *Proc. Natl. Acad. Sci.* 111, 3316–3321. <https://doi.org/10.1073/pnas.1317692111>.

Cao, C.Q., Wang, W., Liu, L.J., 2008. Two episodes of  $^{13}\text{C}$ -depletion in organic carbon in the latest Permian: evidence from the terrestrial sequences in northern Xinjiang, China. *Earth Planet. Sci. Lett.* 270, 251–257.

Carroll, A.R., Bohacs, K.M., 1999. Stratigraphic classification of ancient lakes: Balancing tectonic and climatic controls. *Geology* 27, 99–102.

Carroll, A.R., Graham, S.A., Hendrix, M.S., Ying, D., Zhou, D., 1995. Late Paleozoic tectonic amalgamation of northwestern China: Sedimentary record of the northern Tarim, northwestern Turpan, and southern Junggar Basins. *Geol. Soc. of America Bull.* 107, 571–594.

Carroll, A.R., Graham, S.A., Smith, M.E., 2010. Walled sedimentary basins of China. *Basin Res.* 22, 17–32. <https://doi.org/10.1111/j.1365-2117.2009.00458.x>.

Cascales-Miñana, B., Cleal, C.J., 2014. The plant fossil record reflects just two great extinction events. *Terra Nova* 26, 195–200. <https://doi.org/10.1111/ter.12086>.

Cheng, Z., 1993. On the discovery and significance of the nonmarine Permo-Triassic transition zone at Dalongkou in Jimusar, Xinjiang, China. Pp. 65–67. In: Lucas, S.G., Morales, M. (Eds.), *The Nonmarine Triassic*. New Mexico Museum of Natural History and Science Bulletin, 3.

Cheng, Z.-W., Lucas, S.G., 1993. A possible nonmarine GSSP for the Permian-Triassic boundary. *Albertiana* 12, 39–44.

Cheng, Z.-W., Wu, S.Z., Fang, X.S., 1996. The Permian-Triassic sequences in the southern margin of the Junggar Basin and the Turpan Basin, Xinjiang, China. In: Hongfei, Hou, Jinsong, Zhou (Eds.), *Field Trip Guide; Volume 1, Stratigraphy, Paleontology, Sedimentology, Petroleum and Coal Geology: 30th International Geological Congress. Geological Publishing House, Beijing, China*.

Chu, D.L., Tong, J.N., Song, H.J., Benton, M.J., Song, H.Y., Yu, J.X., Qiu, X.C., Huang, Y.F., Li, T., 2015. Lilliput effect in freshwater ostracods during the Permian-Triassic extinction. *Palaeogeogr. Palaeoclimatol. Palaeoecol.* 435, 38–52. <https://doi.org/10.1016/j.palaeo.2015.06.003>.

Condon, D.J., Schoene, B., McLean, N.M., Bowring, S.A., Parrish, R., 2015. Metrology and traceability of U-Pb isotope dilution geochronology (EARTHTIME Tracer Calibration Part I). *Geochim. Cosmochim. Acta* 164, 464–480.

Crowley, J.L., Schoene, B., Bowring, S.A., 2007. U-Pb dating of zircon in the Bishop Tuff at the millennial scale. *Geology* 1123–1126.

Cui, C., Cao, C., 2021. Increased aridity across the Permian-Triassic transition in the mid-latitude NE Pangea. *Geological Journal* 1–14. <https://doi.org/10.1002/gj.4123>.

Davydov, V.I., 2021. Tunguska coals, Siberian sills and the Permian-Triassic extinction. *Earth Science Review* 212, 103438.

DiMichele, W.A., Gastaldo, R.A., 2008. Plant Paleoecology in Deep Time. *Annals of the Missouri Botanical Gardens* 95, 144–198.

Feng, Z., Wei, H.B., Guo, Y., Bomfleur, B., 2018. A conifer-dominated early Triassic flora from Southwest China. *Sci. Bull.* 63, 1462–1463.

Feng, Z., Wei, H.B., Guo, Y., He, X.Y., Sui, Q., Zhou, Y., Liu, H.Y., Gou, X.D., Lv, Y., 2020. From rainforest to hermland: New insights into land plant responses to the end-Permian mass extinction. *Earth Sci. Rev.* 204, 103153.

Fielding, C.R., Frank, T.D., Vajda, V., McLoughlin, S., Mays, C., Tevayaw, A.P., Winguth, A., Winguth, C., Nicoll, R.S., Bocking, M., Crowley, J.L., 2019. Age and pattern of the southern high-latitude continental end-Permian extinction constrained by multiproxy analysis. *Nat. Commun.* 10, 385. <https://doi.org/10.1038/s41467-018-07934-z>.

Foster, C.B., Afonin, S.A., 2006. *Syndesmorion* gen. Nov.—a coenobial alga of Chlorococcalean affinity from the continental Permian-Triassic deposits of Dalongkou section, Xinjiang Province, China. *Rev. Palaeobot. Palynol.* 6, 1–8.

Fredericks, J.G., 2017. Provenance and Depositional Environments of Fluvial-Lacustrine Deposits in a Non-marine Rift Basin, Lower-Triassic Jiucayuan and Shaofanggou Low-Order Cycles, Bogda Shan, NW China. MS thesis, Missouri University of Science and Technology, Missouri (290 pp).

Gastaldo, R.A., 2019. Ancient plants escaped an ancient mass extinction. *Nature* 567, 38–39.

Gastaldo, R.A., Neveling, J., Clark, C.K., Newbury, S.S., 2009. The terrestrial Permian-Triassic boundary event bed is a non-event. *Geology* 37, 199–202.

Gastaldo, R.A., Tabor, N.J., Neveling, J., 2020a. Trends in stable isotopes and climate proxies from late Changhsingian ghost landscapes of the Karoo Basin, South Africa. *Front. Ecol. Evol.* 8, 567109. <https://doi.org/10.3389/fevo.2020.567109>.

Gastaldo, R.A., Demko, T.M., 2011. Long term hydrology controls the plant fossil record. In: Allison, P.A., Bottjer, D.J. (Eds.), *Taphonomy, Second Edition: Processes and Bias Through Time: Topics in Geobiology*, 32. Springer, pp. 249–286.

Gastaldo, R.A., Kamo, S.L., Neveling, J., Geissman, J.W., Looy, C.V., Martini, A.M., 2020b. The base of the *Lystrosaurus* Assemblage Zone, Karoo Basin, predates the end-Permian marine extinction. *Nat. Commun.* 11, 1428. <https://doi.org/10.1038/s41467-020-15243-7>.

Gastaldo, R.A., Neveling, J., Geissman, J.W., Kamo, S.L., Looy, C.V., 2021. A tale of two Tweefonteins: What physical correlation, geochronology, magnetic polarity stratigraphy, and palynology say about the end-Permian terrestrial extinction paradigm. *Geol. Soc. Am. Bull.* 133 <https://doi.org/10.1130/B35830.1/5345349/b35830.pdf>.

Gerstenberger, H., Haase, G., 1997. A highly effective emitter substance for mass spectrometric Pb isotope ratio determinations. *Chem. Geol.* 136, 309–312.

Glen, J.M.G., Nomade, S., Lyons, J.J., Metcalfe, I., Mundil, R., Renne, P.R., 2009. Magnetostratigraphic correlations of Permian-Triassic marine and terrestrial sediments from western China. *J. Asian Earth Sci.* 36, 521–540.

Greene, T.J., Carroll, A.R., Wartes, M., Graham, S.A., Wooden, J.L., 2005. Integrated provenance analysis of a complex orogenic terrain: Mesozoic uplift of the Bogda Shan and inception of the Turpan-Hami Basin, NW China. *J. of Sedimentary Research* 75, 251–267.

Guan, W., 2011. Provenance Analysis of Upper Permian-Basal Triassic Sedimentary Rocks in the Greater Junggar-Turpan Basin, Southern Bogda Mountains, NW China. MS thesis, Wichita State University, Kansas.

Guan, W., Yang, W., Liu, Y.Q., Feng, Q., 2011. Local and regional sources for Upper Permian-Lowermost Triassic fluvial-lacustrine fills in the Tarlong-Taodonggou half graben, southern Bogda Mountains, NW China. Am. Association of Petroleum Geologists Annual Meeting, Houston, 71.

Hiess, J., Condon, D.J., McLean, N., Noble, S.R., 2012.  $^{238}\text{U}/^{235}\text{U}$  systematics in terrestrial uranium-bearing minerals. *Science* 335, 1610–1614.

Huang, Y., Chen, Z.-Q., Roopnarine, P.D., Benton, M.J., Yang, W., Liu, J., Zhao, L., Li, Z., Guo, Z., 2021. Ecological dynamics of terrestrial and freshwater ecosystems across three mid-Phanerozoic mass extinctions from Northwest China. *Proc. R. Soc. B* 288, 20210148. <https://doi.org/10.1098/rspb.2021.0148>.

International Commission on Stratigraphy, 2020. International Chronostratigraphic Chart, v2020/01. [www.stratigraphy.org](http://www.stratigraphy.org).

Jaffey, A.H., Flynn, K.F., Glendenin, L.E., Bentley, W.C., Essling, A.M., 1971. Precision measurements of half-lives and specific activities of  $^{235}\text{U}$  and  $^{238}\text{U}$ . *Physical Review C* 4, 1889–1906.

Jeffrey, B.M., 2011. Rift Basin-Fill Architecture of Fluvial-Lacustrine Lower Permian Lucaogou and Hongyanchi Low-Order Cycles, Bogda Mountains, NW China. MS thesis, Wichita State University, Kansas (115 pp).

Jeffrey, B., Yang, W., Feng, Q., Liu, Y., 2011. Rift basin-fill architecture of fluvial-lacustrine Lower Permian Lucaogou and Hongyanchi low-order cycles, southern Bogda Mountains, NW China. In: 2011 American Association of Petroleum Geologists Annual Meeting, Houston, 92.

Kammerer, C.F., Angielczyk, K.D., Fröbisch, J., 2011. A comprehensive taxonomic revision of *Dicynodon* (Therapsida, Anomodontia), and its implications for dicynodont phylogeny, biogeography, and biostratigraphy. *Society of Vertebrate Paleontology Memoir* 11, 1–158.

Kozur, H.W., Weems, R.E., 2011. Detailed correlation and age of continental late Changhsingian and earliest Triassic beds: Implications for the role of the Siberian Trap in the Permian. *Palaeogeogr. Palaeoclimatol. Palaeoecol.* 308, 22–40.

Krogh, T.E., 1973. A low contamination method for hydrothermal decomposition of zircon and extraction of U and Pb for isotopic age determination. *Geochim. Cosmochim. Acta* 37, 485–494.

Li, Y.A., Jin, X.C., Sun, D.J., Cheng, Z.W., Pang, Q.Q., Li, P.X., 2003. Paleomagnetic properties of non-marine Permo-Triassic transitional succession of the Dalongkou Section, Jimsar, Xinjiang. *Geol Rev* 49, 525–536 (in Chinese with English abstract).

Li, J., Wu, X., Zhang, F. (Eds.), 2008. The Chinese Fossil Reptiles and their Kin. Science Press, Beijing.

Li, Z.X., Yang, W., Wang, Y.S., Zhang, L.Q., Luo, H.M., Liu, S.H., Zhang, L.K., Luo, X.R., 2019. Anatomy of a lacustrine stratigraphic sequence within the fourth member of the Eocene Shahejie Formation at the steep margin of Dongying Depression, eastern China. *Am. Assoc. Pet. Geol. Bull.* 103, 469–504.

Liao, Z., Lu, L., Jiang, N., Xia, F., Song, F., Zhou, Y., Li, S., Zhang, Z., 1987. Carboniferous and Permian in the western part of the east Tianshan Mountains. In: Eleventh Congress of Carboniferous Stratigraphy and Geology, Guidebook Excursion 4. China, Beijing.

Liu, S., 1994. The non-marine Permian-Triassic boundary and Triassic conchostracean fossils in China. *Albertiana* 13, 12–24.

Liu, Z.S., 2000. The Permo-Triassic boundary at the northern margin of Tu-Ha Basin. *J. Stratigr.* 24, 310–314 (in Chinese with English abstract).

Liu, J., 2021. The tetrapod fauna of the upper Permian Naobaogou Formation of China: 6. *Turfanodon jufengensis* sp. nov. (Dicynodontia). *PeerJ* 9, e10854. <https://doi.org/10.7717/peerj.10854>.

Liu, J., Abdala, F., 2017. Therocephalian (Therapsida) and chroniosuchian (Reptiliomorpha) from the Permo-Triassic transitional Guodikeng Formation of the Dalongkou Section, Jimsar, Xinjiang, China. *Vertebrata PalAsiatica* 55, 24–40.

Liu, J., Li, J.L., Cheng, Z.W., 2002. The *Lystrosaurus* fossils from Xinjiang and their bearing on the terrestrial Permain-Triassic boundary. *Vertebrata PalAsiatica* 40, 267–275 (in Chinese with English abstract).

Looy, C.V., Twitchett, R.J., Dilcher, D.L., Van Konijnenburg-Van Cittert, J.H.A., Visscher, H., 2001. Life in the end-Permian dead zone. *PNAS* 98, 7879–7883. [www.pnas.org/cgi/doi/10.1073/pnas.131218098](http://www.pnas.org/cgi/doi/10.1073/pnas.131218098).

Lu, Y.R., 2016. Origin of Lacustrine Carbonate-Dominated Clinoforms in the Lower-Permian Lucaogou Low-Order Cycle, Southern Bogda Mountains. MS Thesis, Missouri University of Science and Technology, Missouri, NW China.

Lucas, S.G., 2001. Chinese Fossil Vertebrates. Columbia University Press, New York.

Ludwig, K.R., 2003. User's Manual for Isoplot 3.00. Berkeley Geochronology Center, Berkeley, CA (70 pp).

Mack, G.H., James, W.C., 1994. Paleoclimate and the global distribution of paleosols. *J. Geol.* 102, 360–366.

Mack, G.H., James, W.C., Monger, H.C., 1993. Classification of paleosols. *Geol. Soc. of America Bull.* 105, 129–136.

Maisch, M.W., Matzke, A.T., 2014. *Sungeondon kimkraemerae* n. gen. n. sp., the oldest kannemeyeriiform (Therapsida, Dicynodontia) and its implications for the early diversification of large herbivores after the P/T boundary. *N. Jb. Geol. Palaont. Abh.* 272, 1–12.

Mattinson, J.M., 2005. Zircon U-Pb chemical abrasion ("CA-TIMS") method: combined annealing and multi-step partial dissolution analysis for improved precision and accuracy of zircon ages. *Chem. Geol.* 220, 47–66.

Maxwell, W.D., 1992. Permian and early Triassic extinction of non-marine tetrapods. *Palaeontology* 35, 571–584.

Mays, C., Vajda, V., Frank, T.D., Fielding, C.R., Nicoll, R.S., Tevyaw, A.P., McLoughlin, S., 2020. Revised Permian-Triassic floristic timeline reveals early collapse and delayed recovery of south polar terrestrial ecosystems. *Geol. Soc. Am. Bull.* 132, 1489–1513. <https://doi.org/10.1130/B35355.1>.

Metcalfe, I., Foster, C.B., Afonin, S.A., Nicoll, R.S., Mundil, R., Wang, X.F., Lucas, S.G., 2009. Stratigraphy, biostratigraphy and C-isotopes of the Permian-Triassic non-marine sequence at Dalongkou and Lucaogou, Xinjiang Province, China. *J. Asian Earth Sci.* 36, 503–520.

Miall, A.D., 1996. The Geology of Fluvial Deposits: Sedimentary Facies, Basin Analysis, and Petroleum Geology. Springer, New York.

Nowak, H., Schneebeli-Hermann, E., Kustatscher, E., 2019. No mass extinction for land plants at the Permian-Triassic transition. *Nat. Commun.* 10, 384.

Obrist-Farmer, J., Yang, W., 2015. Nonmarine time-stratigraphy in a rift setting: an example from the Mid-Permian lower Quanzijie low-order cycle, Bogda Mountains, NW China. *J. Palaeogeogr.* 4, 27–51.

Obrist-Farmer, J., Yang, W., 2016. Implications of loess and fluvial deposits on paleoclimatic conditions during an icehouse–hothouse transition, Capitanian upper Quanzijie low-order cycle, Bogda Mountains, NW China. *Palaeogeogr. Palaeoclimatol. Palaeoecol.* 441, 959–981. <https://doi.org/10.1016/j.palaeo.2015.10.041>.

Obrist-Farmer, J., Yang, W., 2017. Provenance and depositional conditions of fluvial conglomerates and sandstones and their controlling processes in a rift setting, mid-Permian lower and upper Quanzijie low order cycles, Bogda Mountains, NW China. *J. Asian Earth Sci.* 138, 317–340.

Ogg, J.G., Chen, Z.Q., Orchard, M.J., Jiang, H.S., 2020. The Triassic Period. In: Gradstein, F.M., Ogg, J.G., Schmitz, M.D., Ogg, G.M. (Eds.), *Geologic Time Scale 2020*. Elsevier, pp. 903–953.

Olivier, C., Battail, B., Bourquin, S., Camille Rossignol, C., Steyer, J.-S., Jalil, N.-E., 2019. New dicynodonts (Therapsida, Anomodontia) from near the Permo-Triassic boundary of Laos: implications for dicynodont survivorship across the Permo-Triassic mass extinction and the paleobiogeography of Southeast Asian blocks. *J. Vertebr. Paleontol.* 39, 2. <https://doi.org/10.1080/02724634.2019.1584745>.

Ouyang, S., Norris, G., 1999. Earliest Triassic (Induan) spores and pollen from the Junggar Basin, Xinjiang, northwestern China. *Rev Palaeobot Palyno* 106, 1–56.

Pang, Q., Jin, X.C., 2004. Ostracoda of the Guodikeng Formation and the continental Permo-Triassic boundary of Dalongkou section, Jimsar, Xinjiang. Professional Papers on Stratigraphy and Palaeontology 28, 205–246 (in Chinese).

Peng, X.W., 2016. Provenance and Depositional Environments of Fluvial-Lacustrine Sandstones of Lower Permian Lucaogou Low-Order Cycle, Bogda Mountains, NW China. MS Thesis, Missouri University of Science and Technology, Missouri (163 pp).

Retallack, G.J., 1990. Soils of the Past – An Introduction to Paleopedology. Unwin Hyman, Boston.

Retallack, G.J., 1995. Permian-Triassic life crisis on land. *Science* 267, 77–80.

Retallack, G.J., Veevers, J.J., Morante, R., 1996. Global coal gap between Permian-Triassic extinction and Middle Triassic recovery of peat-forming plants. *Geol. Soc. Am. Bull.* 108, 195–207. [https://doi.org/10.1130/0016-7606\(1996\)108.2.CO;2](https://doi.org/10.1130/0016-7606(1996)108.2.CO;2).

Roopnarine, P.D., Angielczyk, K.D., Wang, S.C., Hertog, R., 2007. Trophic network models explain instability of Early Triassic terrestrial communities. *Proc. R. Soc. B* 274, 2077–2086. <https://doi.org/10.1098/rspb.2007.0515>.

Roopnarine, P.D., Angielczyk, K.D., Oliroyd, S.L., Nesbitt, S.J., Botha-Brink, J., Peecock, B.R., Day, M.O., Smith, R.M.H., 2017. Comparative ecological dynamics of Permian-Triassic communities from the Karoo, Luangwa, and Ruhuhu Basins of southern Africa. *Journal of Vertebrate Paleontology* 37 (sup1), 254–272. <https://doi.org/10.1080/02724634.2018.1424714>.

Sadler, P.M., 1999. The influence of hiatuses on sediment accumulation rates. In: Bruns, P., Hass, H.C. (Eds.), *On the Determination of Sediment Accumulation Rates*, GeoResearch Forum, vol. 5, pp. 15–40.

Schmitz, M.D., Schoene, B., 2007. Derivation of isotope ratios, errors and error correlations for U-Pb geochronology using  $^{205}\text{Pb}$ - $^{235}\text{U}$ - $^{233}\text{U}$ -spiked isotope dilution thermal ionization mass spectrometric data. *Geochemistry, Geophysics, Geosystems (G3)* 8, Q08006. <https://doi.org/10.1029/2006GC001492>.

Schneebeli-Hermann, E., Hochuli, P.A., Bucher, H., 2017. Palynofloral associations before and after the Permian-Triassic mass extinction, Kap Stosch, East Greenland. *Glob. Planet. Chang.* 155, 178–195.

Schneider, J.W., Lucas, S.G., Scholze, F., Voigt, S., Marchetti, L., Klein, H., Oplustil, S., Werneburg, R., Golubev, V.K., Barrick, J.E., Nemirovska, T., Ronchi, A., Day, M.O., Silantiev, V.V., Rößler, R., Saber, H., Linnemann, U., Zharinova, V., Shen, S.Z., 2020. Late Paleozoic-early Mesozoic continental biostratigraphy—Links to the Standard Global Chronostratigraphic Scale. *Palaeoworld* 29, 186–238. <https://doi.org/10.1016/j.palwol.2019.09.001>.

Schumm, S.A., 1968. Speculations concerning paleohydrologic controls of terrestrial sedimentation. *Geol. Soc. of America Bull.* 79, 1573–1588.

Scotese, C.R., Wright, N., 2018. PALEOMAP Paleodigital Elevation Models (PaleoDEM5) for the Phanerozoic. <https://www.earthbyte.org/paleodem-resource-scotese-and-wright-2018/>.

Sengör, A.M.C., Nat'l'in, B.A., 1996. Paleotectonics of Asia: Fragments of a synthesis. In: Yin, A., Harrison, T.M. (Eds.), *The Tectonic Evolution of Asia*. Cambridge University Press, New York, pp. 486–640.

Sengör, A.M.C., Natal'in, B.A., Sunal, G., van der Voo, R., 2018. The Tectonics of the Altai: Crustal Growth during the Construction of the Continental Lithosphere of Central Asia between ~750 and ~130 Ma ago. *Annu. Rev. Earth Planet. Sci.* 46, 439–494.

Shanley, K.W., McCabe, P.J., 1994. Perspectives on the sequence stratigraphy of the continental strata. *Am. Asso. Petrol. Geol. Bull.* 78, 544–568.

Shao, L., Stattegger Garbe-Schoenberg, C.-D., 2001. Sandstone petrology and geochemistry of the Turpan Basin (NW China): Implications for the Tectonic evolution of a continental basin. *J. Sediment. Res.* 71, 37–49.

Shao, L., Stattegger, K., Li, W., Haupt, B.J., 1999. Depositional style and subsidence history of the Turpan Basin (NW China). *Sediment. Geol.* 128, 155–169.

Shen, S.Z., Crowley, J.L., Wang, Y., Bowring, S.A., Erwin, D.H., Sadler, P.M., Cao, C.Q., Rothman, D.H., Henderson, C.M., Ramezani, J., Zhang, H., Shen, Y.N., Wang, X.D., Wang, W., Mu, L., Li, W.Z., Tang, Y.G., Liu, X.L., Liu, L.J., Zeng, Y., Jiang, Y.F., Jin, Y.G., 2011. Calibrating the End-Permian mass extinction. *Science* 334, 1367–1372.

Shen, S.Z., Ramezani, J., Chen, J., Cao, C.Q., Erwin, D.H., Zhang, H., Xiang, L., Schoepfer, S.D., Henderson, C.M., Zheng, Q.F., Bowring, S.A., Wang, Y., Li, X.H., Wang, X.D., Yuan, D.X., Zhang, Y.C., Mu, L., Wang, J., Wu, Y.S., 2019. A sudden end-Permian mass extinction in South China. *Geol. Soc. Am. Bull.* 131, 205–223. <https://doi.org/10.1130/B31909.1>.

Sidor, C.A., O'Keefe, F.R., Damiani, R., Steyer, J.S., Smith, R.M.H., Larsson, H.C.E., Sereno, P.C., Ide, O., Maga, A., 2005. Permian tetrapods from the Sahara show climate-controlled endemism in Pangaea. *Nature* 434, 886–889.

Sidor, C.A., Vilhena, D.A., Angielczyk, K.D., Huttlenlocker, A.K., Nesbitt, S.J., Peecock, B.R., Steyer, J.S., Smith, R.M.H., Tsuji, L.A., 2013. Provincialization of terrestrial faunas following the end-Permian mass extinction. *PNAS* 110, 8129–8133.

Sláma, J., Košler, J., Condon, D.J., Crowley, J.L., Gerdes, A., Hanchar, J.M., Horstwood, M.S.A., Morris, G.A., Nasdala, L., Norberg, N., Schaltegger, U., Schoene, B., Tubrett, M.N., Whitehouse, M.J., 2008. Plešovice zircon — a new natural reference material for U-Pb and Hf isotopic microanalysis. *Chem. Geol.* 249, 1–35.

Smith, R.M.H., Botha-Brink, J., 2014. Anatomy of a mass extinction: Sedimentological and taphonomic evidence for drought-induced die-offs at the Permo-Triassic boundary in the main Karoo Basin, South Africa. *Palaeogeogr. Palaeoclimatol. Palaeoecol.* 396, 99–118.

Smith, R.M.H., Ward, P.D., 2001. Pattern of vertebrate extinctions across an event bed at the Permo-Triassic boundary in the Karoo Basin of South Africa. *Geology* 29, 1147–1150. [https://doi.org/10.1130/0091-7613\(2001\)029<1147:POVEAA>2.0.CO;2](https://doi.org/10.1130/0091-7613(2001)029<1147:POVEAA>2.0.CO;2).

Stanley, S.M., 2016. Estimates of the magnitudes of major marine mass extinctions in earth history. *Proc. Natl. Acad. Sci. U. S. A.* 113, E6326–E6334.

Talbot, M.R., Allen, P.A., 1996. Lakes. In: Reading, H.G. (Ed.), *Sedimentary Environments: Processes, Facies and Stratigraphy*. Blackwell Science, London, pp. 83–124.

Thomas, S.G., Tabor, N.J., Yang, W., Myers, T.S., Yang, Y., Wang, D., 2011. Paleosol stratigraphy across the Permo-Triassic boundary, Bogda Mountains, NW China: Implications for palaeoenvironmental transition through earth's largest mass extinction. In: Algeo, T.J., Chen, Z.-Q., Fraiser, M.L., Twitchett, R.J., eds., *Special Issue: Permian-Triassic ecosystems: collapse and rebuilding*. Palaeogeogr. Palaeoclimatol. Palaeoecol. 308, 41–64. <https://doi.org/10.1016/j.palaeo.2010.09.020>.

Trayler, R.B., Schmitz, M.D., Cuitiño, J.I., Kohn, M.J., Bargo, M.S., Kay, R.F., Strömborg, C.A.E., Vizcaíno, S.F., 2020. An improved approach to age-modeling in deep time: Implications for the Santa Cruz Formation, Argentina. *Geol. Soc. Am. Bull.* 132, 233–244. <https://doi.org/10.1130/B35203.1>.

Viglietti, P.A., 2020. Biostratigraphy of the *Dipteridophyllum* Assemblage Zone (Beaufort Group, Karoo Supergroup), South Africa. *South African Journal of Geology* 123, 191–206. <https://doi.org/10.25131/sajg.123.0014>.

Viglietti, P.A., Benson, R.B.J., Smith, R.M.H., Botha, J., Kammerer, C.F., Skosan, Z., Butler, E., Crean, A., Ellof, B., Kaal, S., Mohoi, J., Molehi, W., Matalana, N., Mtungata, S., Ntheri, N., Ntsala, T., Nyaphuli, J., October, P., Skinner, G., Strong, M., Stummer, H., Wolvaaert, F.P., Angielczyk, K.D., 2021. Evidence from South Africa for a protracted end-Permian extinction on land. *Proc. Natl. Acad. Sci.* 118, e2017045118.

Wagner, P.J., Kosnik, M.A., Lidgard, S., 2006. Abundance distributions imply elevated complexity of post-Paleozoic marine ecosystems. *Science* 314, 1289–1292.

Wan, M.L., Yang, W., Wang, J., 2014. *Septomedullopitys szei* sp. nov., a new Gymnospermous wood from lower Wuchiapingian (upper Permian) continental deposits of NW China, and its implication for a weakly seasonal humid climate in mid-latitude NE Pangaea. *Palaeogeogr. Palaeoclimatol. Palaeoecol.* 407, 1–13. <https://doi.org/10.1016/j.palaeo.2014.04.011>.

Wan, M.L., Yang, W., Liu, L.J., Wang, J., 2016a. Plant-arthropod and plant-fungus interactions in late Permian gymnospermous woods from the Bogda Mountains, Xinjiang, northwestern China. *Rev. Palaeobot. Palynol.* 235, 120–128.

Wan, M.L., Yang, W., Wan, S., Wang, J., 2021a. Wildfires in the Early Triassic of northeastern Pangaea: Evidence from fossil charcoal in the Bogda Mountains, northwestern China. *Palaeoworld*. <https://doi.org/10.1016/j.palwor.2021.07.002>.

Wan, M.L., Yang, W., Wang, K.Y., Liu, L.J., Wang, J., 2021b. *Zhuottingoxylon liaoii* gen. Et sp. nov., a silicified coniferous trunk from the Changhsingian (Permian) of southern Bogda Mountains, northwestern China. *Geol. J.* <https://doi.org/10.1002/gj.4189>.

Wan, M.L., Zhou, W.M., Yang, W., Wang, J., 2016b. Charred wood of *Prototaxoxylon* from the Wuchiapingian Wutonggou Formation (Permian) of Dalongkou, northern Bogda Mountains, northwestern China. *Palaeoworld* 25, 21–31.

Wan, M.L., Yang, W., Liu, L.J., Wang, J., 2017a. *Ductoagathoxylon jimsarensis* sp. nov., a coniferous wood from the Wuchiapingian (upper Permian) Wutonggou Formation in Junggar Basin, northern Bogda Mountains, northwestern China. *Rev. Palaeobot. Palynol.* 241, 13–25. <https://doi.org/10.1016/j.revpalbo.2017.02.004>.

Wan, M.L., Yang, W., Tang, P., Liu, L.J., Wang, J., 2017b. *Medullopaxoxylon triassicum* gen. et sp. nov., a taxodiaceous conifer wood from the Norian (Triassic) of northern Bogda Mountains, northwestern China. *Rev. Palaeobot. Palynol.* 241, 70–84. <https://doi.org/10.1016/j.revpalbo.2017.02.009>.

Wan, M.L., Yang, W., Wang, J., 2019a. *Amyelon bogdense* sp. nov., a silicified gymnospermous root from the Changhsingian–Induan (?) in southern Bogda Mountains, northwestern China. *Rev. Palaeobot. Palynol.* 263, 12–27. <https://doi.org/10.1016/j.revpalbo.2019.01.004>.

Wan, M.L., Yang, W., Wang, J., 2019b. *Sclerospiroxylon xinjiangensis* sp. nov., a gymnospermous wood from the Kunjurang (lower Permian) southern Bogda Mountains, northwestern China: systematics and palaeoecology. *Geobios* 52, 85–97. <https://doi.org/10.1016/j.geobios.2018.11.005>.

Wan, M.L., Yang, W., Wang, J., 2019c. A new *Protophyllocladoxylon* wood from the Induan (lower Triassic) Jiucayuan Formation in the Turpan–Hami Basin, southern Bogda Mountains, northwestern China. *Rev. Palaeobot. Palynol.* 267, 62–72. <https://doi.org/10.1016/j.revpalbo.2019.05.005>.

Wan, M.L., Gastaldo, R., Yang, W., 2019d. Taphonomic and paleoecological aspects of a silicified stand of the gymnosperm *Protophyllocladoxylon* from the Wutonggou low order cycle, Bogda Mountains, Xinjiang Province, western China. *Geological Society of America Abstracts with Programs* 51. <https://doi.org/10.1130/abs/2019AM-335626>.

Wan, M.L., Yang, W., Wang, J., 2020. *Palaeocupressinoxylon uniserialis* n. gen. n. sp., a gymnospermous wood from the upper Permian of Central Taodonggou, southern Bogda Mountains, northwestern China. *Palaeoworld* 29, 117–125. <https://doi.org/10.1016/j.palwor.2019.06.002>.

Ward, P.D., Botha, J., Buick, R., Dekock, M.O., Erwin, D.H., Garrison, G., Kirschvink, J., Smith, R.H.M., 2005. Abrupt and gradual extinction among late Permian land vertebrates in the Karoo Basin, South Africa. *Science* 307, 709–714. <https://doi.org/10.1126/science.1110768>.

Wartes, M.A., Carroll, A.R., Greene, T.J., 2002. Permian sedimentary record of the Turpan–Hami Basin and adjacent regions, Northwest China; constraints on postamalgamation tectonic evolution. *Geol. Soc. of America Bull.* 114, 131–152.

Watson, E.B., Wark, D.A., Thomas, J.B., 2006. Crystallization thermometers for zircon and rutile. *Contrib. Mineral. Petrol.* 151, 413–433.

Xinjiang Uyghur Autonomous Region Bureau of Geology and Mineral Resources, 1993. *Regional Geology of Xinjiang Uyghur Autonomous Region*. Geological Publishing House, Beijing (762 pp in Chinese).

Xinjiang Uyghur Autonomous Region Bureau of Geology and Mineral Resources, 1999. *Stratigraphy of Xinjiang Uyghur Autonomous Region*. Publication House of China University of Geosciences, Wuhan, China, 430 pp. (in Chinese).

Yang, J.D., Qu, L.F., Zhou, H.Q., 1986. Permian and Triassic strata and fossil assemblages in the Dalongkou area of Jimsar. Xinjiang. Beijing. Geological Publishing House 1–262 (in Chinese with English abstract).

Yang, W., 1996. Cycle symmetry and its causes. *Cisco Group (Virgilian and Wolfcampian)*, Texas. *J. Sediment. Res.* B66, 1102–1121.

Yang, W., 2008. Internal Report – Depositional Systems Analysis within a Seismic Sequence Stratigraphic Framework, Turpan–Hami Basin, NW China. *Tu-Ha Oil Company*, PetroChina.

Yang, W., Komlin, M., Major, R., 1998. Distinguishing the roles of autogenic versus allogenic processes in cyclic sedimentation. *Cisco Group (Virgilian and Wolfcampian)*, North-Central Texas. *Geol. Soc. Am. Bull.* 110, 1333–1353.

Yang, W., Mazzullo, S.J., Teal, C.S., 2004. Sediments, facies tracts, and variations in sedimentation rates of Holocene platform carbonate sediments and associated deposits, northern Belize – Implications for “representative” sedimentation rates. *J. Sediment. Res.* 74, 498–512.

Yang, W., Liu, Y., Feng, Q., Lin, J., Zhou, D., Wang, D., 2007a. Sedimentary evidence of early-late Permian mid-latitude continental climate variability, southern Bogda Mountains, NW China. *Palaeogeogr. Palaeoclimatol. Palaeoecol.* 252, 239–258.

Yang, W., Feng, Q., Liu, Y.Q., Tabor, N., Thomas, S., Yang, Y., Sun, G.Z., Sun, B., 2007b. Promises and problems of two-dimensional nonmarine sequence stratigraphic analysis using hierarchical depositional cycles – an example from outcrop Lower Permian to Lower Triassic fluvial-lacustrine deposits, Southern Bogda Mountains, Turpan Intermontane Basin, NW China. In: *Am. Assoc. Petrol. Geologists Annual Meeting, Abstracts Volume*, p. 154.

Yang, W., Feng, Q., Guan, W., Lin, J., Liu, Y.Q., 2009. Wither Nonmarine Sequence Stratigraphy? Sequence Stratigraphic Correlation of Lower Permian Fluvial-Lacustrine Deposits in a Half Graben, Bogda Mountains, NW China. *Am. Assoc. Petrol. Geologists Annual Meeting, Abstracts Volume*, p. 226.

Yang, W., Feng, Q., Liu, Y.Q., Tabor, N., Miggins, D., Crowley, J.L., Lin, J., Thomas, S., 2010. Depositional environments and cyclo- and chronostratigraphy of uppermost Carboniferous-lower Triassic fluvial-lacustrine deposits, southern Bogda Mountains, NW China – terrestrial palaeoclimatic record of mid-latitude NE Pangaea. *Glob. Planet. Chang.* 73, 15–113.

Yang, W., Crowley, J.L., Oberst, J., Tabor, N.J., Feng, Q., Liu, Y.Q., 2013. A marine back-arc origin for the Upper Carboniferous basement of intracontinental greater Turpan–Junggar basin – Volcanic, sedimentary, and geochronologic evidence from southern Bogda Mountains, NW China. *Geological Society of America Abstracts with Programs* 45 (7), 294.

Yang, W., Li, Z.X., Yu, Q.W., 2015. Thick coarse-grained transgressive siliciclastic deposits in lacustrine sequences. In: *Geological Society of America Abstracts with Programs* 47, Paper No. 284–11.

Yang, W., Wan, M.L., Zhan, X., 2018. Cyclostratigraphic correlation of uppermost Permian-Lower Triassic fluvial-lacustrine records in Bogda Mountains, greater Turpan–Junggar basin, NW China – Updates from sedimentary, geochemical, and paleobotanical data. *Geological Society of America Abstracts with Programs* 50. <https://doi.org/10.1130/abs/2018AM-321878>.

Yuan, P.L., Young, C.C., 1934. On the discovery of a new *Dicynodon* in Sinkiang. *Bulletin of the Geological Society of China* 13, 563–573.

Zhan, X., 2019. Paleoenvironment and Paleoclimate of NE Pangaea in Early Permian – Linking Chemo- and Cyclo-Stratigraphy, Bogda Mountains, NW China. *Ph.D. dissertation*, Missouri University of Science and Technology (138 pp).

Zhang, X., 1981. *Regional Stratigraphic Chart of Northwestern China*, Branch of Xinjiang Uyghur Autonomous Region. Geological Publishing House, Beijing (496 pp in Chinese).

Zhang, H., Cao, C.-Q., Liu, X.-L., Mu, L., Zheng, Q.-F., Liu, F., Xiang, L., Liu, L.-J., Shen, S.-Z., 2016. The terrestrial end-Permian mass extinction in South China. *Palaeogeogr. Palaeoclimatol. Palaeoecol.* 448, 108–124. <https://doi.org/10.1016/j.palaeo.2015.07.002>.

Zheng, D.Y., Yang, W., 2020. Provenance of upper Permian-lowermost Triassic sandstones, Wutonggou low-order cycle, Bogda Mountains, NW China: implications on the unroofing history of the Eastern North Tianshan Suture. *Journal of Palaeogeography* 9, 19. <https://doi.org/10.1186/s42501-020-00067-9>.

Zhou, T.S., Zhou, H.Q., 1986. *Palaeobotany*. In: Institute of Geology, Chinese Academy of Geological Sciences, Institute of Geology, Xinjiang Bureau of Geology and Mineral Resources (Eds.), *People's Republic of China Ministry of Geology and Mineral Resources, Geological Memoirs Series 2, Number 3, Permian and Triassic Strata and Fossil Assemblages in the Dalongkou Area of Jimsar, Xinjiang*. Geological Publishing House, Beijing, pp. 39–69 (in Chinese with English summary).

Zhou, T., Li, X., Yang, J., Hou, J., Liu, S., Cheng, Z., Wu, S., Li, Y., 1997. Research on Chinese nonmarine Permo-Triassic GSSP sections. *Xinjiang Geol.* 15, 211–225 (in Chinese with English abstract).

Zhu, H.-C., Ouyang, S., Zhan, J.-Z., Wang, Z., 2005. Comparison of Permian palynological assemblages from the Junggar and Tarim basins and their phytoprovincial significance. *Rev. Palaeobot. Palynol.* 136, 181–207.